Interpretation of regional geophysics of the Pilbara Craton, northwest Australia

PETER WELLMAN

RECORD 1999/4

AGSO

AUSTRALIAN GEOLOGICAL SURVEY ORGANISATION

AUSTRALIAN GEOLOGICAL SURVEY ORGANISATION
DEPARTMENT OF INDUSTRY, SCIENCE & RESOURCES

AGSO RECORD 1999/4

Interpretation of regional geophysics of the Pilbara Craton, northwest Australia

PETER WELLMAN

Minerals Division, Australian Geological Survey Organisation, GPO Box 378, Canberra, ACT 2601

CANBERRA 1999

Department of Industry, Science & Resources

Minister for Industry, Science & Resources: Senator the Hon. Nick Minchin
Parliamentary Secretary: The Hon. Warren Entsch, MP
Secretary: Russell Higgins

Australian Geological Survey Organisation

Executive Director: Neil Williams

ISSN 1039–0073
ISBN 0 642 27380 4

Bibliographic reference: Peter Wellman., 1999. Interpretation of regional geophysics of the Pilbara Craton, northwest Australia. Australian Geological Survey Organisation, Record 1999/4.

Contents

Abstract 1
Introduction 2
Thickness of granites from gravity anomalies 2
  Gravity datasets 2
  Calculation of the gravity anomaly due to density variation in the upper crust 2
  Geological model for the granites 3
  Margins of the granites 3
  Depth to the base of the granites 4
  Conclusions 4
Quantitative analysis of gamma-ray spectrometric surveys for solid-rock geological mapping 4
  Spectrometric surveys over the north Pilbara region 4
  Description of methods of analysis 5
  Analysis of the Pilbara exposures in terms of component analysis 6
    Separation of pixels into the major rock types 6
    Illustration of component analysis for three major rock groups 6
  Evolution paths for felsic igneous rocks 7
  Geochemical maps 7
  Conclusions 8
Major crustal fractures within the Pilbara Craton 8
  Northeast to east trending shear zones 8
  NNW trending faults 9
Interpretation of the magnetic anomalies in terms of geological features 9
Direction of magnetisation of dykes 10
Total vertical deformation after 2780 Ma: Map of depth to the base of the Fortescue Group 10
Susceptibility measurements 10
Long-wavelength magnetic anomalies 11
Regional variation of crustal properties across the Pilbara Craton 13
Conclusions 13
Acknowledgments 14
References 15

Appendix 1. Equations in K, Th and U defining for major rock types their fields in K-Th-U space 15
Appendix 2. Distribution of susceptibilities for major rock types 16
Figure 1. Location map. 18
Figure 2. Comparison of residual gravity anomalies 19
Figure 3. Calculation of Faye gravity anomalies. 20
Figure 4. Seismic refraction velocity/depth models of the Pilbara Craton. 21
Figure 5. Inter-relationship of seismic, gravity and magnetic interpretations. 22
Figure 6. Location of the maximum gravity gradient. 23
Figure 7. Relation between the granite margin's outcrop/subcrop and the margins average position at depth. 24
Figure 8. Thickness of granites. 25
Figure 9. Comparison of display methods of spectrometric data. 26
Figure 10a, b. Scattergram for felsic igneous rocks. 27
Figure 10c, d. Scattergram for intermediate igneous rocks of the Fortescue Group. 28
Figure 10e, f. Scattergram for two areas of Pilbara sedimentary rocks. 29
Figure 10g, h. Scattergram for two areas of the mafic volcanics. 30
Figure 10i, j. Scattergram for two more areas of the mafic volcanics. 31
Figure 11. Scattergrams showing the significant correlation between K and Th for major rock types. 32
Figure 12. Mafic igneous rocks - comparison of RGB composite image, with pseudocolour images. 33
Figure 13. Intermediate igneous rocks - comparison of RGB composite image, with pseudocolour images. 34
Figure 14. Sedimentary rocks - comparison of RGB composite image, with pseudocolour images. 35
Figure 15. Amount of differentiation of granites. 36
Figure 16. Scattergram of composite data from granitoid complexes. 37
Figure 17. Scattergram of K vs Th for the Shaw Granitoid Complex granites with K > 2.8%. 37
Figure 18a, b. Scattergrams for Yule and Shaw Granitoid Complexes. 38
Figure 18c, d. Scattergrams for Corunna Downs and Edgar Granitoid Complexes. 39
Figure 19. Major crustal fractures and boundaries in the Pilbara Craton. 40
Figure 20. Magnetic polarity of dykes mapped from magnetic images. 41
Figure 21. Contours of the elevation of the base of the Hamersley Basin rocks. 42
Figure 22. Plots of susceptibility against distance for 10 susceptibility traverses. 43
Figure 23. Histograms of susceptibility of major rock types, Peter Wellman data. 44
Figure 24. Histograms of susceptibility of major rock types, observations taken during geological mapping. 45
Figure 25. Histograms of susceptibility of major rock types, a summary of all data. 46
Figure 26. Total magnetic intensity reduced-to-the-pole for the western part of the Pilbara Craton. 47
Figure 27. Total magnetic intensity reduced-to-the-pole for the eastern part of the Pilbara Craton. 48
Figure 28. Interpretation of long-wavelength magnetic anomalies. 49

Figure 29. Model anomalies for interpreting the long-wavelength magnetic anomalies of the Pilbara Craton. 50
Figure 30. Map of the larger magnetic anomalies reduced to the pole assuming a magnetic inclination of -80°. 51
Figure 31. Modelling of magnetic anomaly profiles. 52
Figure 32. Regional magnetic and gravity anomalies over the Pilbara Craton. 53
Figure 33. Synthetic example to show the problem with detailed modelling of gravity over granites. 54
Figure 34. Coordinate systems: a, principal components; b, c, components. 54
Figure 35. Legend for geochemical map of Fig. 9g. 55
Figure 36. Modelling of the gravity anomaly between granitoid complex and greenstone belt 55

Abstract

This study reports on the general interpretation of gravity, magnetic and spectrometric data for the Archaean-age Pilbara Craton. The main focus of the work is to obtain some understanding of the 3D shape of the main geological elements within the upper crust. The gravity data are consistent with the granitoid complexes having generally vertical margins at depth. The preferred model for the seismic refraction, magnetic and gravity data is for the seismic velocity gradient at 14 km between the upper and lower crust to correspond with both the base of the granitoid complexes, and the base of the greenstone belts including banded iron formations. The lower crustal material must be more mafic than the average for the upper crust.

The northeast third of the craton is interpreted to have relatively high mean density and lower susceptibility in the upper crust on the basis of the regional gravity and magnetic data. Major shear fractures crossing the Pilbara Craton trend generally east and northeast, and are within the northwest half of the craton.

In areas of exposed rock the the major rock types can be separated using the spectometric data. For each of these rock types the data can be usefully expressed as three uncorrelated components. For felsic igneous rocks, the spectrometric data can be used to subdivide the rocks into four groups with different K, Th and U compositional ranges, and different directions of geochemical variation.

Introduction

The Pilbara Craton is an area of Archaean rocks in the northern part of Western Australia (Fig. 1) about 650 x 500 km in extent. The craton consists of two elements. The basement is ca. 3500-2800 Ma granite-greenstone terrain (Hickman 1983)(Fig. 1). These rocks are some of the oldest areas of well exposed Archaean on the Earth, and they have low deformation and low metamorphism. This basement is overlain unconformably by ca. 2800-2400 Ma sediments and intermediate lavas of the Hamersley Basin. These comprises a lower sequence (the Fortescue Group) of mainly lavas, and an upper sequence (the Hamersley Group) of mainly sediments. The northern half of the Pilbara Craton on land consists of well exposed granite-greenstone basement with small outliers of Hamersley Basin Rocks. The souther half of the Pilbara Craton consists of Hamersley Basin rocks with small inliers of granite-greenstone basement.

In order to enhance the geological understanding of the north Pilbara area, AGSO and GSWA are cooperating in the North Pilbara Project (1995-2000) (http://www.agso.gov.au/minerals/pilbara/) within the National Geoscience Mapping Accord. As part of this accord most of the area of granite-greenstone rocks of the north Pilbara area were covered by airborne surveys during 1995-1996. Each airborne survey measured total magnetic intensity, gamma-ray spectrometry, and surface altitude, with a flight line spacing of 400 m. In this record I discuss the interpretation of these magnetic and spectrometric data, together with existing seismic refraction and gravity data, and field susceptibilities collected during 1996-1997. The objective of the study is to obtain an understanding of the upper crust of the North Pilbara Project area as a whole, rather than an understanding of details at 1:100 000 or 1:250 000 scale.

In the following discussion I use some words in a restricted sense. North Pilbara region is used for the area of exposed granite/greenstone rock within the northern part of the Pilbara Craton. Granite is used for felsic plutonic rock. Greenstone belt is used for the non-granite rocks of the north Pilbara region, mainly lava and sediments.

Thickness of granites from gravity anomalies

Gravity anomalies provide an important source of information about the distribution of rock types in the middle part of the upper crust. The information from gravity anomalies on rock types at depths below 2 km in the upper crust is more reliable that that derived from interpretation of magnetic anomalies for two reasons: 1) the major rock types have more distinct differences in density than magnetic properties, so rock type identification is more reliable, and 2) the gravity anomaly for a body drops off with the square of the distance, and that for magnetics drops off at the cube of the distance, so the gravity anomalies contain more information on rock types at depth.

Gravity datasets

Gravity surveys of the Pilbara Craton have been compiled and integrated by the Gravity Section of AGSO. The gravity field is essentially defined by the following three surveys: AGSO survey 6824 which covered the marine area by a series of east-west ship-borne traverses at about 16 km spacing, AGSO survey 6914 which covered the land area on a grid at 11 km spacing, and survey 9063 of the southern part of the area by CRA (Hamersley Iron) on a 5 km grid. Using these surveys the southern part of the land area has a well defined gravity field, the northern part of the land area is adequately defined, the near-shore 30 km of the marine area is undefined by surveys, and the remainder of the marine area is relatively poorly defined because of poor ship-navigation.

Calculation of the gravity anomaly due to density variation in the upper crust

In modelling the gravity anomaly due to density variation in the upper crust, there are two major decisions to be made: crustal strength, and the reference rock-type for the upper crust.

The gravity anomaly due to density variation in the upper crust is calculated by subtracting from the Bouguer anomaly the anomaly due to density variation below the upper crust. These density variations below the upper crust are more distant from the Earth's surface, so they have a relatively longer wavelength.

The normal procedure is to remove a long-wavelength regional from the Bouguer anomaly such that one is left with an apparently sensible gravity anomaly due to the upper crust. A regional surface can be fitted to the value of the lowest anomalies of the larger granites - this surface has a shortest wavelength of 100 km. When this is removed from the Bouguer anomaly, the resultant residual anomaly is that of Figure 2a. However, the Pilbara Craton has high crustal strength (Zuber et al., 1989), so the regional anomaly should be of wavelength 200-300 km. Hence the resultant residual anomaly is incorrect, because it has removed wavelengths that are too short.

In this study, I have taken the conservative view. We know that the crust will support isostatic anomalies, so these anomalies are an estimate of the anomalies due to the upper crust.

The procedure used can be visualised by reference to Figures 2 and 3. The Bouguer anomaly (Fig. 3a) shows local gravity lows over the granites, and a steep regional anomaly that is lowest in the southern central part of the area. The regional topography (Fig. 3b) is highest in this southern central area; in part the slope on the regional Bouguer anomaly is due to isostatic compensation of this topography, known to be mainly at the base of the crust. The topographic effect has been removed by subtracting the 50 km x 50 km average Bouguer correction from the Bouguer anomaly, to give the Faye gravity anomaly (Fig. 3c). This is essentially a terrain-corrected free air anomaly, equivalent to an isostatic anomaly for a zero crustal thickness. Because it is a type of isostatic anomaly, no short wavelength anomalies have been removed that are due to density variation in the upper crust.

In modelling the upper crust one must have a reference major rock type, forming large volumes in the upper crust, with which the density of other rocks is compared. The possible choices in the north Pilbara region are granite, pre-

Hamersley sediment, and mafic lava. The reference rock chosen here is granite, because of its wide distribution, and the likelihood that most granitoid complexes have a similar average density.

The ideal is to have the same residual gravity anomaly over the middle of each major granite, so that the gravity residuals give the gravity attraction of masses differing from a granite upper-crustal model. Figure 2b shows the Faye anomalies, overlain with the outline of the granites derived from geological mapping and short-wavelength magnetic anomalies. The Faye anomalies over the granites of the central-southern area are more negative than elsewhere. A second-order surface has been removed from the Faye anomaly, such that the resulting residual anomaly (Fig. 2c) is similar over the middle of most of the larger granitoid complexes. Using a second-order surface it is impossible to get a perfect fit for all granites. More positive anomaly values are obtained over the smaller granites with irregular outlines, and this is thought to be due to these granites being thinner. More negative anomaly values are obtained over two types of granites. The first type comprises three granites near the middle of the study area (A-C of Fig. 2c; parts of the Carlindi and Yule Granitoid Complexes), where the negative anomalies are attributed to the granite being more felsic, and hence of a lower mean density than normal, the mean density being judged on the basis of geological mapping, gamma-ray spectrometric data, and magnetic anomalies. The second type comprises granites along the margin of the craton, where the negative anomaly is due in part to the effects of the craton margin (Wellman 1978)(D to E, and F to G in Fig. 2c).

Geological model for the granites

The main features of the Pilbara crust are shown by seismic refraction studies. Models of Drummond (1983) show a two-layer crust (Fig. 4), with a steep velocity increase between the upper and lower crust. The crust thickens slightly to the south. The simplest starting model for the granitoid complexes is that they are vertical cylinders extending to the middle of the transition between the upper and lower crust (Fig. 5). The mean depth for this transition from the seimic data is 14 km (Drummond 1983).

The interpretation of the gravity anomalies can be separated into two almost independent parts: (1) consideration of the shape and slope of the margin of the granites based on the position of the steepest gravity gradients relative to the granite margin mapped in outcrop/subcrop, and (2) consideration of the relative thickness of the granites based on the relative mass deficiency over the granite.

Margins of the granites

The slope of the granite margin is determined by comparing the position of the granite boundary in outcrop and subcrop with the position of the granite boundary at depth.

The position of the granite boundary in outcrop is given by geological maps. The position of the granite boundary in subcrop has been mapped using three features of magnetic anomalies: 1) the extent of a characteristic granite texture, the texture reflecting numerous linear negatives due to fractures in images of the first vertical derivative; 2) the abrupt change in amplitude of short-wavelength (<1 km) anomalies from low amplitude over granite to much higher amplitude over greenstones; and 3) at wavelength greater than 2 km, the extent of lows in reduced-to-the-pole first-vertical-derivative anomalies.

In most areas, the granite margin is relatively steep, so the average position of the granite margin at depth is given with sufficient precision by the maximum gradient of the gravity anomaly. The maximum gradient has been determined from 20 $\mu m.s^{-2}$ contours. At the margin of a Pilbara granite, the gravity gradient has a horizontal extent of about 10 km, so the position of the maximum gradient is adequately defined over all the land area, both where gravity station spacing is 5 km and 11 km. Figure 6 shows the line of maximum gravity gradient overlaid on the 50 $\mu m.s^{-2}$ contours.

Figure 7 gives the position of the granite boundary in outcrop and subcrop, and this inferred average position of the granite margin at depth. Where the granite margin at depth lies over outcropping or subcropping granite then the greenstone dips under the granite, and where it lies over greenstone the granite dips under the greenstone.

For the whole study area, the granite margins dips under the granites and under the greenstones for approximately equal distances. From this it is inferred the average dip on the granite margins is vertical. This conclusion is strong evidence against the outcrop/subcrop level being near the top or the bottom of the granite bodies on average.

In general, the lines representing granite margin at depth are smoother than the lines representing granite outcrop/subcrop. The outcrop/subcrop surface is likely to be cutting the granite bodies at different and near random positions between the top and the base of the bodies, so the granite margin complexity at outcrop/subcrop level, would be similar to that at a slightly different depth, say at a depth of 5 km below the surface. Hence the apparently smoother shape of the granite margin at depth, relative to margin of the granite outcrop/subcrop, is unlikely to be real, and is likely to be due solely to the averaging effect of the gravity potential field.

Traditionally the modelling of the sides of the granite is done using the position of the margin of the granite at the surface, and the gravity gradient, and finding a 2D or 3D granite shape whose gravitational anomaly is the same as that observed. As a synthetic example let us take a granite whose outcrop shape is a hexagon, and where the gravity maximum gradient has a smoother shape - that of a circle with the same area (Fig. 33). Let us model the granite as two layers of equal thickness. The top layer has the shape of the hexagon observed at the surface. Then to get the maximum gradient as a circle not a hexagon, the basal layer of the model has to have a shape similar to the hexagon but positioned so that it is a mirror-image of the outcrop hexagon across the circle (Fig. 33). However, if we accept that the maximum gradient of the gravity is a smoothed measure of shape at depth, it is unlikely that the shape of the bottom layer is always a mirror image of the outcrop across the maximum gradient. Hence *detailed* modelling of a granite's shape at depth using the granite margin and the gravity gradient will give incorrect results.

The preferred method of interpreting and displaying the granite margin data is to map the boundary of outcrop/subcrop, and the margin of granite at depth using the maximum gravity gradient.

Where the gravity gradient maximum is systematically displaced from the outcrop/subcrop of the granite margin over a significant distance (>20 km) there is strong evidence for a consistent and significant dip on the granite margin. For instance the margin of the Kurrana Granitoid Complex (A of Fig. 7) at outcrop/subcrop is generally within the maximum gravity gradient; the granite has an average width of 18 km at the surface and 24 km at depth. The margin of the Portree Granite (B of Fig. 7) at subcrop is generally outside the average gravity gradient; the granite has an average width of 24 km at the surface and 19 km at depth. The main area where the granite margin has a significant slope is the southeastern margin of the Carlindi and Muccan Granitoid Complexes (C

to D in Fig. 7). Here the greenstone belt dips under the granite.

Depth to the base of the granites

To calculate the depth to the base of the granites, assumptions have to be made – either the average density contrast between granites and mafic volcanics/sediments, or the thickness of one or more granites. The assumption that is basic to the following discussion is that a large number of granites have bases at the same depth. A base of 14 km is assumed in the model adopted here. If this depth is incorrect, then the densities and depths derived can be linearly scaled to the new depth value.

Figure 7 shows the residual gravity anomaly and the areas with sufficiently negative anomalies that the granites are thought to have a base at 14 km. In the eastern part of the area, the non-granite material in the upper crust is greenstones with a high proportion of mafic lavas. The difference in mean gravity anomaly over the deeper granites and that over the average greenstone is 450 $\mu m.s^{-2}$. For a density difference extending to 14 km, this relationship implies an average density difference of 0.077 $t.m^{-3}$ between granite and greenstone. In the western part of the area, the non-granite material in the upper crust is predominantly sediment. The difference in mean gravity anomaly over deeper granites from that over average sediment is 250 $\mu m.s^{-2}$. For a density difference extending to 14 km, this relationship implies an average density difference of 0.043 $t.m^{-3}$ between granite and sediment.

For each of the two areas, estimates of the thickness of the granite can be scaled from the observed anomaly. Figure 8 shows information on granite depths. About 2/3 of the area's granites are thought to extend to the base of the upper crust - those with calculated bases of 12 km or greater. Over much of the remaining area the granite thicknesses are calculated to be 6-12 km. There are few extensive areas of thin granite – e.g. Strelly Granite (A of Fig. 8), and on the western part of the project area (area B of Fig. 8). Over some 'granite' areas there is geological, magnetic, and gravity evidence for extensive areas of mixed granite/greenstone rock; the larger of these areas are identified in Figure 8. The thickness of these bodies is not known, but there is no reason for them to extend to the base of the upper crust.

The approximate thickness of the granitoid complexes and greenstone belts can be determined by modelling the gravity gradient between them. The granitoid complex was represented by a three dimensional prism, a body that in plan has the shape of the granitoid complex (as given by the inflection of the gravity anomalies), has vertical sides, and a constant density contrast with the surrounding greenstone belts. Profiles were drawn across the margin where: 1) the gradient was steepest; 2) there was relatively good gravity field control by 5 km station spacing; 3) the margin was near linear; and 4) the greenstone belt was relatively wide so the anomaly tails on both sides of the margin were observed. Figure 36 shows that the model of granitoid complex and greenstone belt boundary with a model base at 14 km gave an anomaly that is consistent with the gravity grid to within the accuracy of the 5 km observation spacing.

The depth to the base of greenstone belts and granites can be very approximately be estimated from the difference in the two crustal columns in gravity anomaly and mean density. The thickness of the bodies (h), relates to their density difference (dc), and gravity anomaly difference (dg) by the formula for the gravitational attraction of a slab: $dg = 0.4186.h.dc$. However the mean density of the greenstone belts at the surface, and the change in density difference with depth are poorly known. The following calculation use surface densities of granite 2.65 $t.m^{-3}$, sediment of 2.7 $t.m^{-3}$, mafic lavas 2.9 $t.m^{-3}$, felsic volcanics 2.65 $t.m^{-3}$ and ultramafics 3.05 $t.m^{-3}$. At about 21.4°S 118.2°E there is a gravity difference of 300 $\mu m.s^{-2}$ between granite and Mallina Group sediments, giving a calculated thickness of 14 km. In the eastern part of the area centred on 21°S 120°E the largest gravity differences are about 650 $\mu m.s^{-2}$. The greenstone belt in this are is a mixture of mafic and felsic lavas, sediment and ultramafic rocks, and is estimated to have a mean density of 2.80 t.m-3, giving a very unreliable thickness of 10 km. In both areas the gravity highs are narrow, so the measured range in gravity is too low, and the thicknesses are an underestimate.

An alternative method is to use a three dimensional model of the boundary between granite and greenstones to compare the calculated to observed anomalies. The modelled bodies averaged 50 km in diameter, and had a 0.1 tm^{-3} density difference to 14 km depth, giving an anomaly amplitude of about 400 $\mu m.s^{-2}$. The results of the modelling show that when three dimensional effects are taken into account, then the density contrast between the granites and greenstone averages about 0.1 $t.m^{-3}$, with exception of density differences of about 0.2 $t.m^{-3}$ in the area of the greenstone belt south of D in Figure 7. This 0.1-0.2 $t.m^{-3}$ seems compatible with the densities given above.

Conclusions

In general the shape of a granitoid complex margin at the surface is more convoluted than the line of maximum gravity gradient, but with the same mean position, so on average the side of a granitoid complex is near vertical. The gravity anomalies are consistent with about 2/3 the granitoid complexes having a base at the base of the upper crust at 14 km, and about 1/3 having a base at a depth of between 12 and 6 km.

Quantitative analysis of gamma-ray spectrometric surveys for solid-rock geological mapping

Spectrometric surveys over the north Pilbara region

Early airborne spectrometric surveys over the Pilbara Craton were at 1.5 km flight line spacing, 150 m ground clearance and 1.7 litre detector crystals. These surveys are not considered further in this record.

Subsequently more detailed surveys were carried out over most of the north Pilbara region at 400 m flight line spacing, 80 m ground clearance and 33 litre detector crystals. Details of the later surveys are as follows.

Table 1. Airborne geophysical surveys over the north Pilbara region

Survey No	*Survey name*	*Operator*	*Contractor*	*Date*
P636	West Pilbara	AGSO/ WAGS	Tesla	1995
P648	Middle Pilbara	AGSO	AGSO	1996
P649	Marble Bar	AGSO	AGSO	1996
P651	Goldsworthy	AGSO	Stockdale /Kevron	1996
P656	East Pilbara	AGSO	Kevron	1996

The results of these surveys were conventionally reduced by the airborne group using aggregate counts for each peak, and grids were calculated for total count (TC), and the concentration of K, Th and U (Richardson 1997). In calculating the concentrations of Th and U, it was assumed that the breakdown products of these elements were in equilibrium. The grids for the various areas were subsequently joined together to form one grid. Survey P649 had the best crystal calibration to give absolute concentrations of elements, so the scale and datum of the grids of the other surveys were adjusted until they had the best average match with P649 along the narrow band of overlap. Each match was at both high and low concentrations on land. The parts of the images over the sea were not matched, because the matching over the sea did not give the same result as matching the low concentrations over land, and the land matching was considered more important. Matching of levels appeared to be more accurate by comparing grey-scale than pseudocolour images.

The north Pilbara region is a suitable area to discuss interpretation in areas of outcrop because the exposure is good, the region contains a wide range of rock types, and there are few problems with regolith, soil or terrain.

In the following analysis the image processing and scattergram preparation were carried out in ERMapper version 5.2

Description of methods of analysis

There is considerable information content in a modern spectrometric survey, which should give us quantitative information on the chemistry of outcropping rock types. The effects of soil are not considered here because soil appears to be poorly developed over the solid rock area of the north Pilbara region and the flanks of the Hamersley Basin. The effects of soil are discussed by Dickson & Scott (1997).

Potentially the spectrometric data have a higher information content than a magnetic survey, because the data are quantitative and there are three channels. This quantitative factor is important - the observed values in a spectrometric survey relate to the absolute concentration of elements in the area being observed, while the observed values in a magnetic survey relate to the relative magnetisation of the observation point to surrounding points.

Commonly, the interpretation of spectrometric data involves no more than the subjective visual classification of colour images; either images of concentrations of individual elements or images of the three elements combined in a RGB composite image. This interpretation method does not extract the maximum information from the data.

In this section I wish to discuss, with reference to the Pilbara, the question - how do we extract the maximum information from the spectrometric dataset in solid rock outcrop areas? The data are essentially five dimensional, the variables being K, Th, U, latitude, and longitude. A good analysis would:

- utilise the absolute calibration of the data,
- the scheme would be a quantitative, rational classification relating to geology,
- allow for the different measurement accuracy's of K, Th, and U, and
- identify areas of one composition, and area boundaries, as an aid for mapping.

RGB and HSI composite images. Commonly the spectrometric data are displayed as separate pseudocolour images of K, Th and U, and a composite K-Th-U image in red-green-blue (RGB) colourspace. The RGB composite image is illustrated in Figure 9a. These images are quick to prepare, and express the main features of the data, so they will continue to be the primary display of spectrometric data. However, they cannot express all the information within the digital dataset. There are several major problems with the composite RGB image.

- Information of the absolute concentrations of the elements is lost in non-linearly transforming observed concentrations to the 0-255 range for display.
- The non-linear transformation is different with the different elements, so, as the average elemental concentrations increase, one hue reflects different ratios between elements.
- The K-Th-U values tend to correlate, so at high and low concentrations the colour tends to be near black and near white (saturation is dominant), the darkness expressing distance along the average correlation path, not differences from this path, while for middle concentrations of the elements there are bright colours (hue is dominant) expressing differences from the mean path, but with poor information on distance along the path.

The hue within the RGB composite image can be more clearly displayed by transferring the colours in RGB colourspace to hue-saturation-intensity (HSI) colourspace, and decreasing the importance of saturation and intensity (Milligan and Gunn 1997). However, the resulting image (Fig. 9b) is misleading, because the different non-linear transformations of K-Th-U from observed concentrations to the 0-255 range for display, results in hue representing different K-Th-U ratios for different elemental concentrations.

Multiple-class classification methods. The multiple-class classification of a dataset is the process of sorting pixels of the dataset into a finite number of classes, the pixels of each class having similar K-Th-U values. In the K-Th-U system there are 3 bands of data, so the data can be considered to be points in 3-dimensional space, and classification is the process of identifying clumps of points within this 3-dimensional space (classes), and assigning pixels to the nearest class. There are two methods of classifying data. In *unsupervised classification,* the computer determines the location of the classes on the basis of preset parameters. Class centres and class extents are sub-equal. The classes may not correspond with continuous areas on the ground. In *supervised classification* (Fig. 9f), the classes are based on training regions defined by the interpreter. This is an advantage because the training regions can be checked on the ground. However, this methods results in a very unequal distribution of class centres and class extents. In both classification methods, clumps of data points, and hence classes, mainly occur along the path of average geochemical variation, so the two approaches mainly express distances along this path. Distances from this average variation path are poorly expressed, although these are often of greatest interest to the

interpreter. Because of this, the multiple-class classification methods were not pursued further.

Principal components. In gamma-ray spectrometry there are 3 bands of partly correlated data. In three-dimensional (K, Th, U) space, the data-points will define an ellipsoid. The original data points can be expressed with new values in an orthogonal coordinate system defined by the long, medium and short axes of this ellipsoid - the first, second and third principal components. Figure 34a shows in two dimensions this change in coordinate system. The advantage of expressing the data as principal components is that the data in the three bands are now non-correlated - independent of each other. The first principal component (PC1) measures the greatest variation in the data. The second principal component (PC2) describes the largest amount of variation that is not described by the first component. The third principal component (PC3) describes the remaining variation; that not described by the first or second component.

Each principal component is determined using data from the three bands. This has two disadvantages in using spectrometry data of K, Th and U.

1) For a rock of basaltic composition, with low concentrations of these elements (K = 0.3%, Th = 1.5 ppm, U = 0.5 ppm), and average radon near the aircraft, the percent standard deviation of the determinations are 32, 46 and 160 respectively (B. Minty pers comm) for 33 litre crystal at 80 m above ground and traditional data reduction. The large percentage standard deviation in U leads to undesirably large uncertainties in all three principal components.

2) There is no difficulty in understanding the geological meaning PC1, but the geological meaning of PC2 and PC3 are obscure.

In analysing spectrometric data where the crystal volume was low, and so elemental percentage uncertainties high, it is advantageous to carry out the analysis using the four channels - total count, K, Th and U. For these data the principal component method may be desirable.

Components. A different type of component analysis is thought to be optimal in analysing spectrometric data of K-Th-U. In this component analysis, the first component (C1) is similar to PC1 in that it is a measure of distance along the long axis of the ellipsoid - the path of average geochemical variation. The second component (ΔTh) is the residual of Th from this axis (Fig. 34b), and the third component (ΔU) is the residual of U from this axis (Fig. 34c). The disadvantage of this analysis is that it is slow to implement. The advantages are as follows.

(1) For most major rock types C1 has a negligible component of U, so can be determined from K and Th. Hence the first two components C1 and ΔTh are not effected by the high percentage standard deviation in U.

(2) The components ΔTh and ΔU have a known geological meaning.

(3) The whole analysis parallels natural geological subdivision and analysis.

The procedure for carrying out component analysis is as follows:

- Scattergrams are prepared for several compact areas of each major rock type.
- Using these scattergrams, equations in K, Th and U are determined for planes in K-Th-U space that separate the major rock types.
- Equations are determined in K and Th measuring distance along the path of average geochemical variation (C1) for each rock type.
- Equations are determined to calculate deviations of each pixel (ΔTh and ΔU) from the path of average geochemical variation for each rock type.
- Images are prepared for each component and for each rock type, with the area that is not that rock type masked out.

Analysis of the Pilbara exposures in terms of component analysis

Separation of pixels into the major rock types

The K, Th and U extent of the major rock types was determined by identifying major areas predominantly of one rock type (Fig. 1), and preparing scattergrams of Th vs K, U vs K and U vs Th for each of these areas (Fig. 10). In most rock types there is a significant positive correlation of K with Th (Fig. 11). There is generally a poorer correlation of U with either K or Th.

When the extent of the major rock types are plotted on a scattergram of K vs Th (Fig 10b), it is found that the field for mafic igneous rocks and the field for felsic igneous rocks do not overlap significantly with that of other rock types, but that the field for sediments corresponds with part of the field for intermediate igneous rocks (Fig. 35). Hence using K and Th, the spectrometric data can be used to subdivide the pixel data into three major rock types groups - mafic igneous, felsic igneous, and a combination of intermediate igneous and sediments.

For each of these major rock types, expressing K-Th-U data as components has brought out the main features of the dataset - the distance of the rocks along the average geochemical evolution path, and deviations from this path. These components are determined quantitatively. These features can be seen in the RGB image, but only when you know what to look for, and only qualitatively.

Illustration of component analysis for three major rock groups

For each of the major rock groups, equations were calculated by hand to define the margins of the rock group in K-Th-U space, and to calculate the components C1, ΔTh and ΔU for each pixel. It is considered important that the components are linear functions of K, Th and U, because this is more consistent with the error structure of these quantities. (Ratios of the elements were not used.) Maps were prepared for each component for each major rock group - sediments, and mafic, intermediate and felsic igneous rocks.

Mafic igneous rocks. Analysis of spectrometric data from mafic flows is complicated by: (1) the outcrop width of the flow being narrower than pixel size; (2) differences in the composition of adjacent flows; (3) the presence of sedimentary and felsic rocks intercalated with the flows; (4) terrain effects of float material moving down-slope off strike ridges; and (5) by larger analytical errors due to relatively low concentrations of K, Th and U. The example used here is the Coongan Syncline. The K-Th-U data are displayed as the traditional RGB composite image in Fig. 12a. C1, a measure of mean geochemical evolution (how mafic the rocks are)(Fig. 12b), shows significant differences across strike both regionally and locally. ΔTh (Fig. 12c) shows that basalt sequences of different ages differ from one another in the amount of Th relative to the mean geochemical evolution path of all the Pilbara basalts. The ΔU (Fig. 12d) image has errors due to levelling the aircraft data (recognised as east-striking bands of high and low), but it is thought to also show localised highs

and lows due to post-emplacement geochemical mobilisation (possibly by hydrothermal solutions). Note the greater noise in Figure 12d, relative to Figures 12b & c, due to the lower precision in the mapping of U.

Intermediate igneous rocks. Figure 13 shows an example of component analysis of intermediate igneous rocks from the Hamersley Group on the Pinderi Hills and Cooya Pooya 1:100 000 sheet areas. The RGB image (Fig. 13a) gives an excellent separation of the layers within the sequence, giving qualitative information both on the distance along and distance from the average geochemical path. C1 (Fig. 13b) gives an equally good separation of layers, based on the distance along the average geochemical path. ΔTh and ΔU (Fig 13c & d) give quantitatively the deviation of the rocks from the mean geochemical variation path. At several scales there are packets of rocks with similar deviations from the mean variation path. This is consistent with the model that adjacent rocks have a high probability of being related geochemically. There are areas where ΔTh and ΔU values differ from those along strike, possibly because of post-emplacement geochemical mobilisation.

Sedimentary rocks. The RGB composite image (Fig. 14a) for the Mosquito Creek Belt mainly reflects variation of distance along the mean geochemical path. The C1 grey-scale image (Fig. 14b) shows this equally well, but more quantitatively. Images of ΔTh and ΔU (Fig. 14c, d) show some changes consistent with statigraphy boundaries, and some changes independent of them.

Felsic igneous rocks. The data for all felsic igneous rocks can be considered as a first approximation to belong to a single differentiated system. The RGB composite image (Fig. 9a) shows the amount of geochemical evolution as a change from dark (for more mafic granites) to light (for more felsic granites), and deviations from this mean evolution as hue. Qualitative estimates of the amount of evolution are possible for high and low concentrations, and estimates of the differences from the mean path are possible only for intermediate values of evolution. The C1 image (Fig. 9c) shows quantitatively the distance along the mean geochemical evolution path. Images of differences from this mean path (Fig. 9d) show discrete areas with uniform values and abrupt boundaries: these are thought to delineate the plutons that make up the granitoid complex.

Evolution paths for felsic igneous rocks

Granites are an important subject of spectrometric analysis, because they are everywhere difficult to map using air-photographs or satellite images. In spectrometric images, there is information as to granite evolutionary path, the amount of differentiation along the mean path, and the deviation of the granite from this mean path. Granites have relatively high K, Th, U contents, so percentage measurement errors are relatively low - for a rock of composition K=2.5%, Th=18 ppm, and U=4 ppm, the percent standard deviations for K is 8%, for Th is 10% and for U is 34%.

The granites of the Pilbara were divided by Hickman (1983) into three broad types based on differences in chemical composition and age - his Agm, Agp, Agc. Using the extent of these types shown by field mapping, the types are distinguished here as occupying different volumes in K-Th-U space, and having different trends within that space. One of his types (Agp) can be subdivided into two types on the basis of the spectrometric data. Table 2 lists the characteristics of the four granite types (G1-G4) recognised in this report.

Table 2. Four granite types

Granite type	G1	G2	G3	G4
Hickman symbol	Agm	Agp	Agp	Agc
Relative age	old	intermediate	intermediate	young
Character	mafic	porphyritic 1	porphyritic 2	felsic
Th content (ppm)	<15	15-23	<23	>23
U content (ppm)	< 3	<3	>3	any
Differentiation	increasing K	increasing K	increasing U	increasing Th&U

The geographical distribution of the four granite types is shown in Figures 9e and 15a. The granite types occur in compact areas, consistent with these subdivisions being real.

Figure 16 shows scattergrams, which are the aggregate of points derived from four granitoid complexes - Mount Edgar, Corunna Downs, Yule and Shaw Granitoid Complexes (Fig. 1). Overall, each plot shows a broad band of geochemical variation, and at a primary level this band can be considered to be the differentiation path for all granites. This mean path was used to calculate Figure 9b and c. However as stated above, the granites can be subdivided into four types - G1-G4. The extent of the four types in K-Th-U space is shown on the scattergrams as black lines. The scatter of points for each granite type shows that each type has a range in composition. The axis of this scatter (shown as a red line in the figure) is interpreted to be the differentiation path (geochemical variation path) for that granite type. The separation of types G3 and G4 is more clearly shown for the Shaw Granitoid Complex data (Fig. 17).

Figure 18 shows scattergrams with the four granitoid complexes displayed separately. The differences between the scattergrams is due to a combination of the following factors:

- differences in the proportion of mafic versus felsic compositions in the granitoid complexes,
- different mean compositions for the same rock type,
- different mean geochemical variation paths, and
- differences in the amount of scatter around these mean paths.

An example of different mean composition is, for the more mafic granites, the lower Th in Mount Edgar Granitoid Complex (Fig. 18d) relative to other granitoid complexes. An example of different differentiation paths, is for Th >20 ppm, the different pattern of K vs Th for Corunna Downs Granitoid Complex (Fig. 18c) relative to Shaw and Yule Granitoid Complexes (Fig. 18a, b).

There is a tendency for later granite types to be located near the middle of intrusion of earlier types. An illustration of how the spectromentric data may be used to draw this conclusion is given in Figure 15.

Geochemical maps

It is possible to use the K-Th-U data to map rock types over the whole of the outcrop area. The method is in part a *multiple class classification* in that the map consists of numerous

classes. It is also in part an extension of the *component* method, in that the major class divisions are the major rock types, and the classes defined are based on the values of the components for the relevant major rock type.

Figure 35 gives the legend for the geochemical map of Fig. 9g. Each major rock type has been given a range of colours:

- ultramafic igneous rocks - purple
- mafic igneous rocks - green
- intermediate igneous rocks and sediments - brown to yellow
- felsic igneous rocks - red to magenta.

To make the geochemical map of Figure 9g as useful as possible for lithological mapping, each major rock group has been subdivided, with lots of classes in the direction of component 1, and fewer classes in the direction of ΔTh.

This type of geochemical map is not a geological map, and can never be one. It does not allow for regolith effects. Boundaries are not coincident with geologial map boundaries because they are based only on only three elements, are gradational not abrupt mappable boundaries, are displaced because of movement of float on hill-sides, or because of geochemical mobility.

However, a geochemical map is potentially an extremely powerful way of

- displaying the K-Th-U data
- subdividing K-Th-U data into geologically meaningful classes
- fully utilising the absolute concentrations.

Importantly, it is a useful starting point in displaying spectrometric data in a way that it can be compared with a geological map to highlight areas which have anomalous compositions, and hence should be checked by either field work, or using other remote sensed data sets.

Conclusions

In areas of outcrop, spectrometric data can be used to map the extent of three major rocks types - mafic igneous, felsic igneous, and a combination of intermediate igneous and sedimentary. Within a major rock type, there is a significant correlation between elements, at least between K and Th. These correlated data can be expressed as uncorrelated components: C1 expresses distance along the geochemical variation path, C2 anomalous Th, and C3 anomalous U. Maps of these components extract useful quantitative geological information from the spectrometric data that should be helpful for mapping. In particular:

- Mafic and intermediate flow sequences can be subdivided into composition types with different thorium values, with abrupt breaks between the composition types.
- The felsic intrusive rocks can be subdivided into four granite types, each type with a different mean composition and differentiation path.

Major crustal fractures within the Pilbara Craton

Geological mapping has lead to the recognition of a major shear zone in the western part of the north Pilbara region - the Sholl Shear Zone. The question addressed in this chapter is what geophysics has to offer in: (1) mapping the full extent of this shear zone; (2) in mapping additional shear zones; and (3) determining the nature and age of these shear zones.

Northeast to east trending shear zones

The Sholl Shear Zone crops out as isolated exposures about 1 km wide, of mylonite and mylonite gneiss, separating dissimilar rocks. The exposures occur along a distance of 130 km. Magnetic anomalies RTP show the Sholl Shear Zone as a gently curving zone with a strike length of about 250 km (A-A in Fig. 19). Along its length, the shear truncates geological structures, but there is no change in the general magnetic anomaly texture across the shear. The shear zone is generally marked by 1-4 subparallel elongate narrow magnetic anomaly highs, and/or the truncated edge of a broad anomaly. At the shear, gravity anomalies generally have a small gradient or inflection.

Other inferred shears with similar character can be identified on magnetic and gravity anomaly maps. Their extent is shown in Figure 19 as brown lines. Each inferred shear has the following characteristics:

- There is generally a change in geology across the shear along its length.
- The shear is marked by narrow, elongate magnetic highs consistent with lithological layering parallel to the shear. Some of the highs may be due to elongate fault slivers within the inferred shear zone.
- The shears correspond with a gravity anomaly gradient.
- In areas where the basement is mapped by short-wavelength magnetic anomalies, the shear is seen as a continuous structure, and the interpreter has reasonable confidence that the feature is real. In areas where short-wavelength magnetic anomalies due to the basement are not imaged because of too great a distance between the basement and aircraft, then the shear is inferred from the truncation of large anomalies. There is no proven continuous fracture in these sections of shear, so the mapped shear may be a chance alignment of unrelated body margins.
- The inferred shears in many places correspond with the margins of granitoid complexes.

These inferred shears are thought to have been established early in the geological history, because they appear to control the more gently curved margins of granitoid complexes. The shears are unconformably overlain by Fortescue Group rocks. From the length, continuity, and relatively gentle curves of these shears, they are inferred to have a steep dip, to extend down well into the upper crust, and their movement to have a significant strike-slip component.

The Mallina 'Shear Zone' (BB of Figure 19) is marked as a shear zone on the Sherlock 1:100 000 sheet (Smithies 1996). I do not believe that it is a *major* shear zone of the type described above, because the rock on the two sides of the fault is mapped as the same, and magnetic anomalies in the area of the fault are flat. Structural work suggests that the 'shear zone' is a late (~2780 Ma) high-level extensional fault system associated with significant gold occurrences (Richard Blewett, pers comm 1998).

Krapez & Eisenlohr (1998) and earlier workers subdivide the North Pilbara region into tectonostratigraphic domains, with the domains separated by transcurrent northeast-trending lineaments. Their three lineaments in the west correspond with shears mapped geologically, and in areas of cover with shears mapped using magnetic anomalies (Fig. 19). Their two lineaments in the east (Mulgandinnah and Lionel Lineaments), may be consistent with geologically mapped features in areas of outcrop, but in areas of cover the magnetic images show that they are unlikely to exist, because they do not correspond

with a lineation, and where they cross lithological basement features the features are not displaced.

NNW trending faults

The major NNW-trending gravity gradient in the east (WW in Figure 19) was thought by Wellman (1978) to be due to a major change in crustal thickness and mean crustal density occurring at the western margin of the Pilbara Craton. Subparallel with this craton boundary are linear features in the magnetic and gravity anomaly images. These are thought to be faults associated with this craton boundary. On Figure 19, gravity gradients parallel to the boundary are given in magenta, and gradients and truncations in the RTP magnetic image are shown in green. These magnetic and gravity gradients and truncations occur in three bands, 15-25 (XX in Figure 19), 40-50 (YY) and 65-80 km (ZZ) from the Pilbara Craton margin. These bands may be due to continuous or discontinuous features in the crust. The features are under Mesozoic cover to the north. In the south feature XX corresponds with faults in the Proterozoic rocks that bound rocks of different composition, and a flexure in Permian rocks. Feature YY is thought to be due to faults in the granite/greenstone rocks, under unfaulted Hamersley rocks. Feature ZZ corresponds in part with co-linear elongate faults cutting both Hamersley rocks, and the greenstone and granite rocks, with a total dextral displacement of 6 km.

Interpretation of the magnetic anomalies in terms of geological features

There are two ways of using magnetic anomalies.

1) The magnetic anomaly features can be mapped using symbols to show their amplitude, character and extent. This method has the advantage of objectively describing the anomaly pattern, independantly of whether or not the bodies causing the pattern are understood. A disadvantage of this method is that it does little to increase ones knowledge of the geological significance of the anomalies.

2) Magnetic anomalies are interpreted in terms of geological features, and standard geological symbols (lithological boundaries, faults, folds etc) are used to describe the magnetic features. This method is the one used in this report. This method has the advantage that the anomalies are directly interpreted in terms of the required information (geology). Disadvantages include: (1) some parts of the interpretation are likely to be incorrect; and (2) the geology causing some of the anomalies is indeterminate, so representation of the anomalies are omitted from the interpretation map. A major feature of low-level aeromagnetic surveys is that the images show texture (stippled, smooth, lineated) of units. This information is generally not reported directly, but it is a major input into the location and confidence of the rock-type boundaries.

The following geological symbols were used in the interpretation: fault, rock-type boundary, positive fracture, negative fracture, dyke, compositional band. The following table shows how the linear features are distinguished using the character of the magnetic anomaly.

Table 3. Interpretation of elongate magnetic anomalies

	Compositional band	Faults, fractures	Dykes
Wave form	complex	simple	simple
Apparent body width	narrow to wide	wide	narrow
Continuity	continuous, segmented	continuous	continuous
Magnetisation	normal or reverse	often zero	various
Adjacent anomalies	subparallel dissimilar	sub-parallel or orthogonal similar	sub-parallel similar

Interpretation was carried out at 1:100 000 scale using double clear plastic on computer-plotted images. The images were prepared as follows. The initial grid values are of total magnetic intensity with the grid parameter based on latitude and longitude in Australian Geodetic Datum 1966. These grids were converted to ones based on Universal Transverse Mercator, World Geodetic System 1972, using bilinear interpolation to calculate new pixel values. The Intrepid computer programs were used to calculate grids of magnetic anomaly reduced-to-the-pole (RTP), and grids of the first vertical derivative of magnetic anomalies RTP. Four maps were printed for each 1:100 000 sheet area over the area of 400 m flight-line spacing coverage:

1. Magnetic anomalies RTP in pseudocolour, with northwest sun-angle shown as darkness in the image. This image type was found to be of little use for detailed interpretation.

2. Northwest sun-angle as greyscale image. This was the clearest image for short-wavelength anomalies, but it was little used because of its directional bias. This image is an important check on visualising the first-vertical derivative image.

3. First vertical derivative of magnetic anomaly as grey-scale image. About 90% of the interpretation is based on this image, because it is unbiased in direction, and it favourably enhances short-wavelength anomalies over all areas except those with steep medium-wavelength gradient.

4. Northwest sun-angle of first vertical derivative of magnetic anomaly as grey-scale image. This was used to map features and determine texture in areas with steep medium-wavelength gradient.

The results of this short-wavelength magnetic anomaly interpretation will be incorporated into the 1:500 000 maps of solid geology of the north Pilbara region that are being prepared. The use of this information in areas of exposed geology depends on resolving issues of apparent conflict between field geology, spectromentric data and magnetic data.

Direction of magnetisation of dykes

The magnetic image reveals many dykes, some of these have been field mapped. In magnetic images the dykes commonly occur as regularly spaced sub-parallel swarms with all dykes having a similar direction of apparent magnetisation and similar magnetic amplitude. Dykes are assumed to be nearly vertical so the direction and strength of apparent magnetisation on the RTP image is thought to be controlled by the strength of the induced magnetisation (which is in the direction of the present Earth's magnetic field), and the strength and the direction of the remanent magnetisation. A map was prepared (Fig. 20) showing the apparent direction of magnetisation of the segments of each dyke. The dykes were divided into 7 classes with different apparent direction of magnetisation using an image of the first vertical derivative of RTP magnetic field. The classes range from 'a' to 'g' in regular steps depending on the relative size and position of the positive and negative anomalies due to the dyke; with 'b' normal polarity - a symmetrical mainly positive anomaly, 'd' horizontal magnetisation with an equal magnitude positive to the north and negative to the south, and 'f' reverse magnetisation - a symmetrical mainly negative anomaly.

The more extensive dyke swarms cut, and are therefore younger than the Hamersley Basin rocks. Some of these dykes have been interpreted as elements of the 755+-3 Ma Mundino Well Dyke Swarm (Wingate et al. 1998). The dykes giving anomalies on magnetic maps are thought to be post metamorphic, because metamorphism substantially reduces both induced and remanent magnetisation. Based on the prior geologial mapping, these strongly magnetic dykes are mainly of mafic compositions; the felsic dykes are relatively weakly magnetised.

From the variation in strike, spacing and direction of magnetisation, the dykes are interpreted to belong to a large number of separate swarms, some of regional extent and some local. Most of the longer dykes are gently curved in one direction, consistent with the crust's horizontal-stress at the time of intrusion varying gradually and linearly over the region. An exception is the long reverse-magnetised dyke in the eastern part of the region; it has a shape analogous to one cycle of a sine wave. For this dyke, a local horizontal stress seems to influence the dyke direction, and the origin of the stress must be at a distance from the dyke comparable with this wavelength - 100 km. For all these dykes the position, strike and spacing of the dykes is thought to be controlled largely by the regional lithospheric stress at the time of dyke injection, and the dyke injection mechanism. At a very local scale the dyke may intrude a pre-existing fracture, but the influence of these pre-existing fractures on the location of the dykes must be minor.

Total vertical deformation after 2780 Ma: Map of depth to the base of the Fortescue Group

A map has been prepared of the altitude of the base of the Fortescue Group relative to the present land surface (Fig. 21) using the published maps at 1:250 000 scale. The zero contour is at the location where the base of the Fortescue Group rocks outcrop. Contours of the altitude of the base of the Fortescue Group below the land surface are mapped using the thickness of Fortescue Group rocks on sections in 1:250 000 maps, and the outcrop trace of the formation boundaries. Contours of the altitude of the base of the Fortescue Group above the present land surface are inferred from the other contours.

The resultant contour map has slopes that are generally between 1:5 and 1:30. Slopes are relatively steep in the mobile area near the margins of the Pilbara Craton and over the greenstone synclines between the granitoid complexes, and are relatively gentle over the granitoid complexes.

Fortescue Group sediments and flows generally exibit regional changes in thickness, which often do not correspond to present day structure. Thus, to a first approximation, the Fortescue Group rocks were laid down on an erosion surface with a relief of less than 1 km. Subsequent to deposition of the Fortescue Group, the contour map shows that there has been a rise of the granitoid complexes relative to the greenstone belts of up to 3 km. The simplest explanation for the relative vertical movement of the granite and greenstone rocks is for the driving force to be the difference in density of the crustal columns. This raises the question of the crustal strength at the time of the vertical movement. It would be interesting to know whether this movement occurred at a time of normal geothermal gradient, or at a time of higher geothermal gradient - such as may have occurred when the Hamersley lavas were extruded.

Susceptibility measurements

A field program was carried out in the period 9-25 May 1997 to determine the susceptibility of the major rock types in greenstone belts of the north Pilbara region. Measurements were on traverses rather than unrelated spot values, because it is the change in susceptibility that produces the magnetic anomaly, not its absolute value. The traverses observed (Fig. 1) were recommended by A. Hickman (GSWA) as providing good access to the major rock sequences, as wel as being on traverses that had previously been geochemically sampled (Glikson & Hickman 1981; Glikson et al. 1986).

The main aim of this work was to identify the rocks with exceptional magnetic anomaly, determine their mean susceptibility and width, and the amount by which the susceptibility deviates from the average value of the surrounding rocks.

Within each traverse, measurements were made on all outcropping rock types. An attempt was made also to keep the sites equally spaced so that the traverse was uniformly sampled. It was considered more important to sample at regular intervals than to identify the rock type at all sites.

Some sites were measured on very small outcrops of fine-grained rock, and the rock type could not be determined.

Measurements were made using a KT-5 magnetic susceptibility meter. This has a sensitivity of 10^{-5} SI units. No correction was made for rock surface unevenness: an unevenness of 1 mm has a correction factor of 1.07, and 5 mm a factor of 1.41. The outcropping rocks are not thought to be weathered relative to rocks at several hundred metres depth; the surface weathering rind is generally very thin (1-2 mm), and surface boulders and outcrops are generally difficult to break because of their freshness. At each site up to 11 measurements were made. The best estimate of the susceptibility of the site was taken to be the median of the measurements at the site. The median was used because the logarithm of the measurements is thought to be normally distributed; use of the mean would bias the estimate too high. The absolute location of most sites was measured using a GPS receiver (Garmin GPS45) set to give metres in Universal Transverse Mercator on datum WGS84. Where sites were relatively closely spaced, the site positions were interpolated between GPS readings by pacing. The results of this work are summarised in a set of plots of traverses (Fig. 22), and for each rock type a histogram of susceptibilities (Fig 23; Appendix 2a).

During the 1996 and 1997 field seasons, AGSO field geologists made susceptibility measurements at most mapping sites. These observations were taken from AGSO's OZROX corporate database by Richard Blewett, have been sorted into the same range of rock types, and are presented in Figure 24, and Appendix 2b. The two data sets have been combined by assuming that the geologists data have an average of 6 readings per site. Appendix 2c and Figure 25 show the combined data.

For the 'greenstone' belts the great majority of susceptibility measurements were in the range $10^{-3.8}$ to $10^{-3.0}$ (SI units). Susceptibilities in this range occurred in all rock types, and it was the dominant susceptibility for the rocks forming the bulk of the 'greenstone' belts - felsic volcanics, mafic volcanics, and sediments.

The distribution of susceptibilities in each rock type is as follows (Fig. 25). Felsic volcanic rocks had the most common value at $10^{-3.3}$ (SI units) with other values lower down to $10^{-4.6}$. Mafic volcanic rocks had values centred closely on $10^{-3.3}$, with some higher values to $10^{-1.2}$ probably due in part to non-recognition of dykes and ultramafic rocks. Ultramafic rocks seem to occur in two ranges $10^{-2.1}$-$10^{-1.1}$, and $10^{-3.7}$-$10^{-2.9}$. Dykes had a similar distribution but based on a smaller sample, a range of $10^{-1.9}$-$10^{-1.1}$ and $10^{-3.3}$-$10^{-3.1}$. For peridotite/gabbro (mainly from Andover Intrusion), the majority of the values were in the range $10^{-1.6}$-$10^{-1.2}$, and the lower values appeared to be associated with obvious felspar. Granites had three peaks of values centred on $10^{-5.0}$, $10^{-3.9}$ and $10^{-2.3}$. The gneiss samples were mainly in the range $10^{-3.8}$-$10^{-3.0}$. Sediments had a mode of $10^{-3.6}$, and were mainly in the range $10^{-5.2}$-$10^{-2.8}$, but there were a few samples of coloured cherts as high as $10^{-1.3}$.

Low susceptibilities of below $10^{-4.5}$ were given by some granites and sediments, and less importantly felsic volcanic rocks and gneiss/schist. Importantly high susceptibilities above $10^{-1.5}$ were given by some ultramafic rocks, dykes, peridotite/gabbro, and chert/red-jaspilite/banded iron formation. The thickness of the high susceptibility bodies was often indeterminable in the field. The few thicknesses measured were in the range 2-30 m for dykes, mafic flows and chert/jaspilite, and 50-200 m for ultramafic composite bodies.

These measured susceptibilities are compared in Figure 25 with the range of susceptibilities given by Clark & Emerson (1991) for these rock types. The agreement is as good for all rock types except granites. In the Pilbara granites give three susceptibility peaks – at $10^{-5.1}$, $10^{-3.9}$ and $10^{-2.3}$, while Clark shows only two peaks about $10^{-3.2}$ and $10^{-1.9}$. Hence the Pilbara measurements show two of the peaks with lower values, and has a third peak of non-magnetic granites not recognised by Clark (1997). Non-magnetic granites have previously been recognised in Cape York Peninsula, Queensland (susceptibility measurements in AGSO's OZROX corporate database).

These susceptibility results are useful in future magnetic modelling, checking rock identity in the field, in confirming the validity for the Pilbara area of most of the Clarke (1997) values, and in extending the susceptibilities of Clark (1997) for granites.

Long-wavelength magnetic anomalies

The distribution of major magnetic anomalies is shown in Figures 26 & 27. The anomalies are of four kinds: (1) Linear anomalies in the greenstone belts with widths of 0.5-1.5 km, and amplitudes of 8000 to 60 000 nT. These anomalies are due to outcropping, steeply dipping layers of either banded-iron formation (BIF) and ultramafics, that are within the greenstone sequence or within fault zones; (2) Anomalies 20 km long and 5-7 km wide of amplitude 1500-2000 nT due to two exposed mafic-ultramafic complexes - the Munni-Munni and Andover Intrusions (A, B of Fig. 28); (3) Irregular short-wavelength anomalies of high amplitude due to Hamersley and Fortescue Group rocks on the southern and western margins of the study area - these anomalies are not discussed further; and (4) Anomalies of amplitude 2000-3600 nT, with a width at half amplitude about 9 km, and a top deeper than 1 km. These major, long-wavelength anomalies are the main subject of this chapter.

Long-wavelength magnetic anomalies occurring over the greenstone belts of the Pilbara Craton can potentially be used to infer the distribution of the causative rock type at depth, and hence the shape of the greenstone belts at depth. Much of the following observations are based on total magnetic intensity reduced-to-the-pole maps. Interpretation has mainly been developed on the basis of two-dimensional models of elongate tabular bodies.

Depth to top. The depth to the top of the bodies causing the long-wavelength anomalies has been determined using the Vacquier method (Vacquier et al. 1951), using the horizontal extent of major gradients. The horizontal extent was measured on contours on the computer screen, using both total magnetic intensity and reduced-to-the-pole anomalies. The mean depths determined are given on Figure 28; they have a mean of about 1.5 km in the west and 2.0 km in the east.

Body width. Many of the major anomalies have a width at one half amplitude of 9 km. Figure 29e shows that a *narrow* (1 km wide), tabular, elongate body at a depth of 2 km has an anomaly width, at one half amplitude, of only 4 km. Figures 29a-d show that a *wide* body of depth 2 km has a body width similar to the anomaly width. Hence these major long-wavelength anomalies with a width at half amplitude of 9 km, are due to bodies with a width of about 9 km.

Depth of base. The depth to the base of the bodies can be determined approximately from the distance apart of the flanking lows, relative to the width of the body. In Figure 29c & d the base of the body is at 5 km, relatively shallow, and the flanking low anomalies are 1.9 body widths apart. In Figure 29a the base of the body is at 14 km, relatively deep, and the flanking low anomalies are about 2.6 body widths apart. For the mapped major long-wavelength anomalies the flanking lows are about 2.6 body widths apart, which is consistent with vertical tabular bodies extending to, or near to, the base of the upper crust. The anomalies are not consistent with the base being relatively shallow. In theory it is possible to have a body with a base at 5 km, and explain the separation of the marginal lows by having the body 8 km wide at the top half, and much wider at the base. However, this model is not possible in the Pilbara because the granitoid complex is immediately adjacent to the high magnetisation body (Fig. 28) and the granitoid complex occupies the space necessary for a wide base. I conclude that the depth to the base of the bodies is likely to be nearer 14 km, than 5 km.

Location. The long-wavelength anomalies are located directly over, and extending over the full width of the major synclines. The margins of the bodies causing the anomalies generally follow the surface contact of the adjacent granitoid complexes (Fig. 28). The anomalies occur directly under the syncline, mainly associated with the De Grey, Gorge Creek and Whim Creek Groups of rocks. In the central eastern part of the north Pilbara region where they are best developed, the anomalies are near continuous and uniform along strike. Elsewhere in the eastern Pilbara Craton the anomalies are isolated segments, of similar properties and dimensions to the more continuous anomalies, except that they are about 20 km strike length. In the western Pilbara Craton long-wavelength anomalies occur over the southern part, each with a strike length of 10-20 km. These bodies are at a shallower depth (averaging 1.5 km), and of relatively low susceptibility, compared with the eastern Pilbara Craton.

Source of magnetisation. The nature of the rock material causing the long-wavelength anomalies is not known with certainty. Many of the long-wavelength anomalies have an amplitude of 2000 nT, a width at one half amplitude of 9 km, and the causative body is interpreted above to extend from 2 km to about 14 km below the surface. One anomaly (A of Fig. 28) has an amplitude of 3600 nT. With these parameters, and if the remanent magnetic component is zero, or has random direction, then the body average susceptibility is generally 0.1 (SI)(Fig. 29a), and up to at least 0.2 (SI). This means that in the body the volume percent of magnetite is about 3%. Susceptibilities observed in the north Pilbara region are reported above in Chapter 7. The three rock types with high susceptibilities are large peridotite bodies and small ultramafic bodies with modes about 0.05 (SI), and banded iron formation in cherts, with a mode about 0.08 and values up to 1.0 (SI). These rock types give similar values outside the north Pilbara region (Clark & Emerson 1991). If the effective remanence is zero, then none of these rock types is reasonable. A peridotite/ultramafic body is unlikely because (a) the susceptibility is slightly too low, (b) it is improbable that the whole of the body is of this rock type with a cross section of 9 x 12 km extending for hundreds of kilometres, and (c) in the area of the greatest magnetic anomaly the residual gravity anomaly is abnormally low. A banded iron formation body, similar to that at the surface, is geologically unlikely because with a susceptibility of 1.0 (SI), and no remanence, the banded iron rock would have to occupy 12% of the greenstone belt at depth, and this is improbable based on known geology determined by surface exposures.

Clark & Schmidt (1994) and Clark (1997) discuss the magnetic properties of banded iron formation in the Hamersley Basin and Yilgarn Block and integrate this work with that on similar rocks overseas. Bedding parallel susceptibility is typically 0.5-2.0 (SI), and the ratio of remanent and induced magnetisation (Q) is typically 1-2. Due to geometrical effects both the susceptibility and remanence magnetisation are much stronger in the plane of the bedding than across the bedding. If we assume that the north Pilbara region banded iron formations have the average values of the above ranges (susceptibility 1.0 (SI) and Q of 1.5), then the apparent susceptibility is 2.5 (SI). If the average apparent susceptibility of the greenstone belts below 2 km is 0.1 (SI) then the BIF would have to occupy an average of 0.1/2.5 = 4% of the volume of the greenstone belt. This seems a bit high, but it is at least possible. The preferred cause of the long-wavelength magnetic anomalies is thin bodies of banded iron formation within the 'greenstone' belts, with enhanced magnetisation below 1.5-2.0 km depth.

Dip. The average dip of the banded iron formations, and hence the greenstone belts, cannot be directly determined because the direction of both susceptibility and remanence is not known. Figure 30 shows that when the total magnetic intensity is reduced to the pole for a magnetic latitude of 80°, then the major anomalies (A-D) are approximately symmetrical, and lows are about 2.5 body widths apart and approximately equal magnitude. This shows that for these bodies the magnetic anomalies are consistent with a near vertical banded iron formation and greenstone belt, with the direction of susceptibility and remanence approximately in this near vertical plane.

Modelling of magnetic profiles. Figure 31 shows modelling of profiles across some of the larger magnetic anomalies. For each profile a single prismatic model was used, with a length approximating the anomaly length. This modelling confirms that the bodies causing the anomalies have the following features: (1) a body width similar to the width of the anomaly at one-half amplitude; (2) a depth to the base of the body of about 14 km; (3) a body top near 2 km, and (4) an average susceptibility of 0.1-0.2 SI.

North Pole Dome. The North Pole Dome (C of Fig. 28) is rather anomalous. The exposed rocks forming the dome are some of the oldest age greenstone rocks (Warawoona Group), and at the lowest level there is a small outcrop of granite. This dome is surrounded, according to outcrop and magnetic anomalies, by deep synclines of greenstone rocks. Because of the domal structure, the granite outcrop, and the dome rocks being about the lowest levels of the greenstone sequence, one would expect that the small granite outcrop to be the exposed part of a granitoid complex underlying the dome. The separation of the surrounding synclines gives a maximum granitoid complex extent of 30 x 35 km. However, gravity anomalies over the dome are only about 100 $\mu m.s^{-2}$ below those over the surrounding greenstone sequences (Fig. 6), so the volume of granite under the dome is very small - a small thickness or width. A major body of granite cannot occur. The low metamorphic grade of the greenstone rocks of the dome is also consistent with there being only a small volume of granite. The upper crustal rocks under the North Pole Dome must be of about greenstone belt mean density, and older than the Warawoona Group.

Summary. The larger magnetic anomalies are probably due to banded iron formation within the greenstone belt, that have enhanced magnetisation below 1-2 km. The anomalies show that the banded iron formation, and the surrounding greenstone belts extend down near vertically, with similar width, to approximately the base of the upper crust (Fig. 5).

Regional variation of crustal properties across the Pilbara Craton

This section discusses the evidence for regional changes across the Pilbara Craton in geophysical crustal properties. The boundary of the Pilbara Craton is taken as the discontinuity in mean gravity value and gravity trend (Wellman 1978)(Fig. 32c black line).

Regional changes in mean crustal density are reflected in the free air gravity anomaly (Fig. 32c), or the isostatic gravity anomaly (Fig. 5 of Wellman 1979). These show the lowest anomalies near the centre of the craton (the Yule Granitoid Complex), low values forming a northwest trending band crossing the centre of the craton, and relatively high values occurring over the northeast third of the craton. These regional changes in free air anomaly are thought to reflect regional changes in average upper crustal density.

Regional changes in mean crustal susceptibility should be reflected in long-wavelength component of the total magnetic intensity map (Fig. 32a). To show the long-wavelength anomalies clearly the total magnetic anomalies have been upward continued 50 km. The resultant map (Fig. 32b) shows high magnetic anomaly values over the western or southwestern half of the craton, and mid-range anomaly values over the eastern or northeastern half of the craton. These average anomaly values are part of a gentle gradient decreasing to the east, but because the gradient has a high to low distance of 600 km, and the shortest wavelength of the anomalies is about 200 km, the average anomaly value in the eastern Pilbara Craton correctly reflects the underlying mean crustal susceptibility. The regional changes in magnetic anomaly are thought to be caused mainly by changes in mean susceptibility of the upper crust, because elsewhere in Australia both short and long wavelength magnetic anomalies change abruptly at boundaries between different crustal blocks.

The western and eastern parts of North Pilbara have a different pre-Hamersley Basin geological history, so to find a difference in their crustal properties is not be surprising. However, one would expect the boundary to trend north, or northeast along the westernmost of the major shears of Figure 19, not to trend northwest.

Data on the seismic velocities of the upper and lower crust as determined by Drummond (1983) are summarised in Table 4 and Figure 4. The iron ore explosions used were at Goldsworthy, Sunrise Hill and Shay Gap in the northwest part of the craton within the pre-Hamersley Basin sequence, and at Pannawonica, Tom Price, Paraburdoo and Newman on thick Hamersley Basin sediments near the eastern and southern margins of the craton. From these data, Drummond (1983) concluded that the variation in crustal velocities and crustal thicknesses were all caused by the southward dip of the crust mantle boundary across the Pilbara Craton. This increase in crustal thickness southwards is consistent with the increased crustal loading by topography to the south, the mean altitude of the land surface being near sea level in the north part of the Pilbara Craton, and about 500 m on the southern margin of the Pilbara Craton. Relative to average continental crust, the crust of the Pilbara Craton is thin, with a relatively-low average-velocity and density.

Table 4. Seismic refraction results Pilbara Craton (from Drummond 1983).

The thicknesses given are to the top of the velocity change. The end points of the profiles are: Shay Gap (S), Goldsworthy (G), Newman (N), Tom Price (T), Paraburdoo (P) and Panawonica (W).

profile	upper crust mean velocity ($km.s^{-1}$)	base upper crust (km)	lower crust mean velocity ($km.s^{-1}$)	base lower crust (km)
northern Pilbara Craton, shot on Pilbara Craton rocks				
S-N	6.05	12	6.42	28
G-N	6.08	13	6.55	26
G-T	6.16	12	6.52	25
mean	6.1	12	6.5	26
southern Pilbara Craton, shot on Hamersley Basin rocks				
W-T	6.16	14	6.53	31
T-G	6.17	11.5	6.55	29
P-G	6.25	14	6.6	32
N-T	6.15	16	6.61	28
N-W	6.16	14	6.53	31
N-G	6.15	13	6.8	35
mean	6.2	14	6.6	31

The above data show that the main regional changes across the Pilbara Craton, are a southern increase in topographic loading and crustal thickness, and a difference between the northeastern third of the Pilbara Craton and the rest, with the upper crust of the northeastern third having a higher density and lower apparent susceptibility.

Conclusions

1. The gravity anomalies mainly reflect the density contrast between the granitoid complexes and greenstone belts. The mapped contact between the granitoid complex and greenstone belt is very irregular at the surface, and it is likely to be equally irregular at depth. The line of greatest gradient is generally a smooth curve following the average position of the mapped contact. This is consistent with the mean position of the contact generally following this line of greatest gravity gradient, and near vertical. The inferred shape of the granitoid complexes, a cylinder with a vertical axis, is consistent with both the diapir and asymmetric extension models for granitoid complex formation. The main constraint from the geophysics

is the granitoid complex margins are near vertical, and there is a break in composition from the lower to upper crust.

2. The seismic model of Drummond (1983) for the Pilbara crust is for a two layer model, with a gradual velocity increases with depth in the upper and lower crust, and a short, steeper downward increase at mid crust. The amplitude of the gravity lows over the granitoid complexes is consistent with about 2/3 of the granitoid complexes having a similar mid-crustal depth, with the remainder generally 80-50% shallower. The simplest model consistent with the seismic, gravity and magnetic data is to have change of density and seismic velocity mainly at one horizon - for the granitoid complexes and greenstone belts to extend to the base of the upper crust. The upper crust is about 50% granite and 50% greenstone-belt. The seismic model of Drummond implies that near the mid-crustal boundary the average lower crust is more mafic than the average upper crust.

3. Wide, high-amplitude magnetic anomalies occur over the greenstone belts. They are thought to be due to banded iron formation having enhanced magnetisation below a depth of 1-2 km. The anomaly shape is consistent with the banded iron formation, and hence the enclosing greenstone-belt, extending, approximately vertically, to a depth of about 14 km.

4. Long wavelength gravity and magnetic anomalies indicate major variation in upper crustal properties. They indicate that the northeastern third of the Pilbara Craton has relatively higher average density and lower apparent susceptibility. The gravity anomaly difference between values over granite versus values over greenstone belt differs across the Pilbara Craton. In the west, the gravity difference is less, probably because the greenstone belts contain more sediments and less mafic lava.

5. Major shear zones have been geologically mapped in the western Pilbara Craton. Across the shear zones are major changes in surface geology and significant shear movement. The extent of these shear zones was mapped using gravity and magnetic anomalies They extend right across the Pilbara Craton. The shear zones are marked by elongate, narrow magnetic highs, the truncation of long-wavelength magnetic anomalies, and by gravity gradients. They occur only in the northwest half of the Pilbara Craton.

6. The magnetic images have been used to map the extent of magnetised dykes over the Pilbara Craton. As these dykes have significant magnetisation, they are thought to be post metamorphic. The dykes were intruded sub-vertically, and they have not been significantly tilted. Hence the reduced-to-the-pole magnetic anomaly images give an anomaly shape that is indicative of the remanent magnetisation of the dykes. A map of the dyke distribution, coloured to show magnetisation, allows a better subdivision into dyke swarms, as each swarm should have a similar location, strike, spacing, polarity and magnetic amplitude.

7. Tests were carried out into the best method of displaying gamma-ray spectrometric data in areas of solid rock outcrop. The traditional red/green/blue for K/Th/U images will continue to be the best display in one image, and preparation is relatively fast. However this image, and other traditional display methods, does not extract the maximum amount of information out of the spectrometric data, and expressing it quantitatively. The major rock types can be treated separately because their fields had minimal overlap on the K-Th plane. For major rock types there is a correlation between K and Th. The best display of the K, Th and U data is thought to be three maps of components for each major rock type, the three components being the amount of geochemical variation, anomalous thorium, and anomalous uranium. Display of principal components is thought to be less useful, as the proportional errors in the elements differ greatly, and the resultant principal components are more difficult to interpret in terms of geology.

8. Interpretation of the gamma-ray spectrometric data over granites is important because of the difficulty of subdividing granites using air-photographs, or Landsat TM data. Previous geological studies subdivided the granites into three types - older, porphyritic and younger. Using the geologically mapped extent of these granite types it can be shown that they occupy different fields in K-Th-U space, and the porphyritic granites can be subdivided into two kinds. Hence in K-Th-U space there appear to be four types of granites, each with a separate composition field, and each with a very different geochemical variation path.

Acknowledgments

I am very grateful for discussions with NGMA personnel both of AGSO and the Geological Survey of Western Australia. Particular thanks are due to Richard Blewett for long discussions on this work. Considerable help with the computing was received from Mitch Ratajkoski, and the AGSO Airborne Group. I am grateful for reviews of this record by Richard Blewett, George Gibson and Alan Whitaker. Brian Minty provided information on measurement errors in spectrometric surveys. The work was carried out under the North Pilbara Project of the NGMA.

References

Clark, D.A., 1997. Magnetic petrophysics and magnetic petrology: aids to geological interpretation of magnetic surveys. AGSO Journal of Australian Geology & Geophysics, 17 (2), 83-103.

Clark, D.A. & Emerson, D.W., 1991. Notes on rock magnetisation characteristics in applied geophysical studies. Exploration Geophysics, 22, 547-555.

Clark, D.A. & Schmidt, P.W., 1994. Magnetic properties and magnetic signatures of BIFs of the Hamersley Basin and Yilgarn Block, Western Australia. In, Dentith, M.E., Frankombe, K.F., Ho, S.E., Shepherd, J.M., Groves, D.I. & Trench, A. (editors), Geophysical signatures of the Western Australian mineral deposits. Geology and Geophysics Department (Key Centre) & UWA Extension, The University of Western Australia, Publication No. 26, 343-354.

Drummond, B.J., 1983. Detailed seismic velocity/depth models of the upper lithosphere on the Pilbara Craton, northwest Australia. BMR Journal of Australian Geology and Geophysics, 8, 35-51.

Dickson, B.L. & Scott, K.M., 1997, Interpretation of aerial gamma-ray surveys - adding the geochemical factors. AGSO Journal of Australian Geology and Geophysics, 17, 187-200.

Glikson, A.Y. & Hickman A.H., 1981. Geochemistry of Archaean volcanic successions, eastern Pilbara Block, Western Australia. Bureau of mineral Resources, Australia, Record 1981/36.

Glikson, A.Y., Davy, R. & Hickman, A.H., 1986. Geochemical data files of Arcaean volcanic rocks, Pilbara Block, Western Australia. Bureau of mineral Resources, Australia, Record 1986/14.

Hickman, A.H., 1983. The geology of the Pilbara block and its environs. Western Australian Geological Survey Bulletin 127, 268 pp.

Hickman, A.H. & Lipple, S.L., 1978. Marble Bar, W.A. Western Australian Geological Survey 1:250 000 Geological Series Explanatory Notes, 24 pp.

Kerr, T.L., O'Sullivan, A.P., Podmore, D.C., Turner, R. & Waters, P., 1994. Geophysics and ore exploration: examples from the Jimblebar and Shay Gap-Yarrie Regions, Western Australia. In, Dentith, M.E., Frankombe, K.F., Ho, S.E., Shepherd, J.M., Groves, D.I. & Trench, A. (editors), Geophysical signatures of the Western Australian mineral deposits. Geology and Geophysics Department (Key Centre) & UWA Extension, The University of Western Australia, Publication No. 26, 355-367.

Krapez, B., Eisenlohr, B., 1998. Tectonic settings of Archean (3325-2775 Ma) crustal-supracrustal belts in the West Pilbara Block. Precambrain Research, 88, 173-205.

Milligan, P.R. & Gunn, P.J., 1997. Enhancement and presentation of airborne geophysical data. AGSO Journal of Australian Geology and Geophysics, 17 (2), 63-75.

Richardson, L.M., 1997. Marble Bar (Marble Bar, western Port Hedland, eastern Roebourne and northeastern Pyramid 1:250 000 sheet areas) airborne geophysical survey 1996 – operations report. Australian Geological Survey Organisation, Record 1997/63.

Smithies, R.H., 1996. Sherlock, W.A., Sheet 2456 (prelim ed.): Western Australian Geological Survey, 1:100 000 Geological Series.

Vacquier, V., Steenland, N.C., Henderson, R.G., Zietz, I., 1951. Interpretation of aeromagnetic maps. The Geological Society of America Memoir 47, 151pp.

Wellman, P., 1978. Gravity evidence for abrupt changes in mean crustal density at the junction of Australian crustal blocks. BMR Journal of Australian Geology and Geophysics, 3, 153-162.

Wellman, P., 1979. On the isostatic compensation of Australian topography. BMR Journal of Australian Geology and Geophysics, 4, 373-382.

Wingate, M., Powell, C. McA., Li, Z.X., Bird, R., 1988. Palaeomagnetic and geochronological constraints on the Neoproterozoic break-up of the eastern margin of Rodinia. Geological Society of Australia, Abstracts, 49, 472.

Zuber, M.T., Bechtel, T.D., and Forsyth, D.W., 1989. Effective elastic thickness of the lithosphere and mechanism of isostatic compensation in Australia. Journal of Geophysical Research, 94, 9353-9367.

Appendix 1. Equations in K, Th and U defining for major rock types their fields in K-Th-U space, and their components

In the following equations K is expressed in percent, and Th and U expressed in ppm.

Mafic igneous rocks
Field in K-Th-U space: $K < 1.2$ and $Th < 5$
Components: $C1 = K + Th/5$: $\Delta Th = Th/5 - K$: $\Delta U = U - Th/3$

Sediments and intermediate igneous rocks
Field in K-Th-U space: $(K > 0.4)$ and $(K < 2.8)$ and $(Th > 4)$ and $(Th/K > 5.71)$ and $(K - Th/12 < 1)$ and $(Th > 5)$.
Components: $C1 = K + Th/5$: $\Delta Th = Th/5 - K$: $\Delta U = U - Th/2.3$

Felsic igneous rocks
Field in K-Th-U space: if $((K > 1.8)$ and $(K < 2.8)$ and $((K - Th/12) > 1))$ or $((K < 1.8)$ and $(Th/K < 5.7))$ or $(K > 2.8)$
Component $C1 = K + Th/20 + U/5$
Residual K: if $(U < 3)$ then null, else $(K - (K + Th/20 + U/5) * 0.115 - 2.8)$
Residual Th: if $(U > 3)$ then $(Th - (K + Th/20 + U/5) * 7.46 - 14.73)$ else $(K < 2.67)$ then $(Th - 3*K + 2.5)$ else $(Th + 21.2 - K * 11.76)$

Appendix 2. Distribution of susceptibilities for major rock types.

See histograms of figures 23-25.

Wellman data

	Rock type								
Log10Sus	felsic	mafic	ultramafic	dyke	gabbro	granite	gneiss	sediment	all greenstone
-0.9					0				2
-1.1	0	1	2	1	0	0	0	0	4
-1.3	1	7	2	1	14	0	0	2	12
-1.5	0	5	1	1	8	0	0	0	8
-1.7	0	2	1	0	0	0	0	1	11
-1.9	1	2	1	3	3	0	0	1	10
-2.1	0	4	1	0	0	1	0	0	7
-2.3	0	3	0	0	2	0	3	1	7
-2.5	1	5	0	0	1	2	0	0	11
-2.7	0	4	0	0	0	1	2	1	9
-2.9	0	7	2	0	1	1	0	4	15
-3.1	1	23	3	2	1	1	4	7	53
-3.3	18	74	7	2	2	3	5	6	146
-3.5	5	14	1	0	5	4	4	15	56
-3.7	10	3	1	0	0	5	5	18	47
-3.9	5	0	0	0	0	5	1	6	17
-4.1	3	0	0	0	0	5	1	10	21
-4.3	3	0	0	0	0	7	0	6	16
-4.5	1	0	0	0	0	1	0	6	8
-4.7	2	0	0	0	0	2	2	10	17
-4.9	0	0	0	0	0	1	0	2	3
-5.1	0	0	0	0	0	0	0	5	6
total sites	51	154	22	10	37	39	27	101	486

Mapping data

	Rock type								
Log10Sus	felsic	mafic	ultra	dyke	gabbro	granite	gneiss	sed	all data
-0.1	0	0	0	0	0	0	0	0	0
-0.3	0	0	0	0	0	0	0	1	1
-0.5	0	0	0	0	0	0	0	1	1
-0.7	0	1	1	0	0	0	0	4	6
-0.9	0	4	11	0	0	1	1	9	27
-1.1	0	2	13	0	2	1	1	9	28
-1.3	0	6	30	0	0	2	2	5	47
-1.5	0	4	37	0	2	18	9	7	78
-1.7	0	2	17	1	2	74	10	4	111
-1.9	1	9	18	0	2	155	8	8	201
-2.1	0	4	5	0	0	224	9	2	245
-2.3	1	3	10	0	2	263	12	7	300
-2.5	0	6	7	1	0	235	12	7	271
-2.7	1	7	5	0	1	188	11	1	216
-2.9	3	19	3	3	2	118	21	11	190
-3.1	0	64	4	6	19	114	34	26	299
-3.3	3	83	15	5	41	112	61	33	379
-3.5	3	17	7	1	6	167	31	32	290
-3.7	2	1	0	1	0	142	15	17	189
-3.9	4	1	0	0	0	265	34	34	350
-4.1	1	0	0	0	1	112	3	21	144
-4.3	1	0	0	0	1	98	12	39	159
-4.5	2	1	0	0	0	60	1	21	92
-4.7	0	0	0	0	0	0	0	0	0
-4.9	0	0	0	0	0	35	0	6	42
-5.1	1	0	0	0	1	151	3	9	166
total	23	234	183	18	82	2535	290	314	3832

Appendix 2. Distribution of susceptibilities for major rock types.

See histograms of figures 23-25.

All data expressed as sites

	Rock type								
Log10Sus	felsic	mafic	ultra	dyke	gabbro	granite	gneiss	sed	all
-0.1	0	0	0	0	0	0	0	0	0
-0.3	0	0	0	0	0	0	0	0	0
-0.5	0	0	0	0	0	0	0	0	0
-0.7	0	0	0	0	0	0	0	1	1
-0.9	0	1	2	0	0	0	0	2	7
-1.1	0	1	4	1	0	0	0	2	9
-1.3	1	8	7	1	14	0	0	3	34
-1.5	0	6	7	1	8	3	2	1	29
-1.7	0	2	4	0	0	12	2	2	30
-1.9	1	4	4	3	3	26	1	2	47
-2.1	0	5	2	0	0	38	2	0	48
-2.3	0	4	2	0	2	44	5	2	59
-2.5	1	6	1	0	1	41	2	1	57
-2.7	0	5	1	0	0	32	4	1	45
-2.9	1	10	3	1	1	21	4	6	48
-3.1	1	34	4	3	4	20	10	11	104
-3.3	19	88	10	3	9	22	15	12	211
-3.5	6	17	2	0	6	32	9	20	109
-3.7	10	3	1	0	0	29	8	21	79
-3.9	6	0	0	0	0	49	7	12	75
-4.1	3	0	0	0	0	24	2	14	45
-4.3	3	0	0	0	0	23	2	13	43
-4.5	1	0	0	0	0	11	0	10	23
-4.7	2	0	0	0	0	2	2	10	17
-4.9	0	0	0	0	0	7	0	3	10
-5.1	0	0	0	0	0	25	1	7	34
total sites	**55**	**193**	**53**	**13**	**51**	**462**	**75**	**153**	**1162**

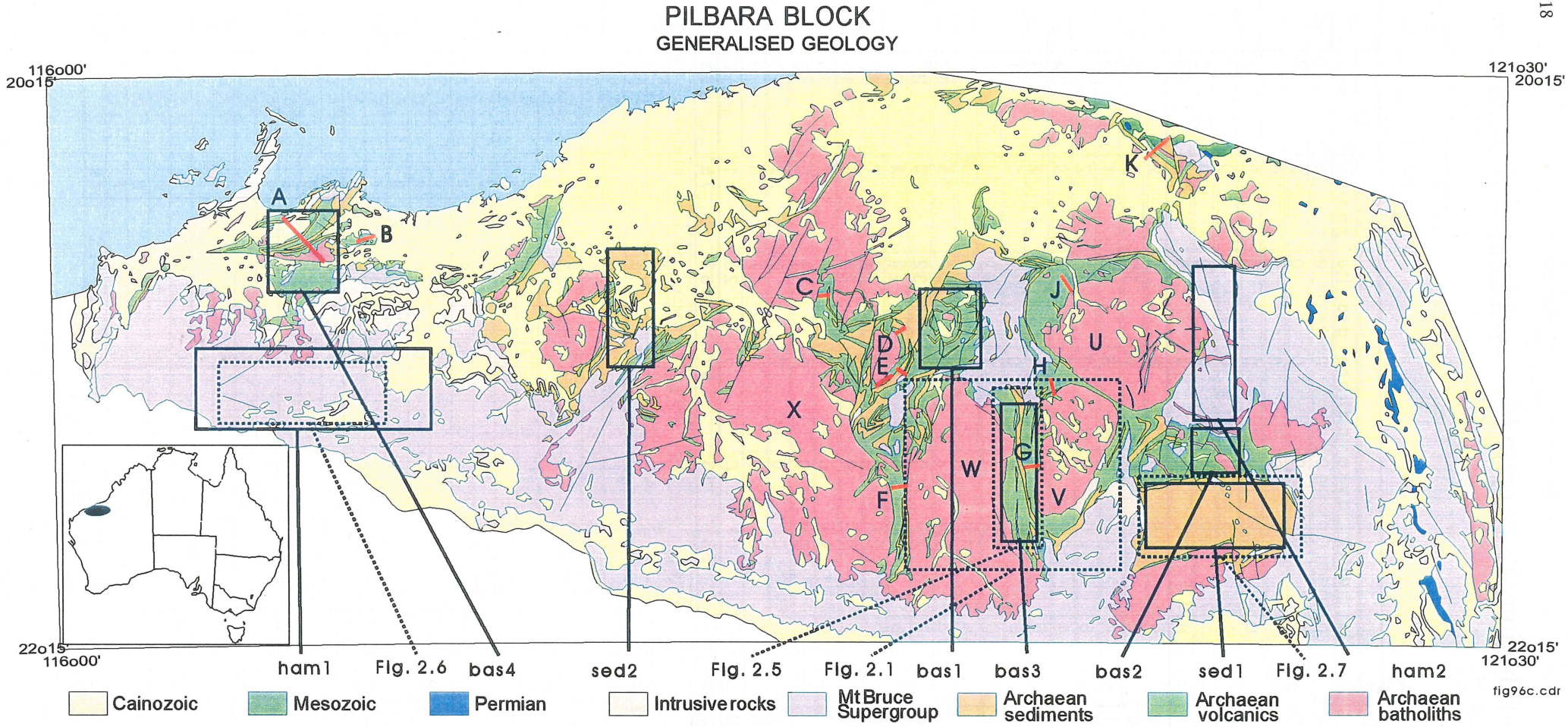

Figure 1. Map showing areas of scattergrams data of Figure 10, areas of component maps (Figs 9, 12, 13, 14), location of susceptibility traverses A-K, and the location of the granitoid complex studied in detail: U, Mount Edgar; V, Curruna Downs; W, Shaw; and X, Yule. The inset shows the location of the north Pilbara area.

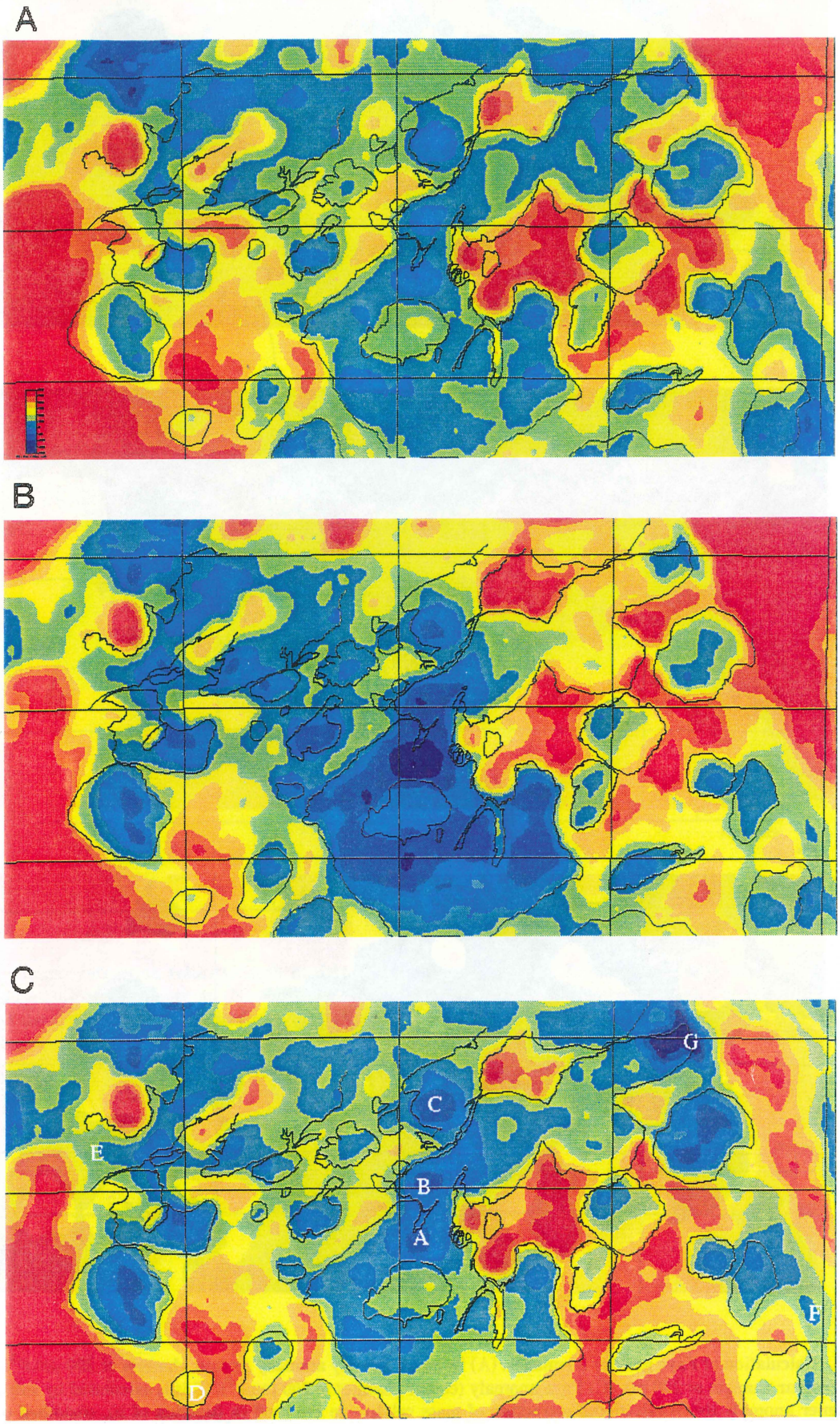

Figure 2. Comparison of residual gravity anomalies. (A) Residual formed by subtracting from the Bouguer anomaly a regional of wavelength 100 km fitted to the lowest values over granites. (B) Faye anomaly - a terrain corrected free air anomaly. (C) Faye anomaly minus 2nd order regional fitted to the lowest values over selected granites. Changes in colour are at 200 $\mu m.s^{-2}$ intervals. The black line is the outcrop and subcrop of the granite boundary. Letters A-E are referred to in the text.

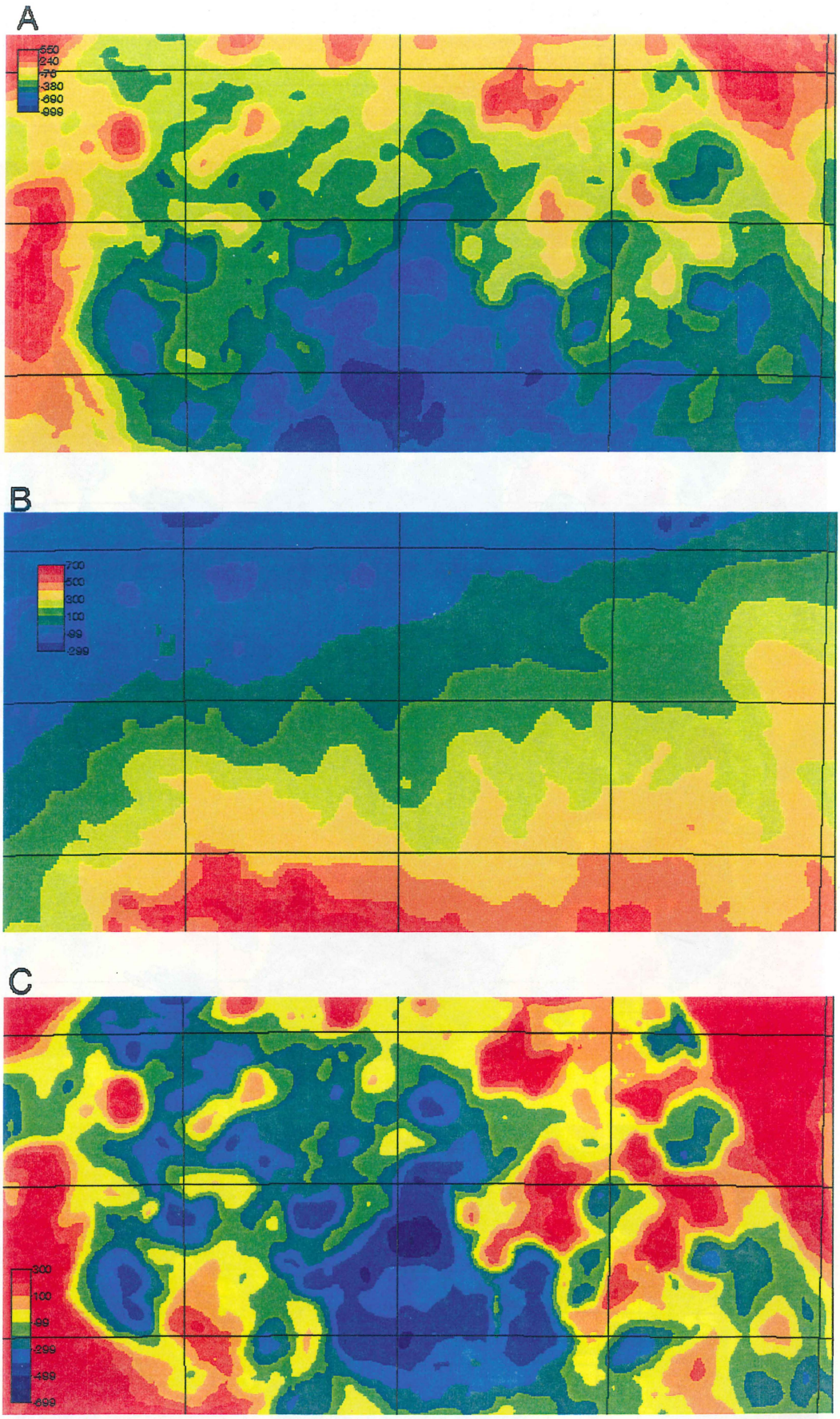

Figure 3. Calculation of Faye gravity anomalies. (A) Bouguer gravity anomaly (colour changes at 200 μm.s^{-2}). (B) Surface altitude (colour changes at 200 m). (C) Faye anomaly (colour changes at 200 μm.s^{-2}). This is calculated by subtracting from the Bouguer anomaly the gravitational attraction of mass relative to sea level (a function of b), smoothed over a 50 km area.

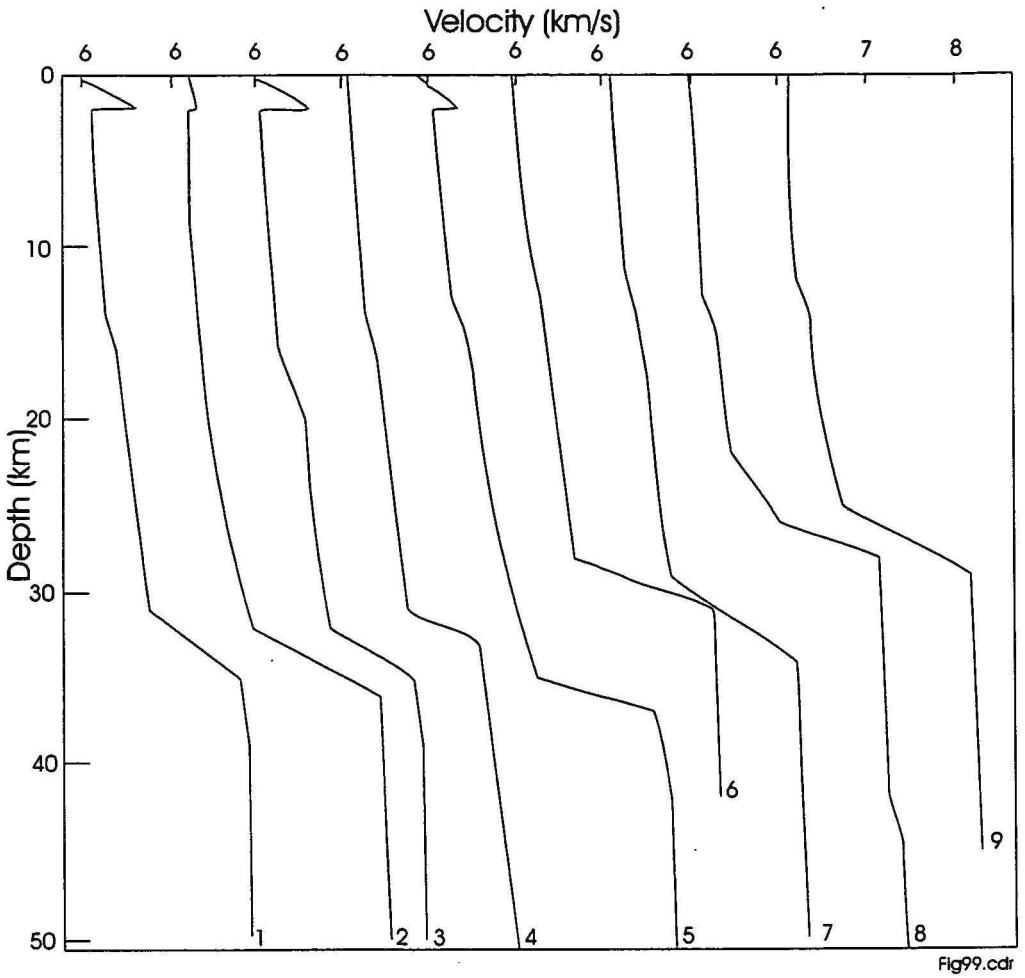

Figure 4. Seismic refraction velocity/depth models of the Pilbara Craton of Drummond (1983). Shot points are at Shay Gap (S), Goldsworthy (G), Newman (N), Tom Price (T), Paraburdoo (P) and Panawonica (W). The following list gives for each model the shot point and the diection of recording: 1 N→W, 2 P→G, 3 N→W, 4 W→N, 5 N→G, 6 S→N, 7 T→G, 8 G→N, 9G→T.

Seismic

At mid crust
velocity increase of 0.15 km/s
at average depth 14 km.

Lower crust more mafic
than average of upper crust;
where upper crust is about
1/2 granite and 1/2 greenstone

Gradual velocity increase
with depth due to increase
in pressure.

Gravity

Position of gravity anomaly inflexion
averages over granite/greenstone
contact - so granitoid complexes on
average have near vertical sides.

Gravity lows are of similar value
- so granitoid complexes
have a similar base depth.

The base of the granitoid complexes
are thought to be at the base of
the upper crust.

Magnetic

Magnetic model

Very magnetic body has:
width similar to greenstone belt,
so the average greenstone belt
does not thicken or thin downward:
depth to top of body is 1-2 km;
depth to base of body is ~ 14 km:
susceptibility 1-3 SI.

Geological model

Banded iron formations causing
the magnetic anomalies are
interpreted to be:
- a small proportion of
greenstone belts;
- scattered through
full width of belt;
- extend from the Earth's surface
to base of upper crust

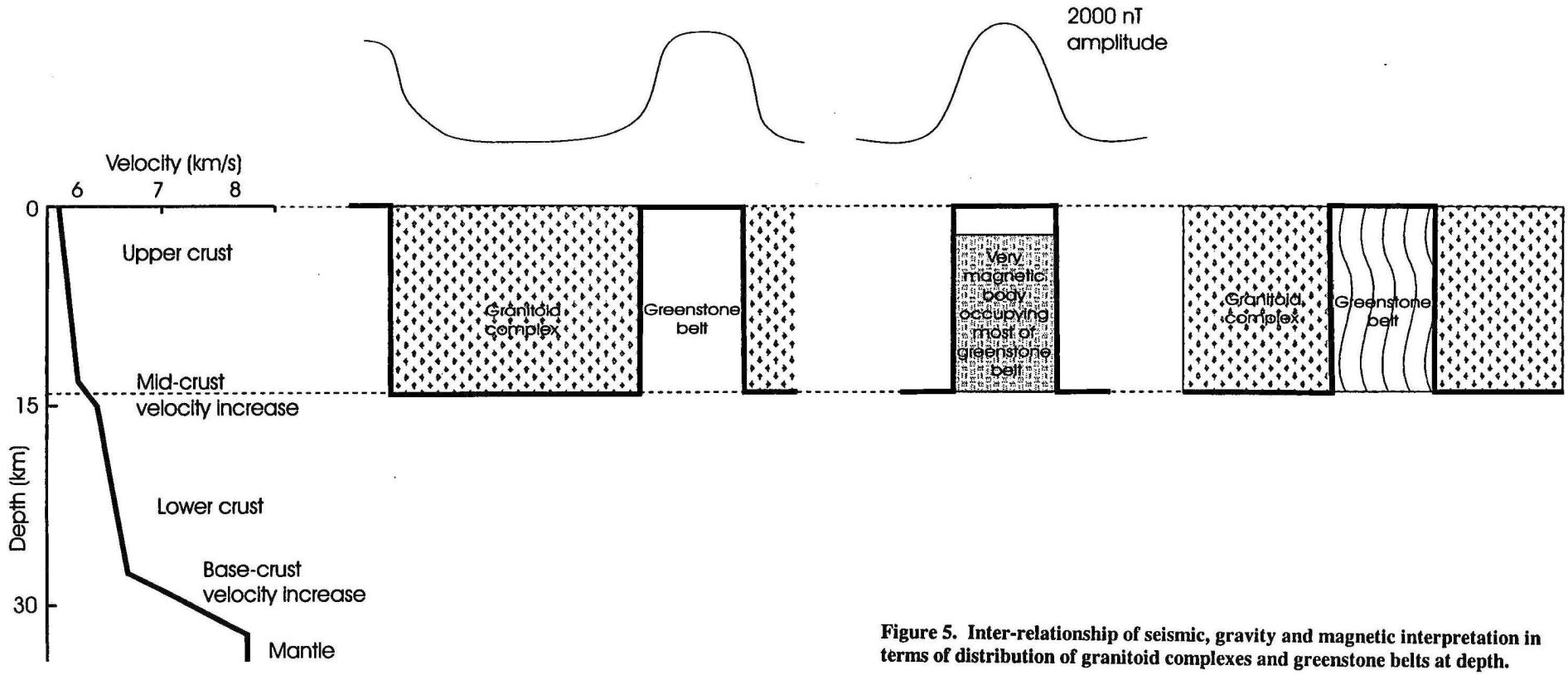

Figure 5. Inter-relationship of seismic, gravity and magnetic interpretation in terms of distribution of granitoid complexes and greenstone belts at depth.

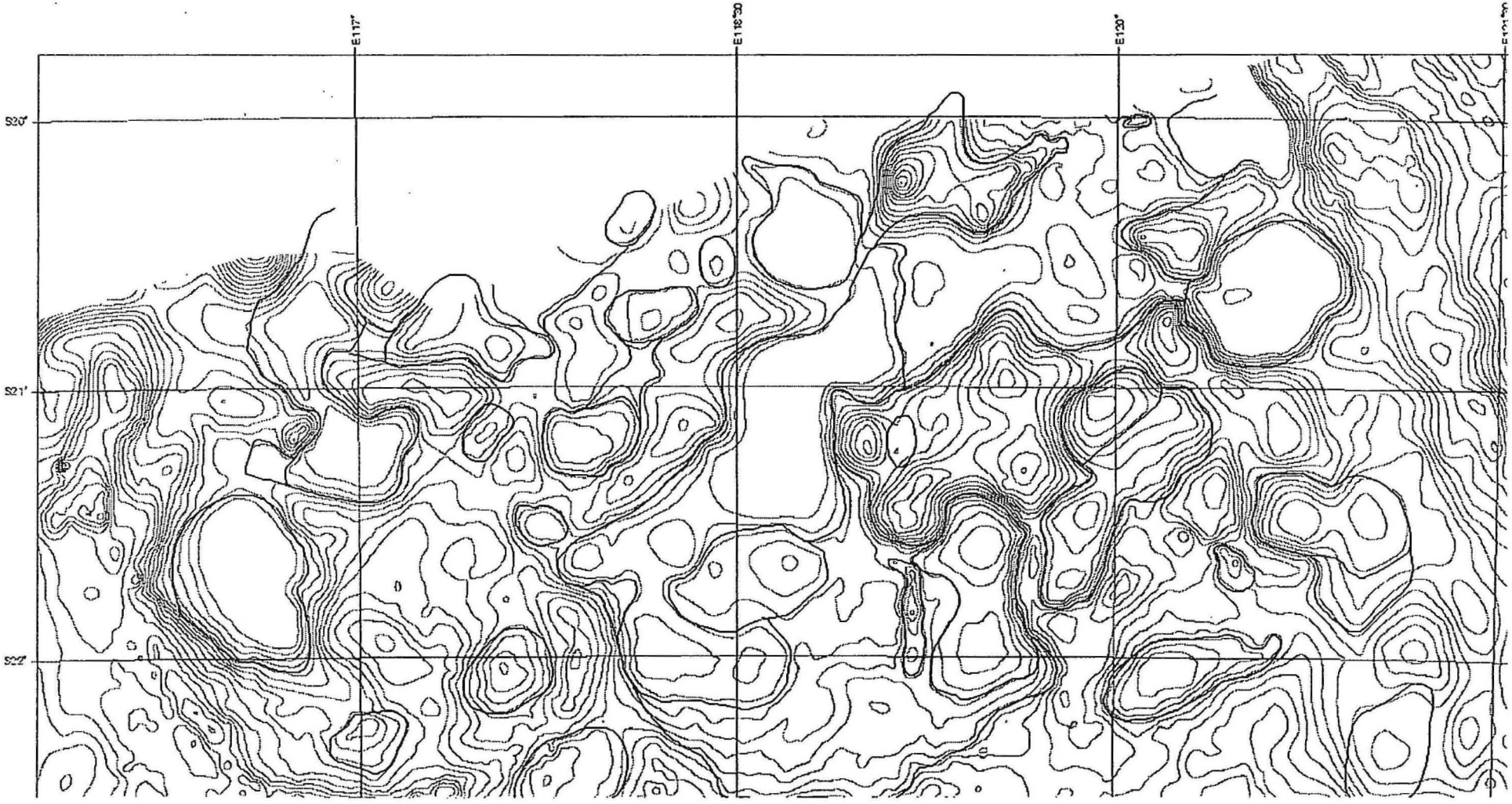

Figure 6. Location of the maximum gravity gradient. Contours of residual gravity anomaly are shown as grey contours (interval = 50 μm.s^{-2}). Lines of maximum gravity gradient shown as black lines.

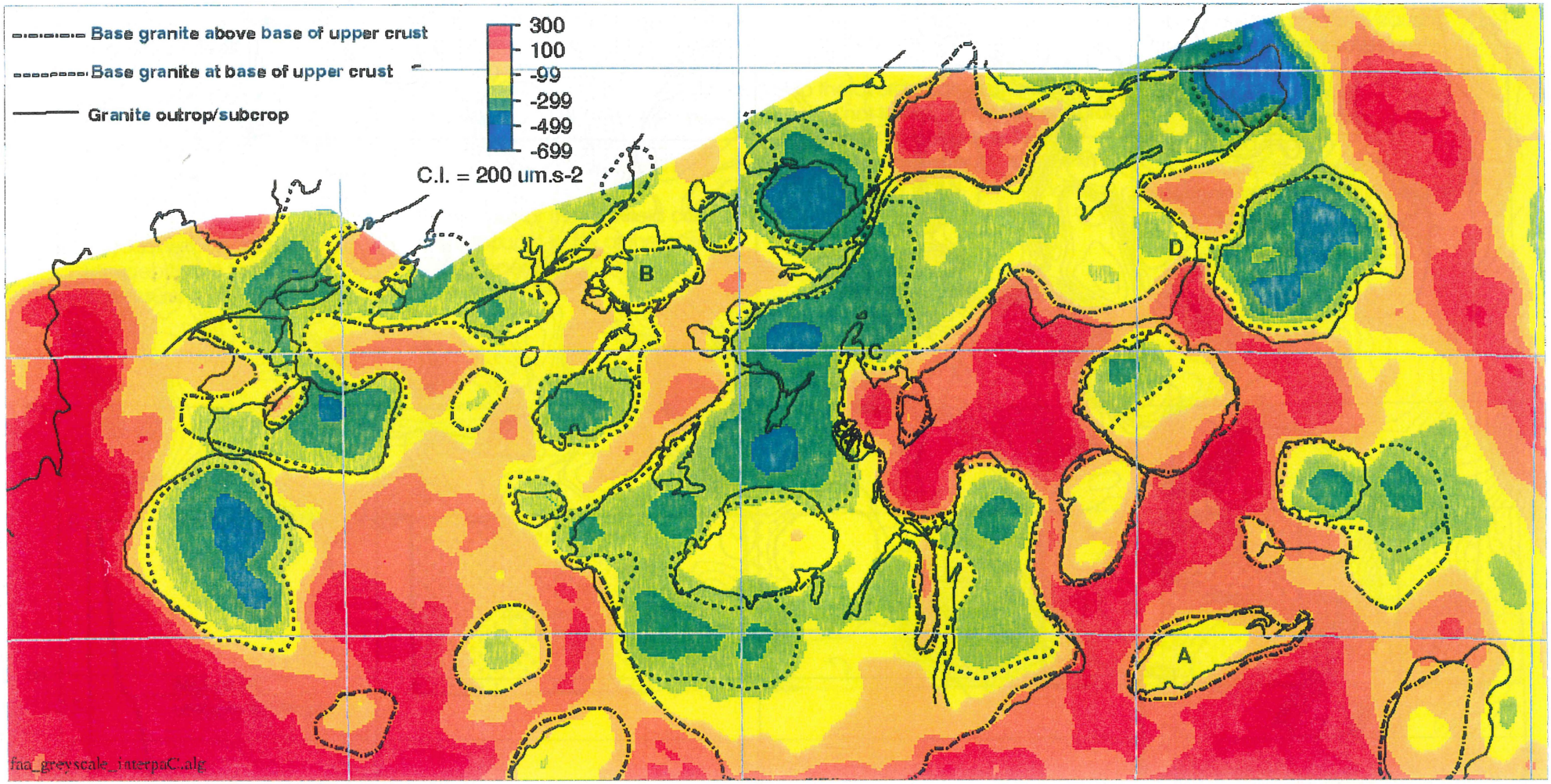

Figure 7. Relation between the granite margin's outcrop/subcrop and the margins average position at depth derived from the maximum gravity gradient. Colours give gravity residual anomaly (Figure 2c), with colour changes at 200 $\mu m.s^{-2}$.

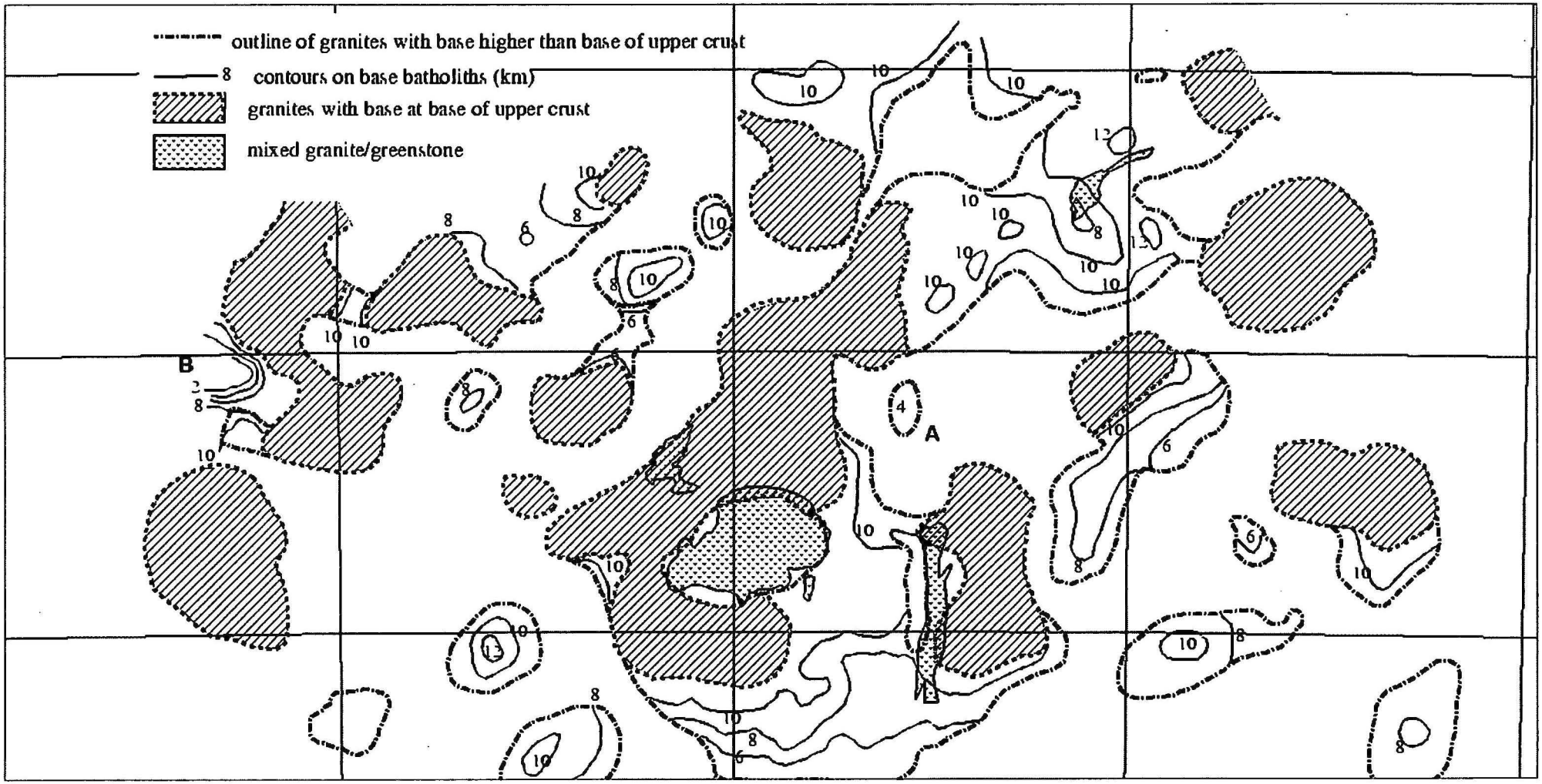

Figure 8. Thickness of granites. This shows the distribution of granites extending down to the base of the upper crust, and the distribution and depth to the base of shallower granites. Exceptionally thin granites are labelled A, B.

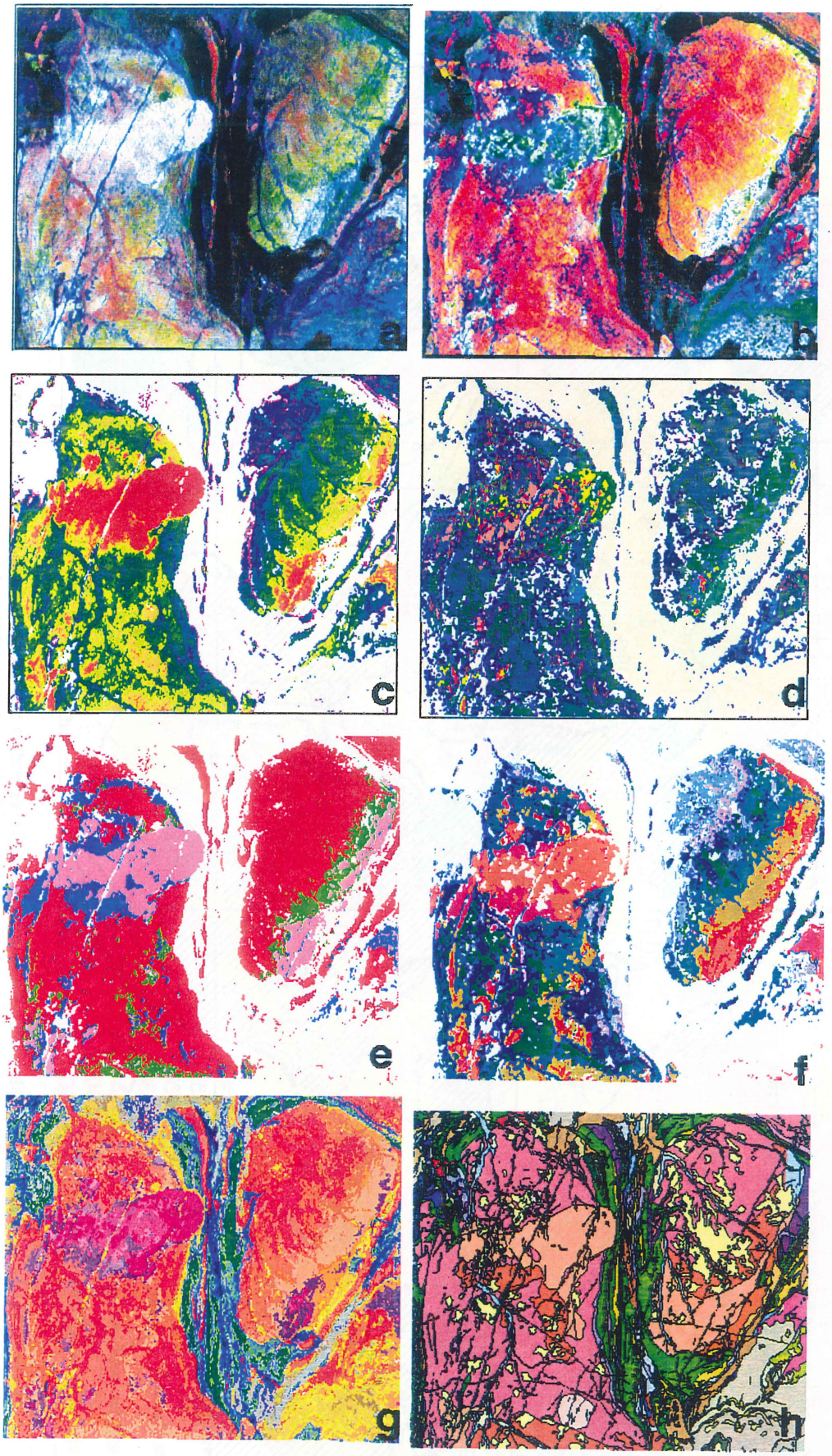

Figure 9. Comparison of display methods of spectrometric data for an area of granites in the north Pilbara region of Australia. Between the granites are bands of sediment and mafic volcanic rock. Width of area 84 km. (a) Red-green-blue colour-space composite image of K, Th, U. (b) Hue saturation-intensity image, with the saturation and intensity effects of Figure 9a decreased. (c) Distance along average geochemical variation path. DD = K(%) + Th (ppm)/20 + U (ppm)/5. (d) Direction of deviation from the average geochemical variation path. Composite red-green-blue: K-Th-U image. Positive differences of more than one standard deviation in full hue, and negative differences of more than one standard deviation 50% hue, 50% black. (e) Distribution of four different granite types (see text), each with a different geochemical variation path. (f) Map showing the distribution of supervised classification classes. (g) Geochemical map showing the distribution of classes, each with a different composition defined using K and Th. The legend given in Figure 35. (h) Geological map of the area (after Hickman & Lipple 1978).

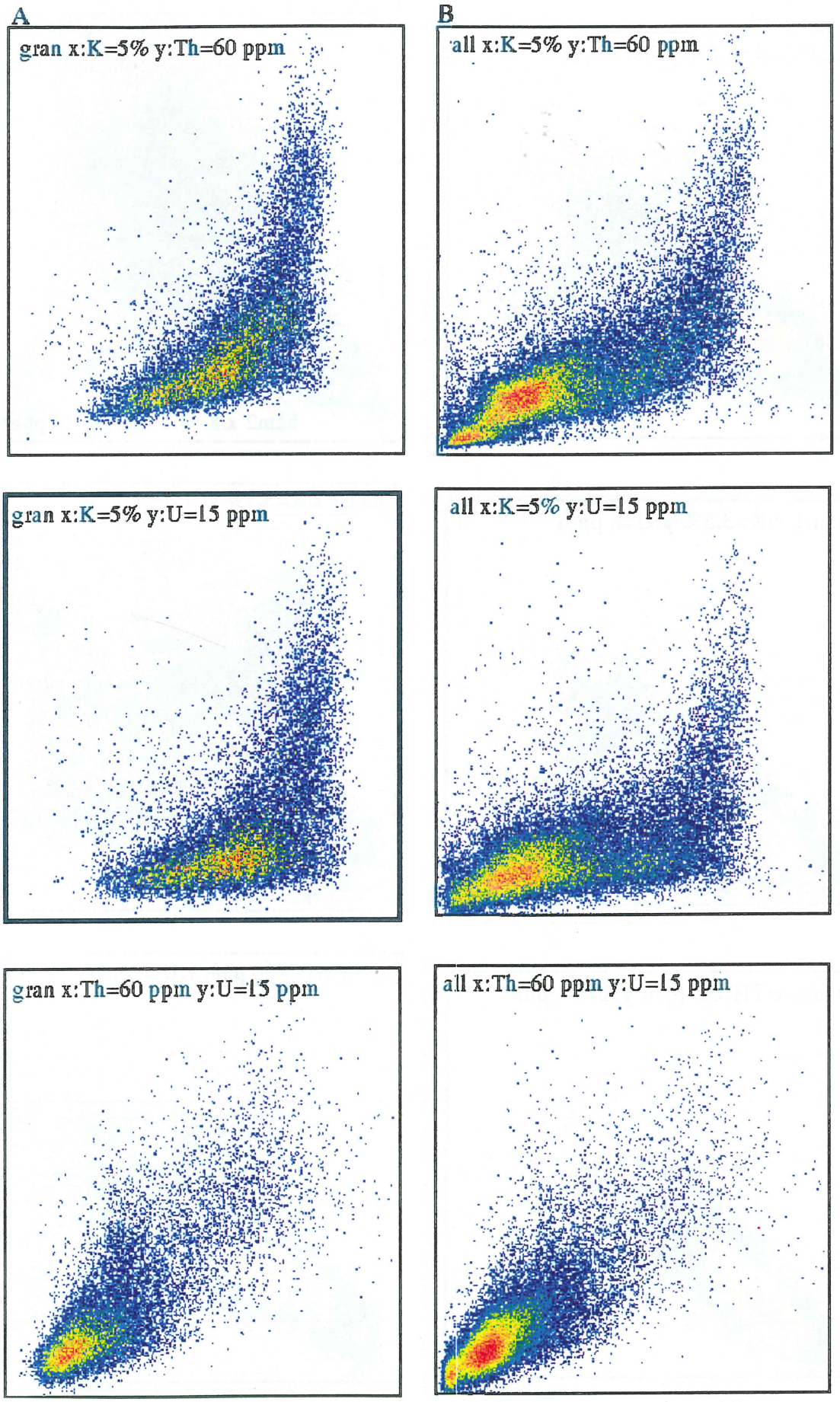

Figure 10a, b. Scattergram for felsic igneous rocks (Yule, Shaw, Corunna Downs and Mount Edgar Granitoid Complexes), and all rock types (for location of areas see Fig. 1). All scattergrams have zero concentrations in the lower left corner. The maximum concentrations on the other axes is written on the scattergram.

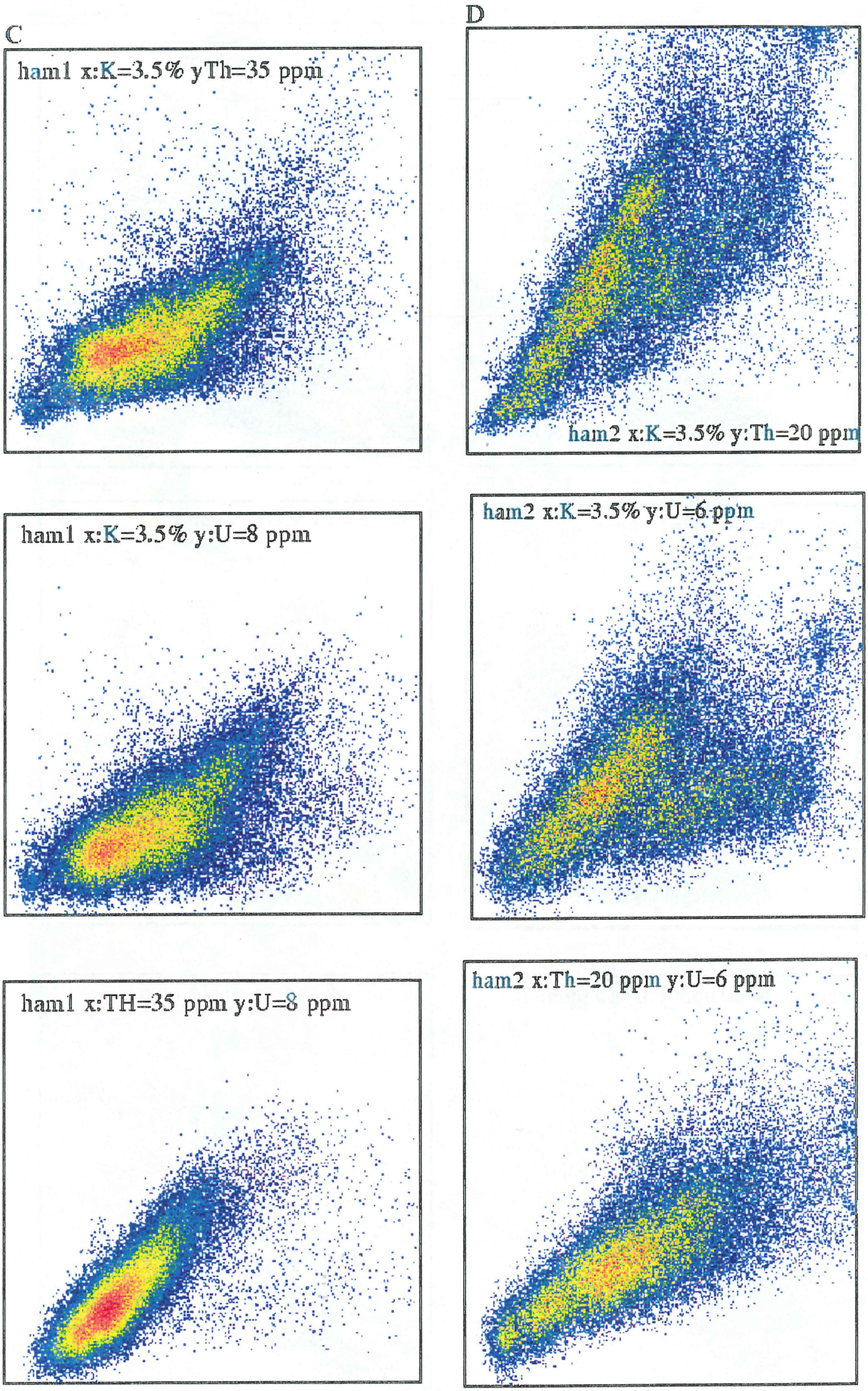

Figure 10c, d. Scattergram for two areas of mainly intermediate igneous rocks of the Fortescue Group (for location of areas see Fig. 1).

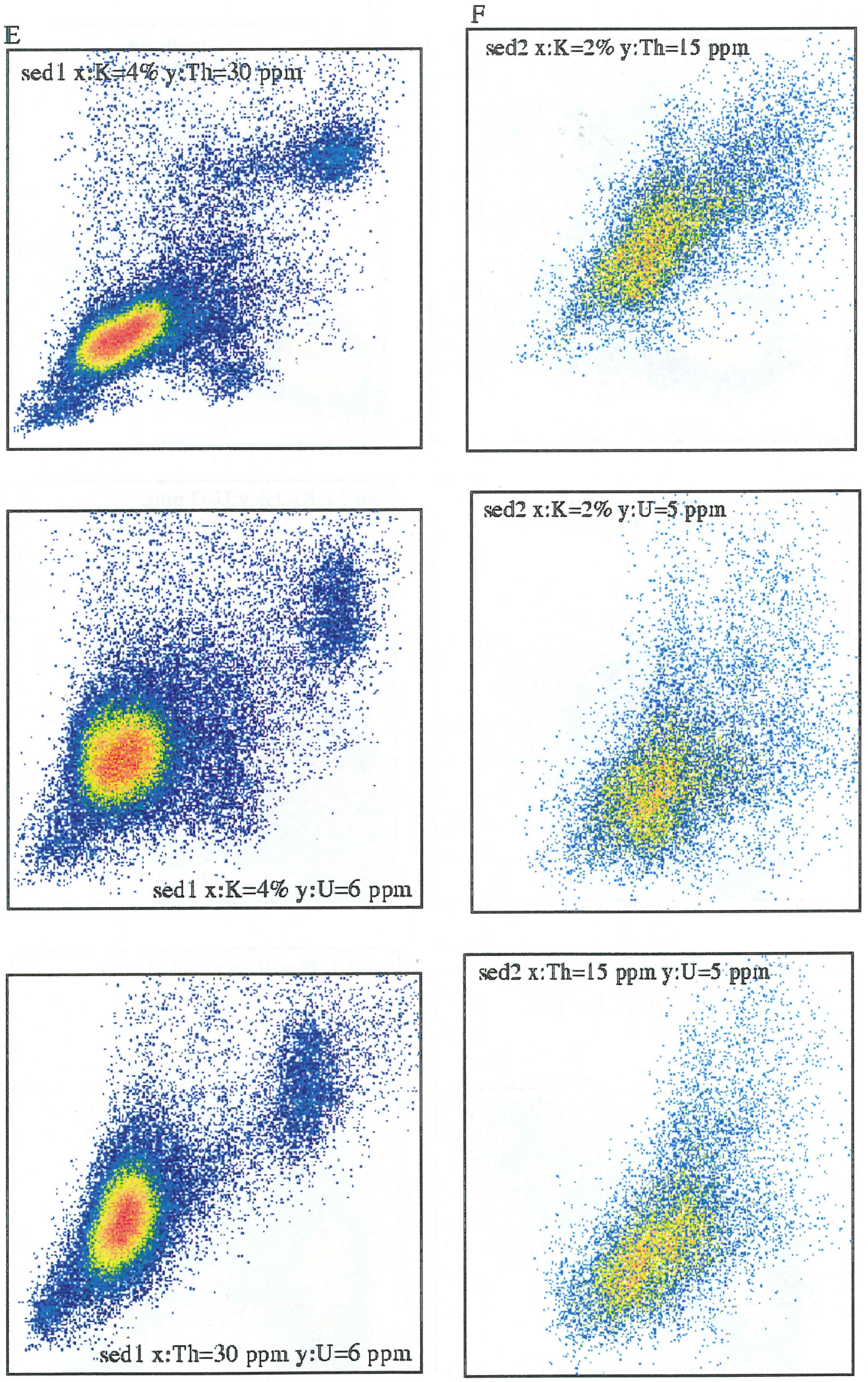

Figure 10e, f. Scattergram for two areas of Pilbara sedimentary rocks - Mosquito Creek Synclinorium, and Mallina Synclinorium (for location of areas see Fig. 1).

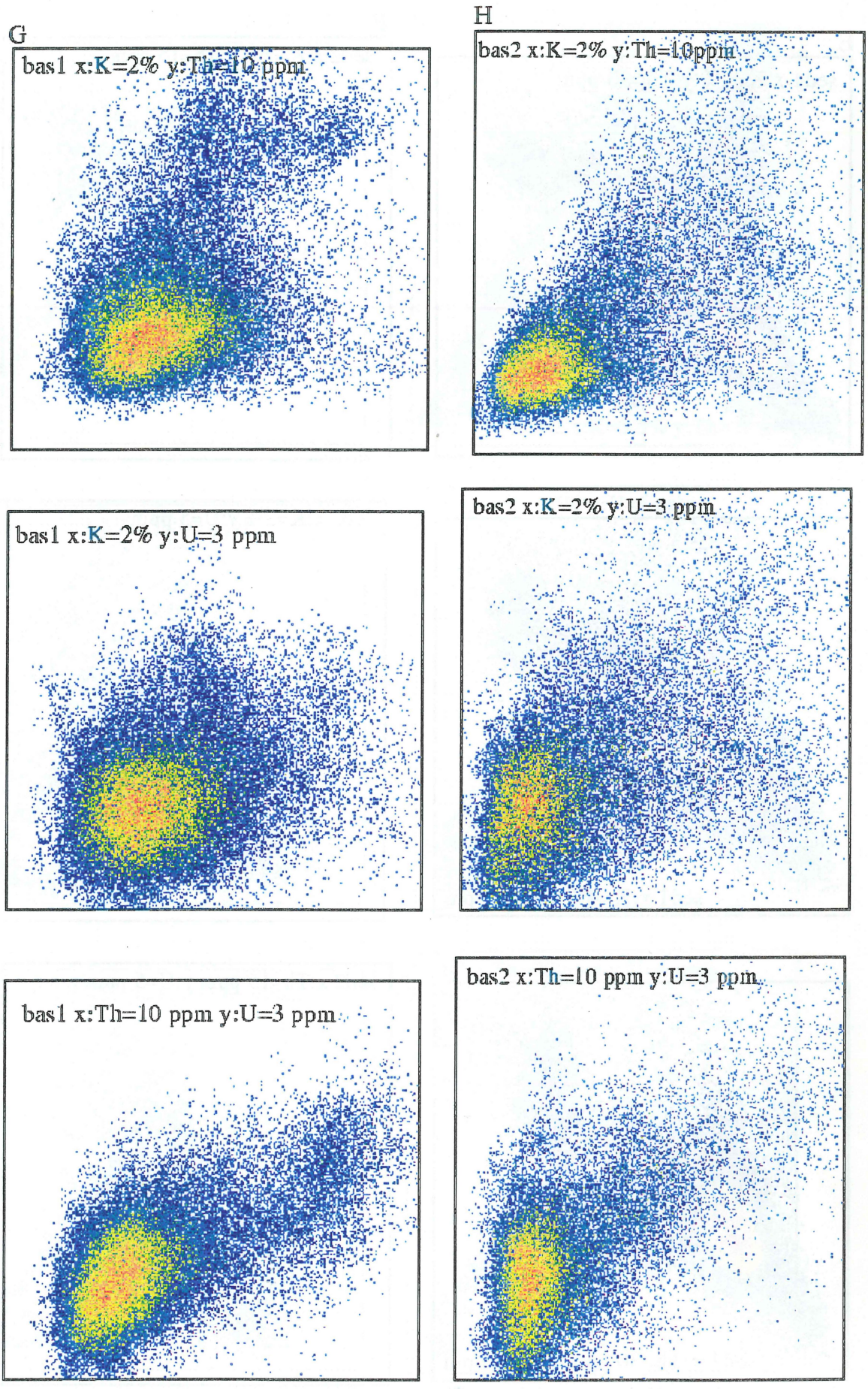

Figure 10g, h. Scattergram for two areas of the mafic volcanics (for location of areas see Fig. 1).

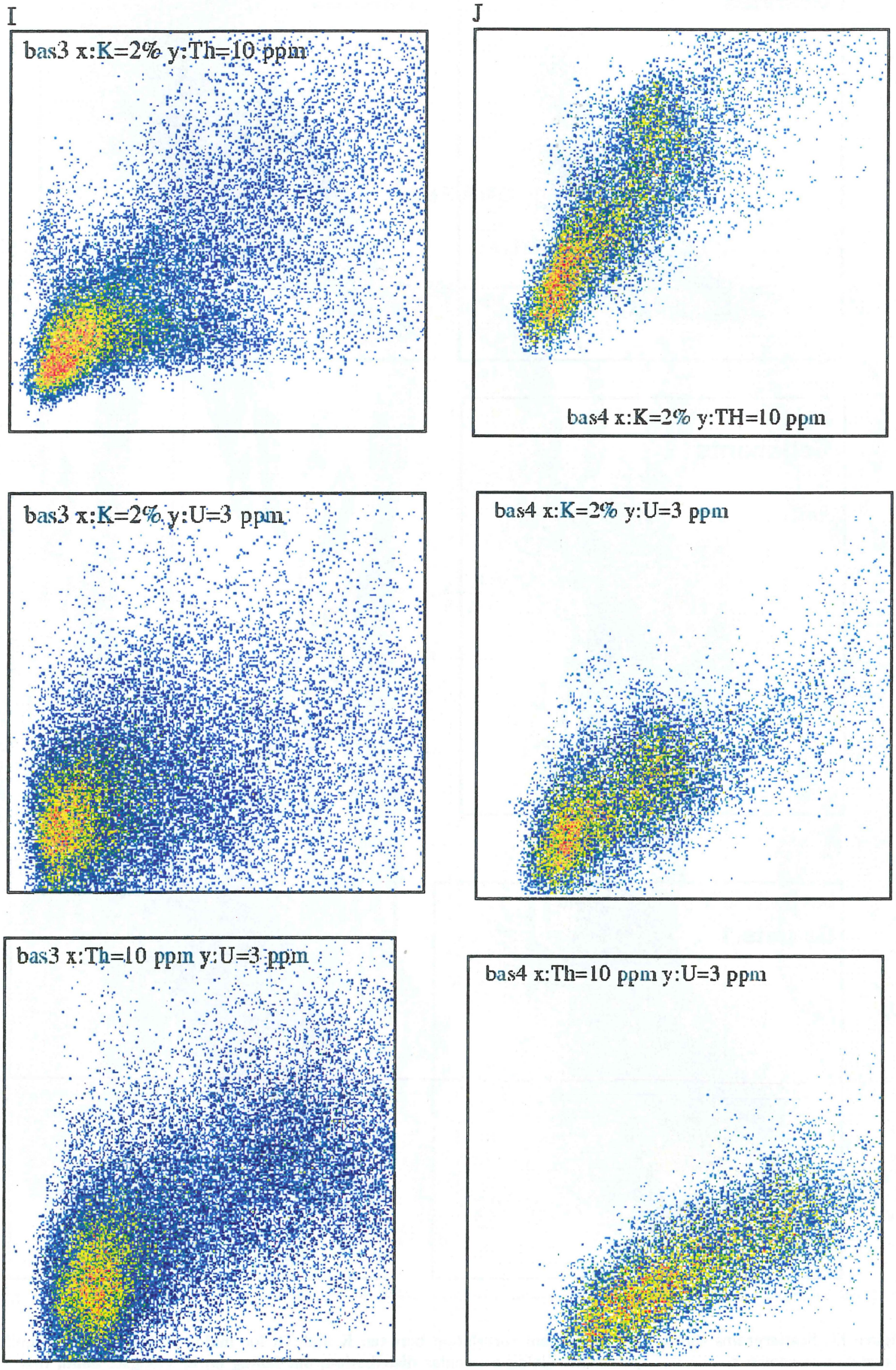

Figure 10i, j. Scattergram for two more areas of the mafic volcanics (for location of areas see Fig. 1).

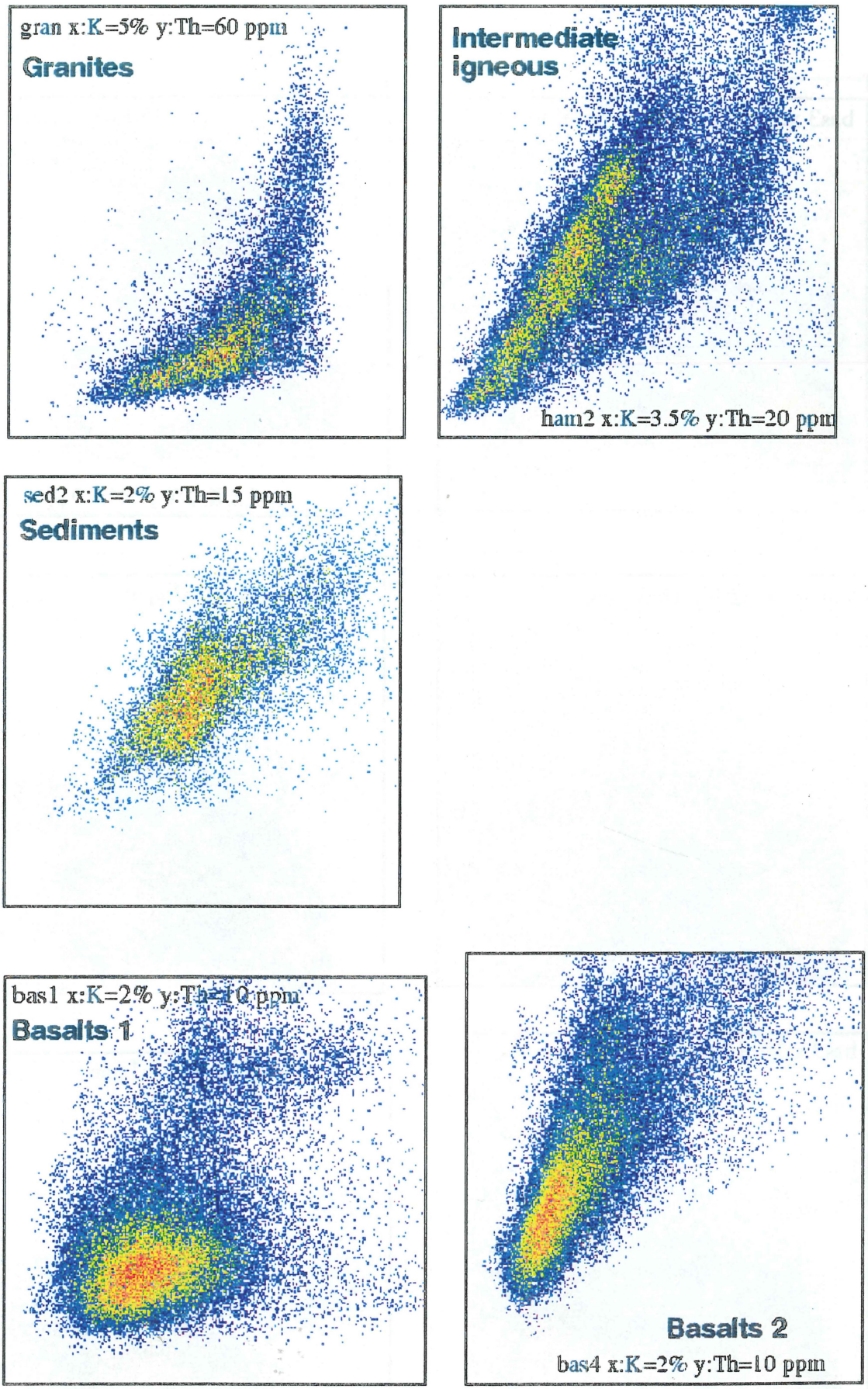

Figure 11. Scattergrams showing the significant correlation between K and Th for major rock types. The significant correlation is shown by the data points not giving a circular distribution, but falling on an elongate band, that is not parallel to either the K or Th axis. The scattergram for intermediate igneous rocks also contains points due to felsic igneous rocks (to the right of the main concentration). The scattergrams for basalts also show extraneous data, in Basalts 1 above the main concentration, and in Basalts 2 to the right of the main concentration.

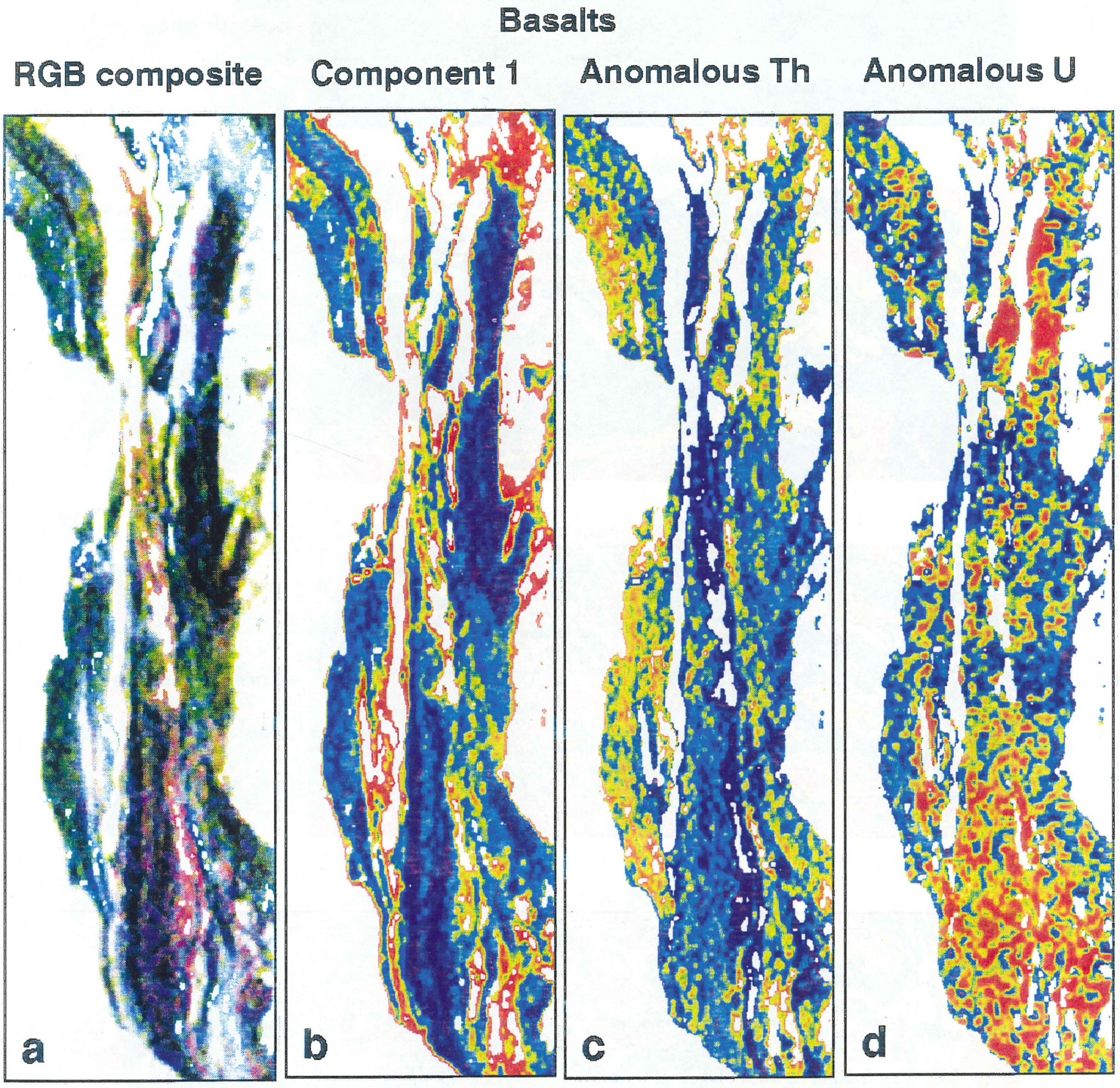

Figure 12. Mafic igneous rocks - comparison of RGB composite image (a), with pseudocolour images of the three components of the data (b, c, d).

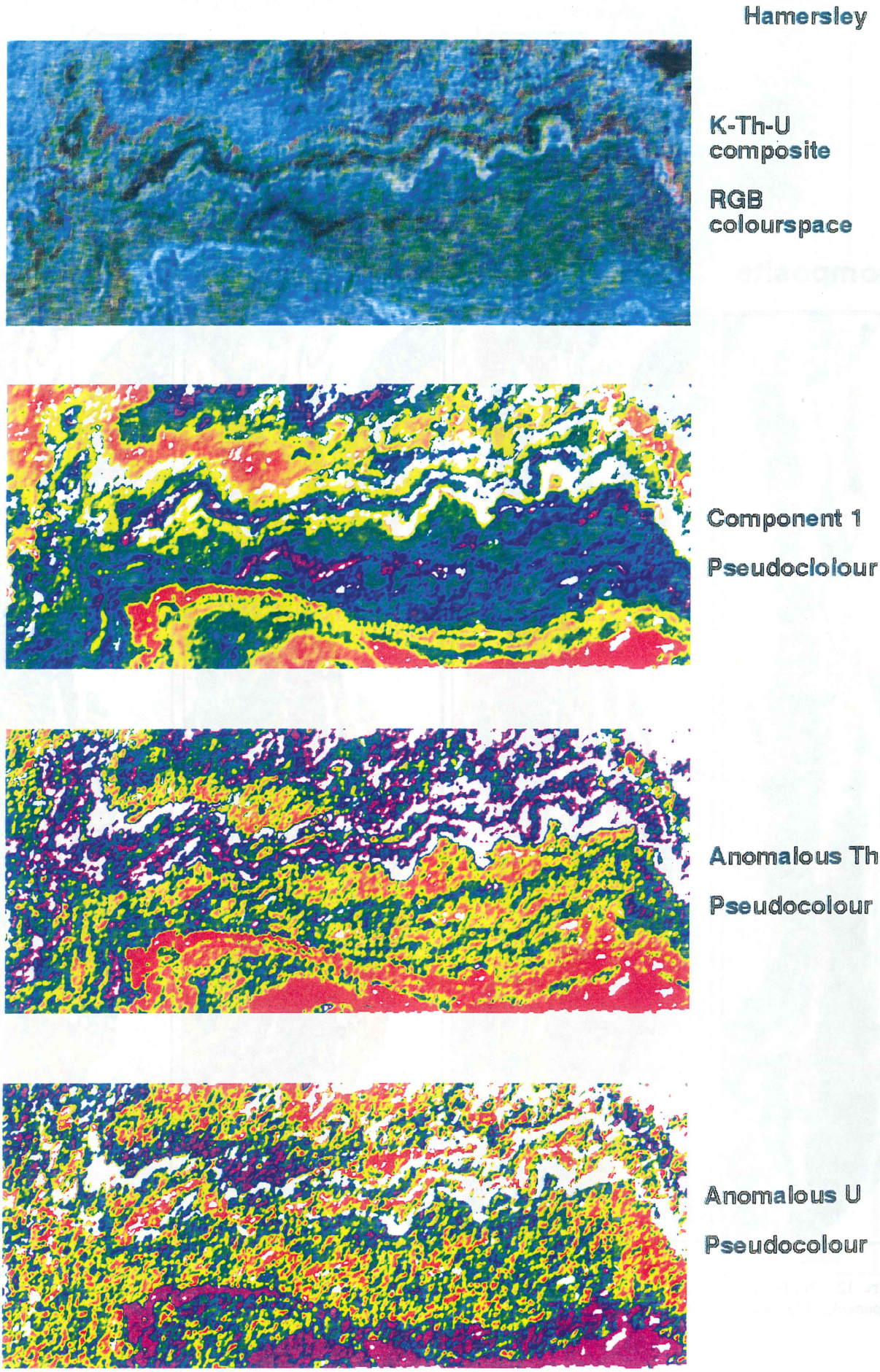

Figure 13. Intermediate igneous rocks - comparison of RGB composite image, with pseudocolour images of the three components of the data.

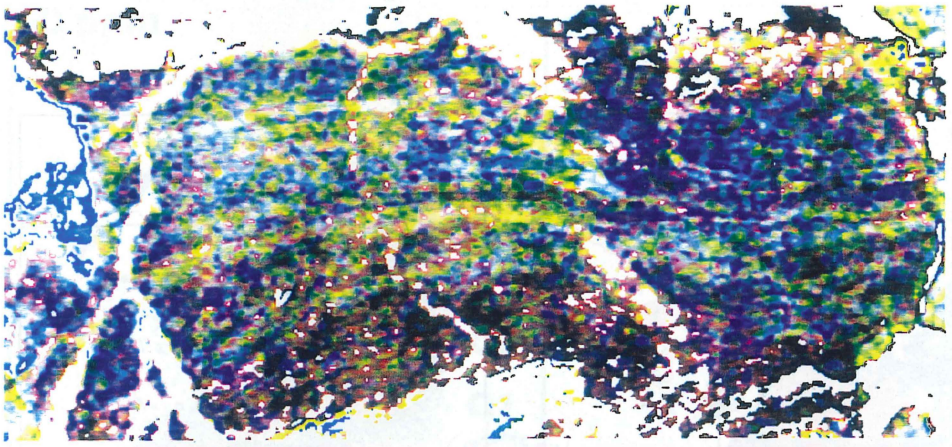

Sediments
Mosquito Creek
Synclinorium

K-Th-U
composite

RGB
colourspace

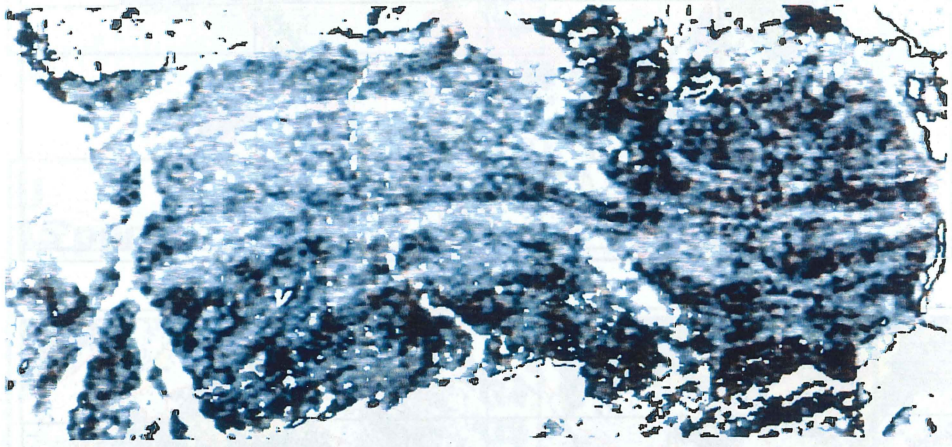

Component 1
greyscale

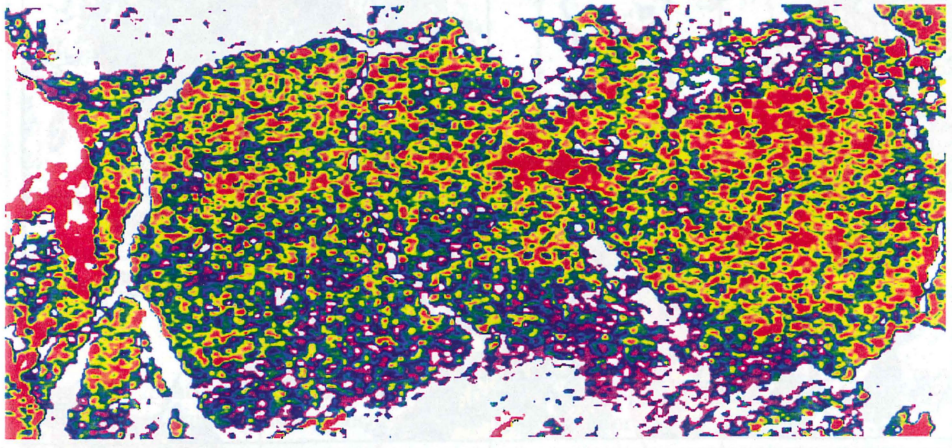

Th residual
pseudocolour

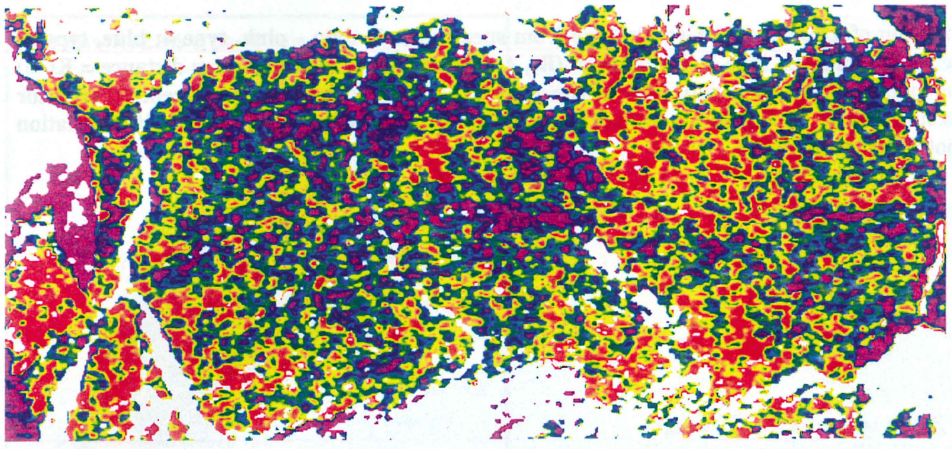

U residual
pseudocolour

Figure 14. Sedimentary rocks - comparison of RGB composite image, with pseudocolour images of the three components of the data.

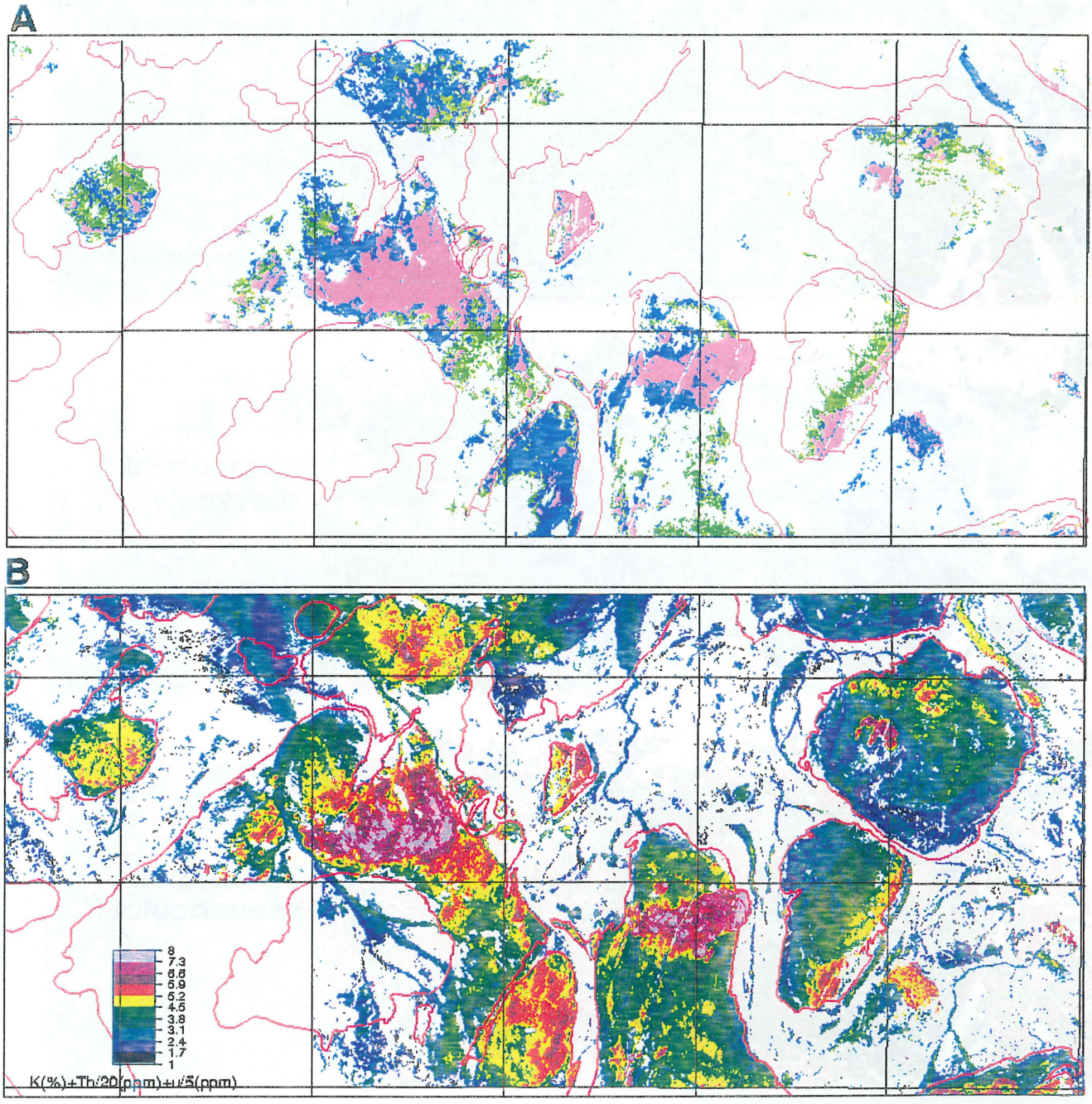

Figure 15. Amount of differentiation of granites. (A) Granite type from spectrometric data - pink, type 4; blue, type 3; green, type 2, uncoloured inside granite margin, type 1 or unknown. (B), A measure of the differentiation distance = K(%) + Th (ppm)/20 + U (ppm)/5. The maps are consistent with later intrusions into granitoid complexes being centred on prior intrusions. In A generally G4 is surrounded by G3, which in turn is generally surrounded by G2. In B the differentiation distance generally drops of smoothly to lower values.

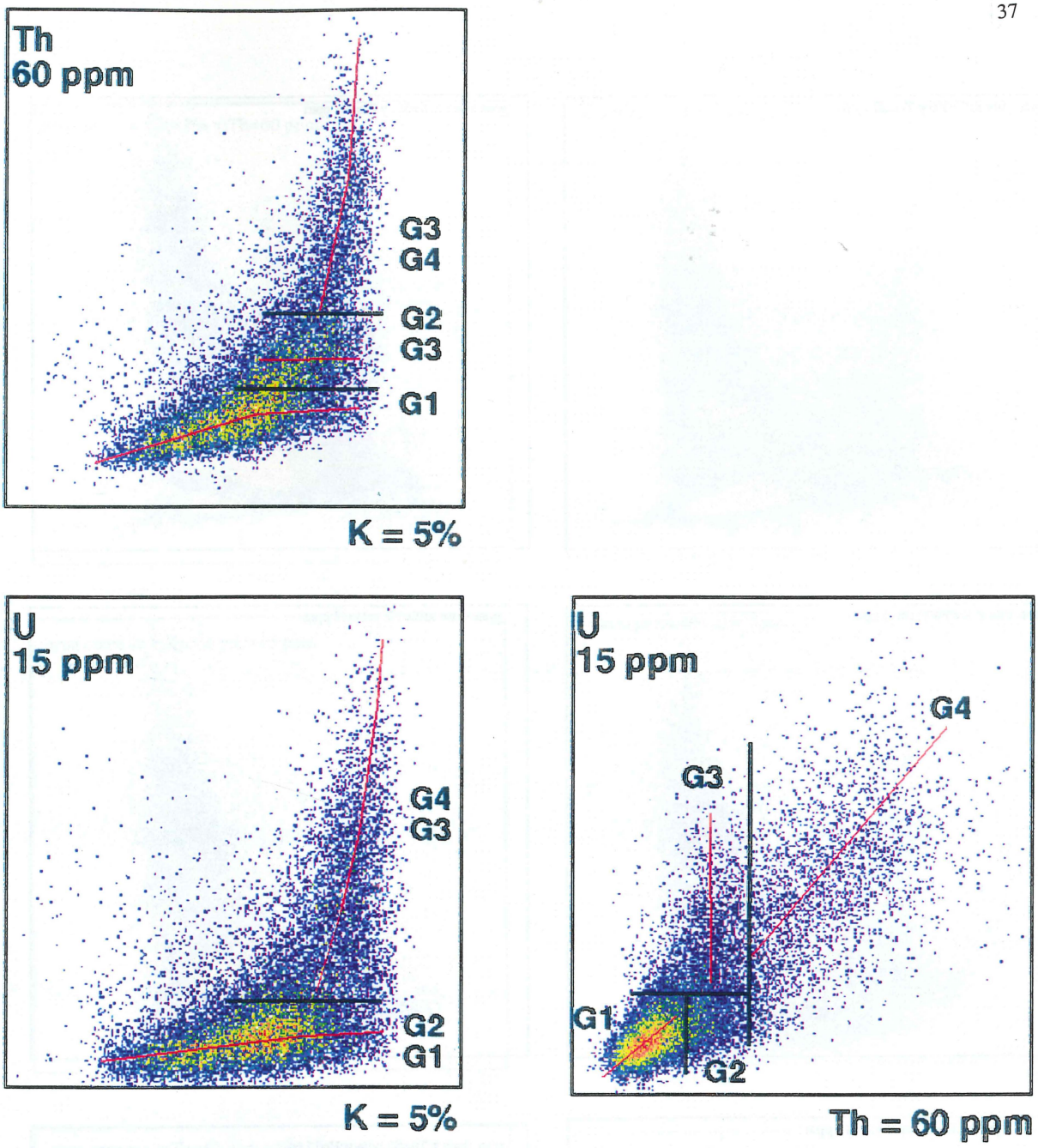

Figure 16. Scattergram of composite data from granitoid complexes. Black lines give division into granite types (G1-G4), and red lines show the mean geochemical variation path for each granite type.

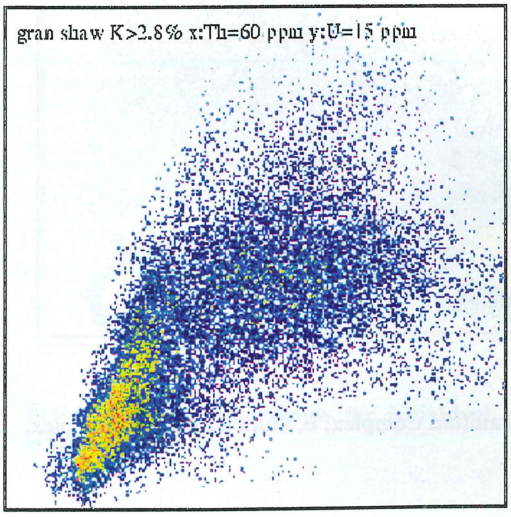

Figure 17. Scattergram of K vs Th for the Shaw Granitoid Complex granites with K > 2.8%. This shows granite type G3 with a linear array to higher U on the left, and granite type G4 with a broad, circular, scatter of points in the right.

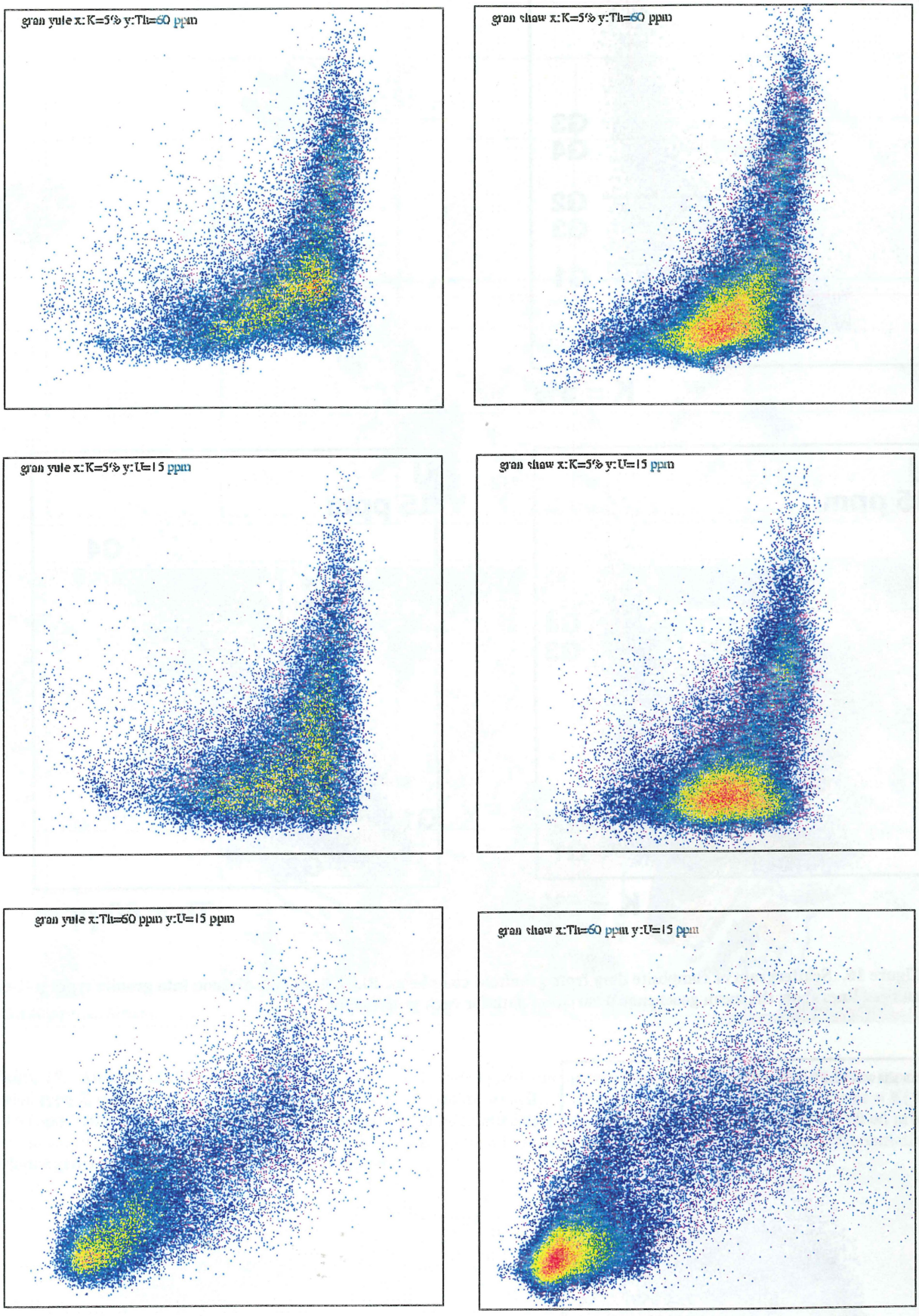

Figure 18a, b. Scattergrams for individual granitoid complexes: a, Yule Granitoid Complex; b, Shaw Granitoid Complex.

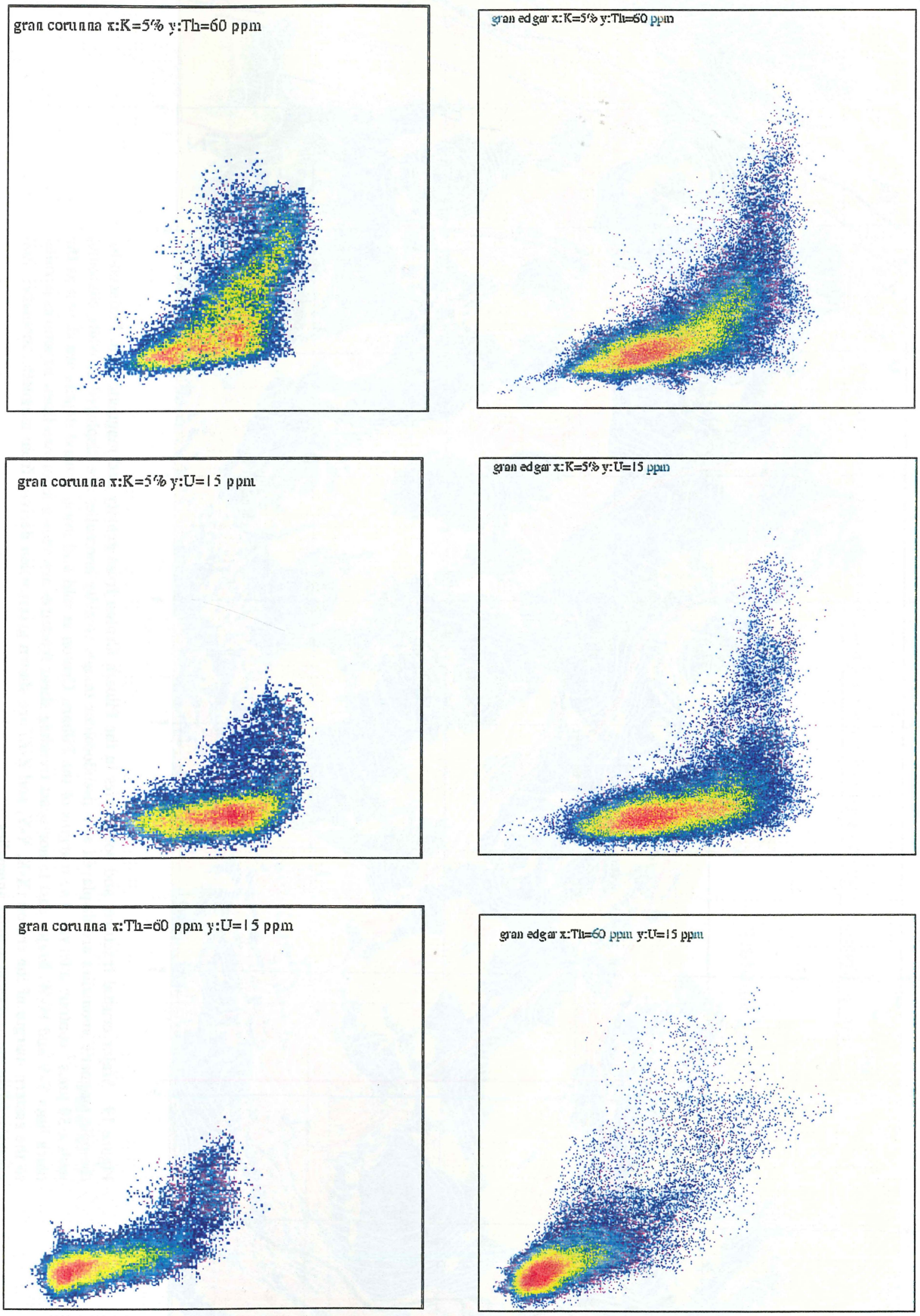

Figure 18c, d. Scattergrams for individual granitoid complexes: c, Corunna Downs Granitoid Complex; d, Edgar Granitoid Complex.

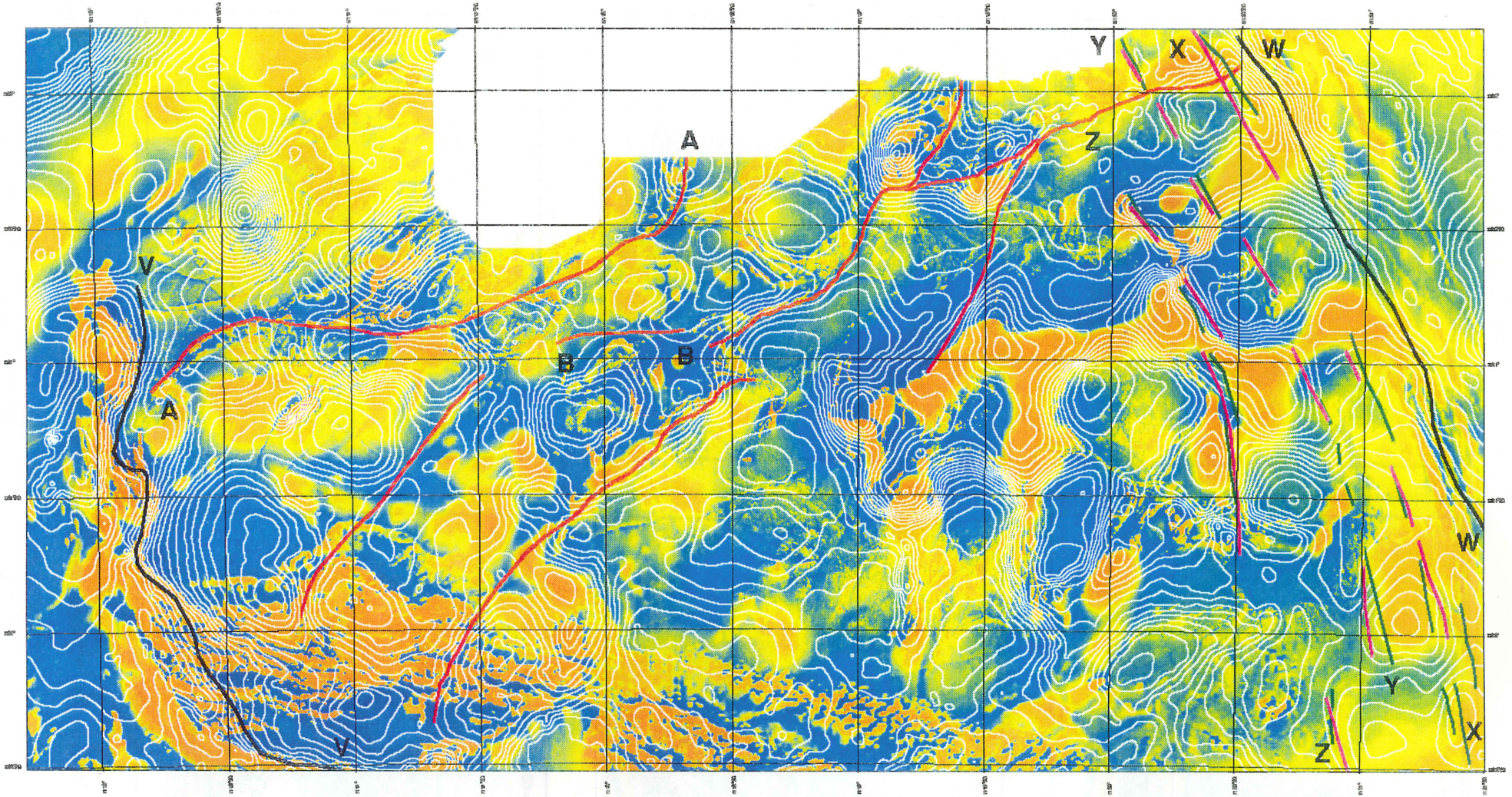

Figure 19. Major crustal fractures and boundaries in the Pilbara Craton from gravity and magnetic data. Reduced-to-the-pole magnetic anomalies are displayed as a pseudocolour image. Gravity anomalies are displayed as white contours, with a 50 $\mu m.s^{-2}$ contour interval. The margins of the Pilbara Craton at mid and lower crustal depths are shown as the black lines V-V and W-W. Major east to northeast trending shear fractures are shown as brown lines. Fractures parallel to the eastern margin of the craton (X-X, Y-Y, and Z-Z) are shown green when derived from magnetic anomalies, and magenta when derived from gravity anomalies.

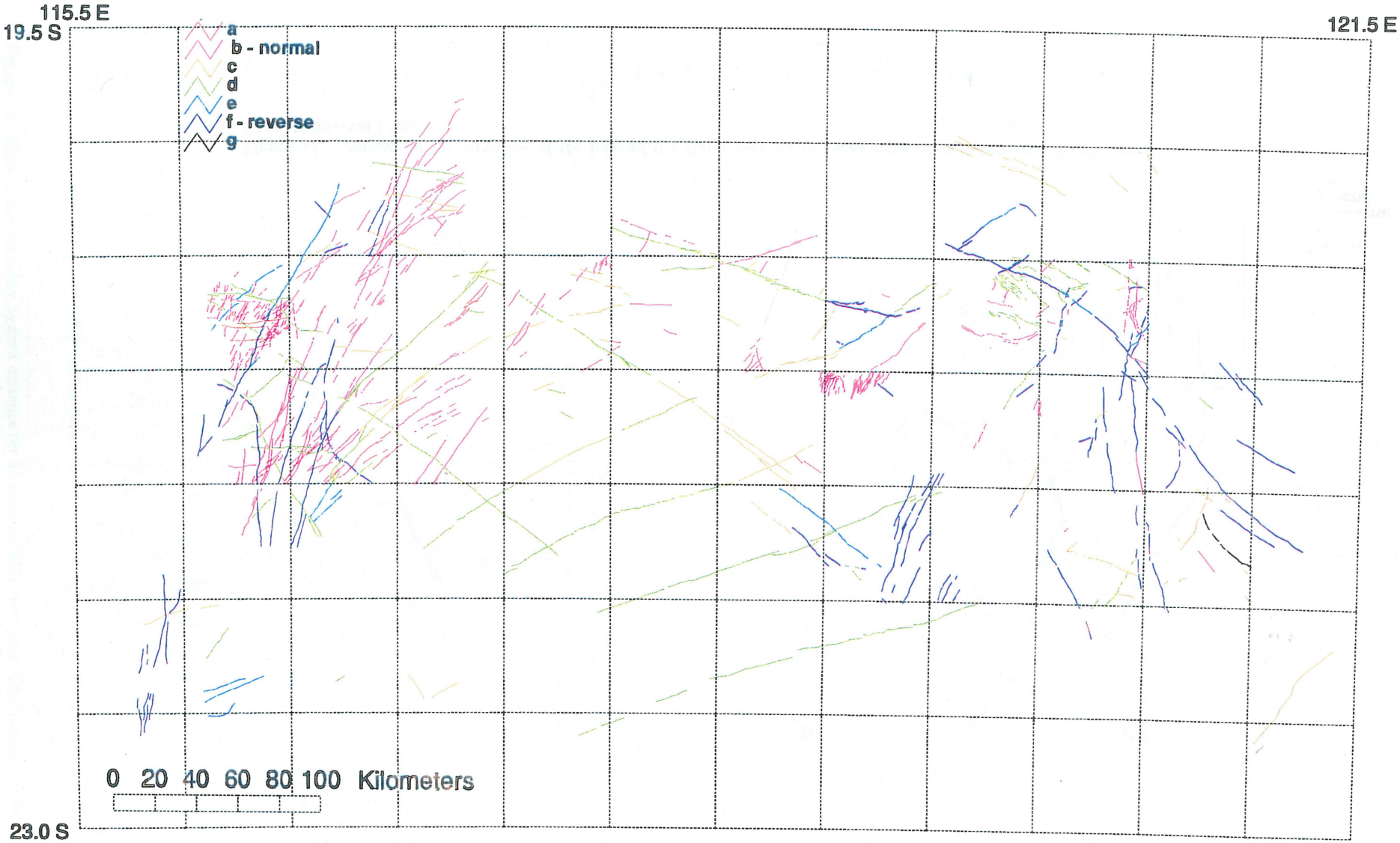

Figure 20. Magnetic polarity of dykes mapped from magnetic images. Refer to text for details.

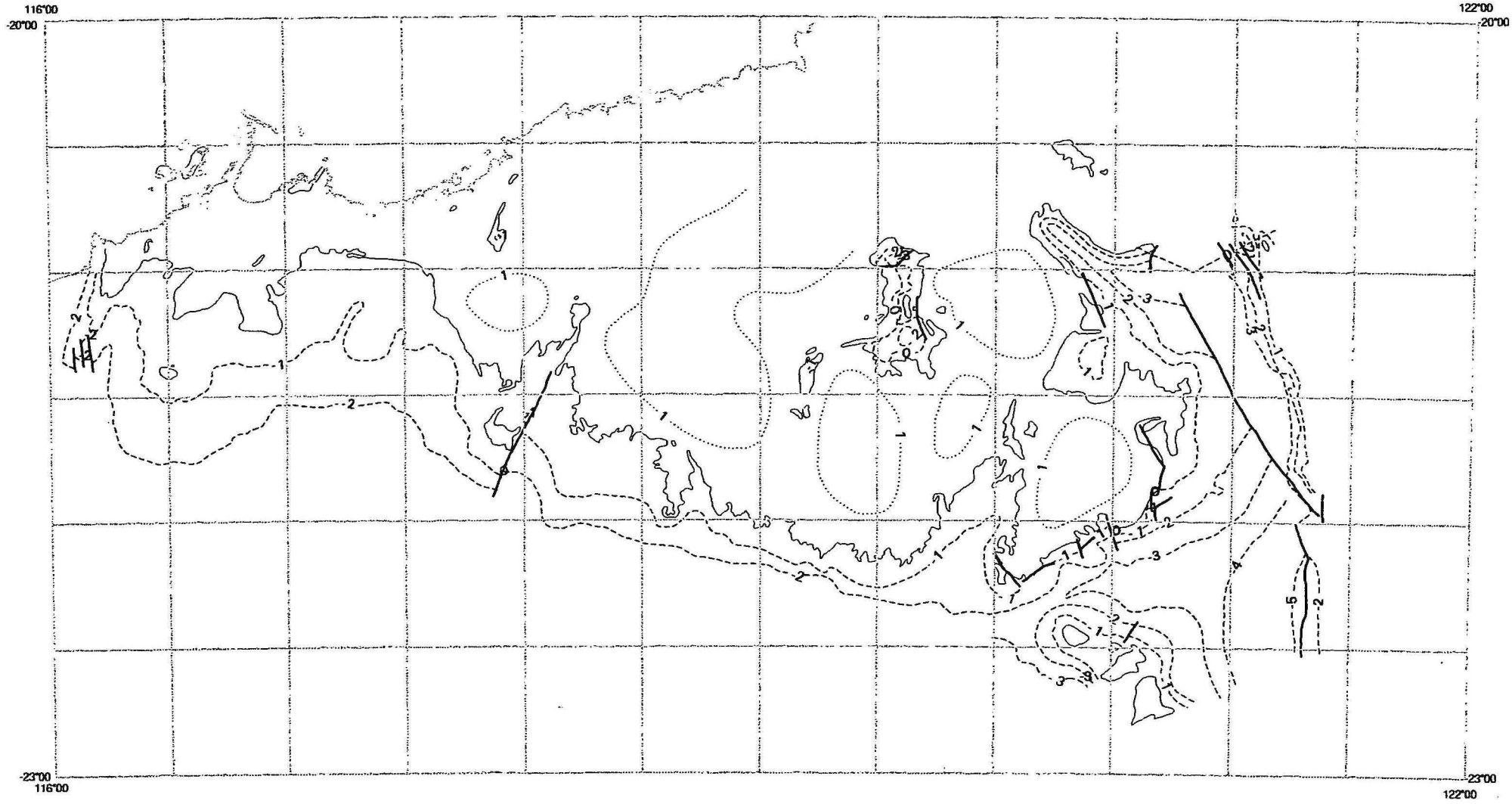

Figure 21. Contours of the elevation of the base of the Hamersley Basin rocks relative to the present Earth's surface. Contour interval 1 km.

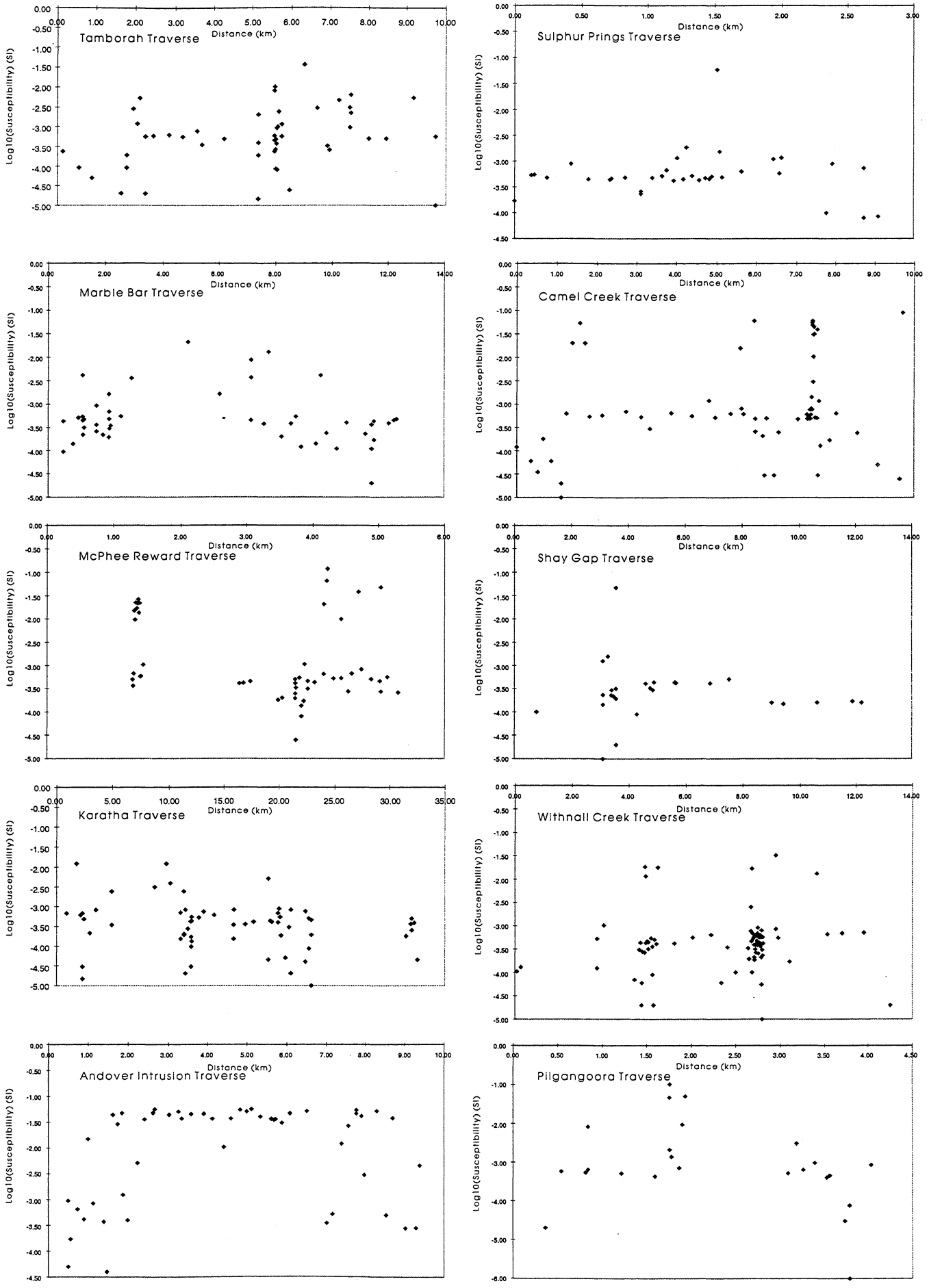

Figure 22. Plots of susceptibility against distance for 10 susceptibility traverses. The location of the traverses is shown in Figure 1.

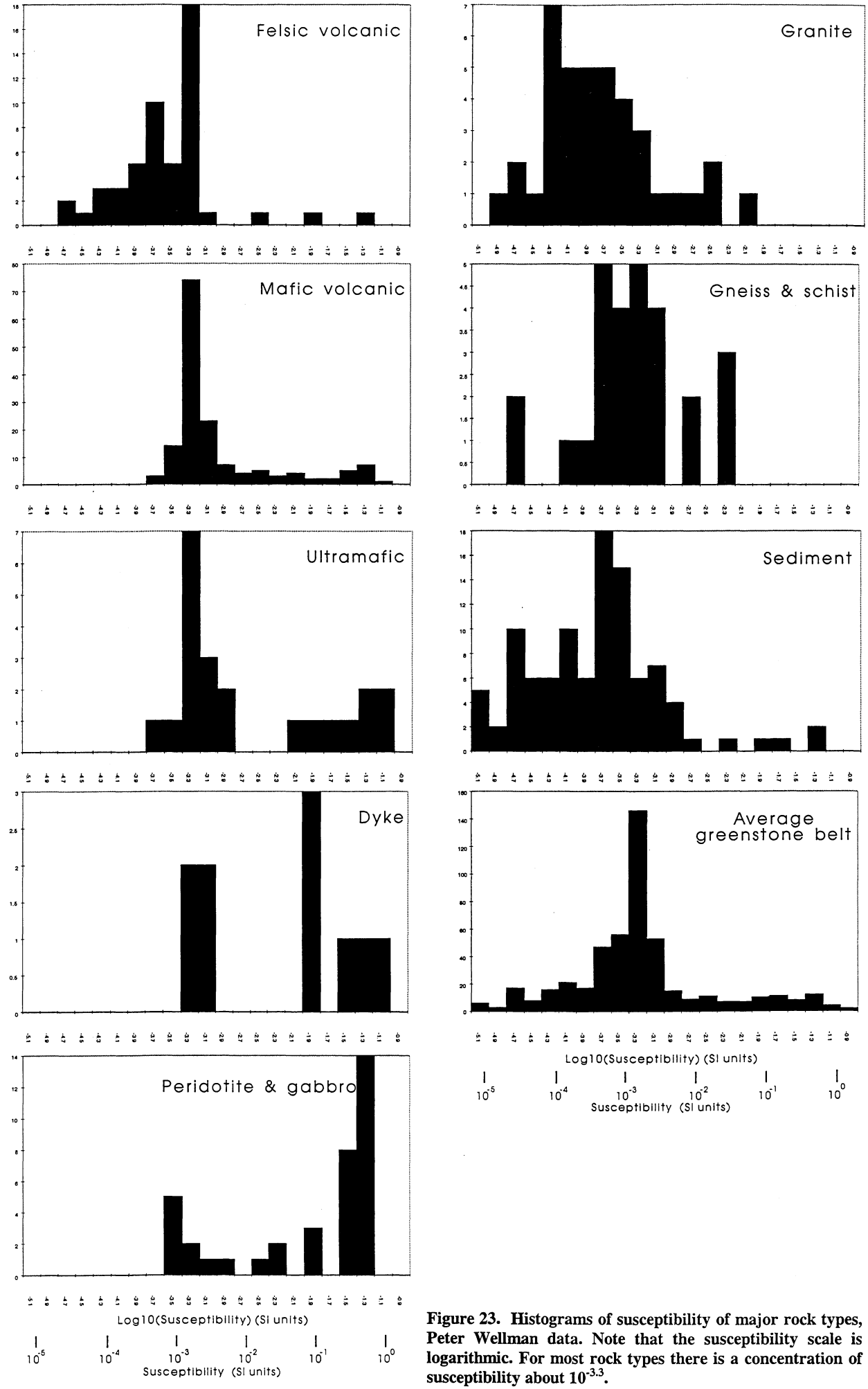

Figure 23. Histograms of susceptibility of major rock types, Peter Wellman data. Note that the susceptibility scale is logarithmic. For most rock types there is a concentration of susceptibility about $10^{-3.3}$.

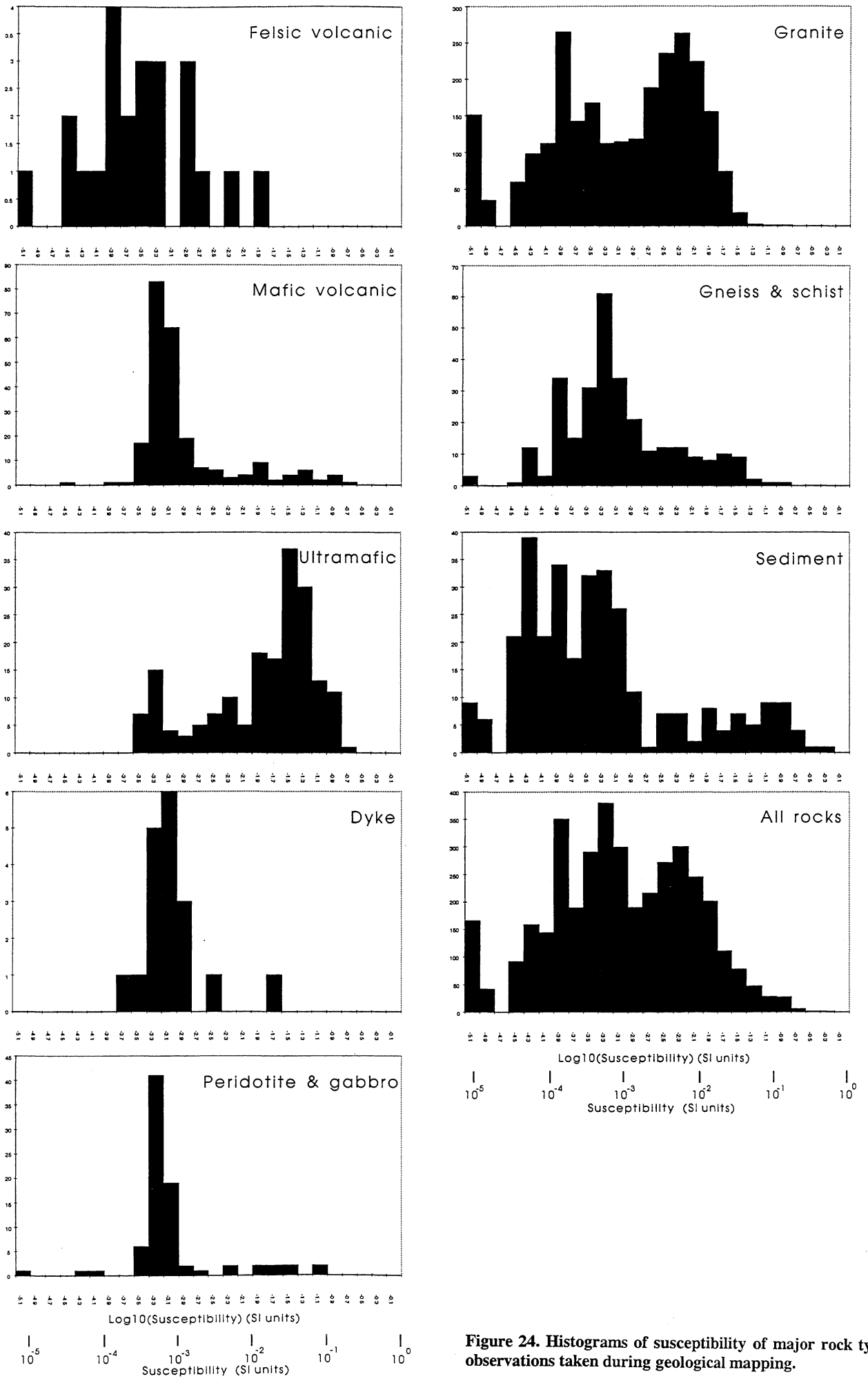

Figure 24. Histograms of susceptibility of major rock types, observations taken during geological mapping.

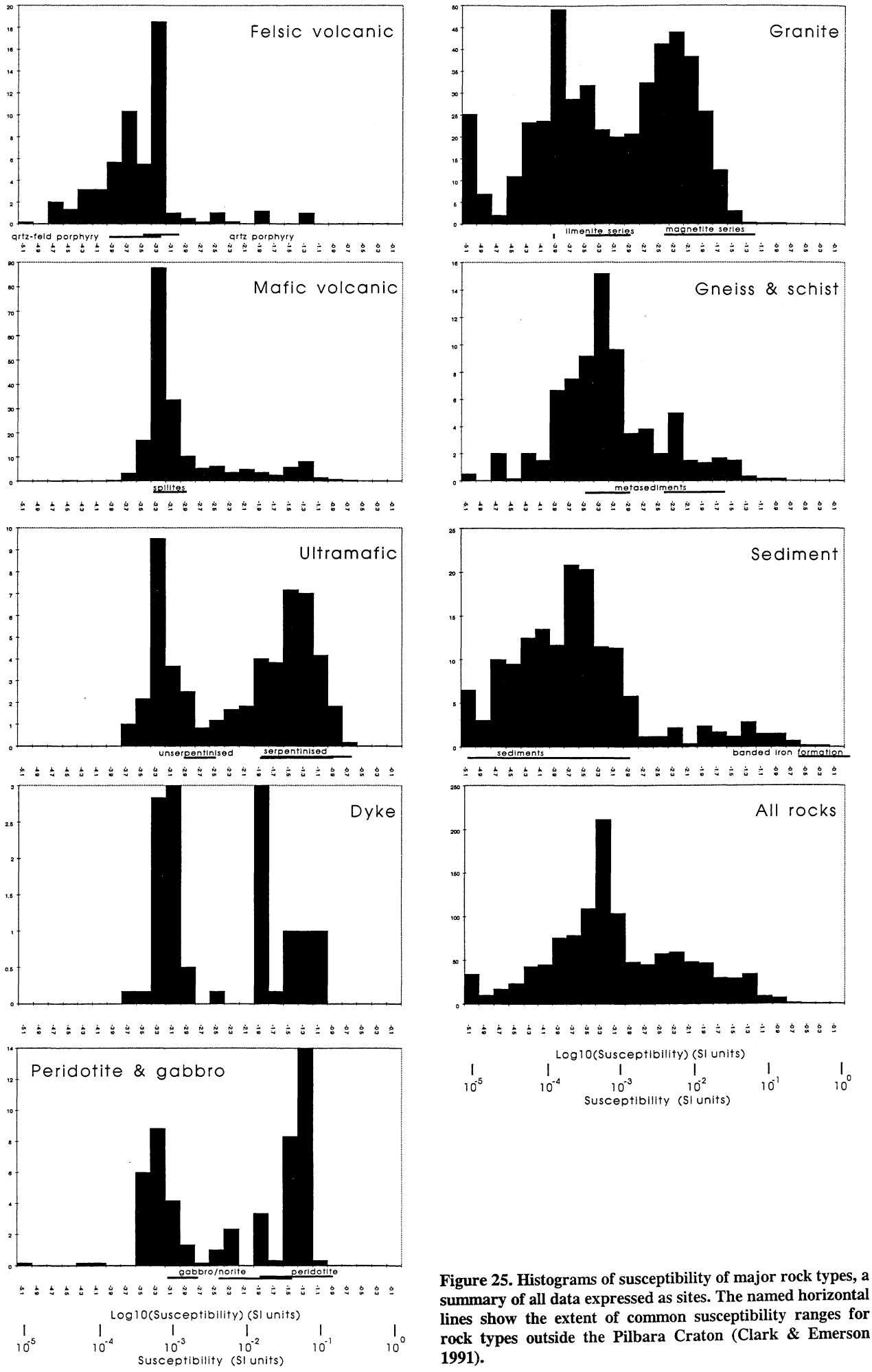

Figure 25. Histograms of susceptibility of major rock types, a summary of all data expressed as sites. The named horizontal lines show the extent of common susceptibility ranges for rock types outside the Pilbara Craton (Clark & Emerson 1991).

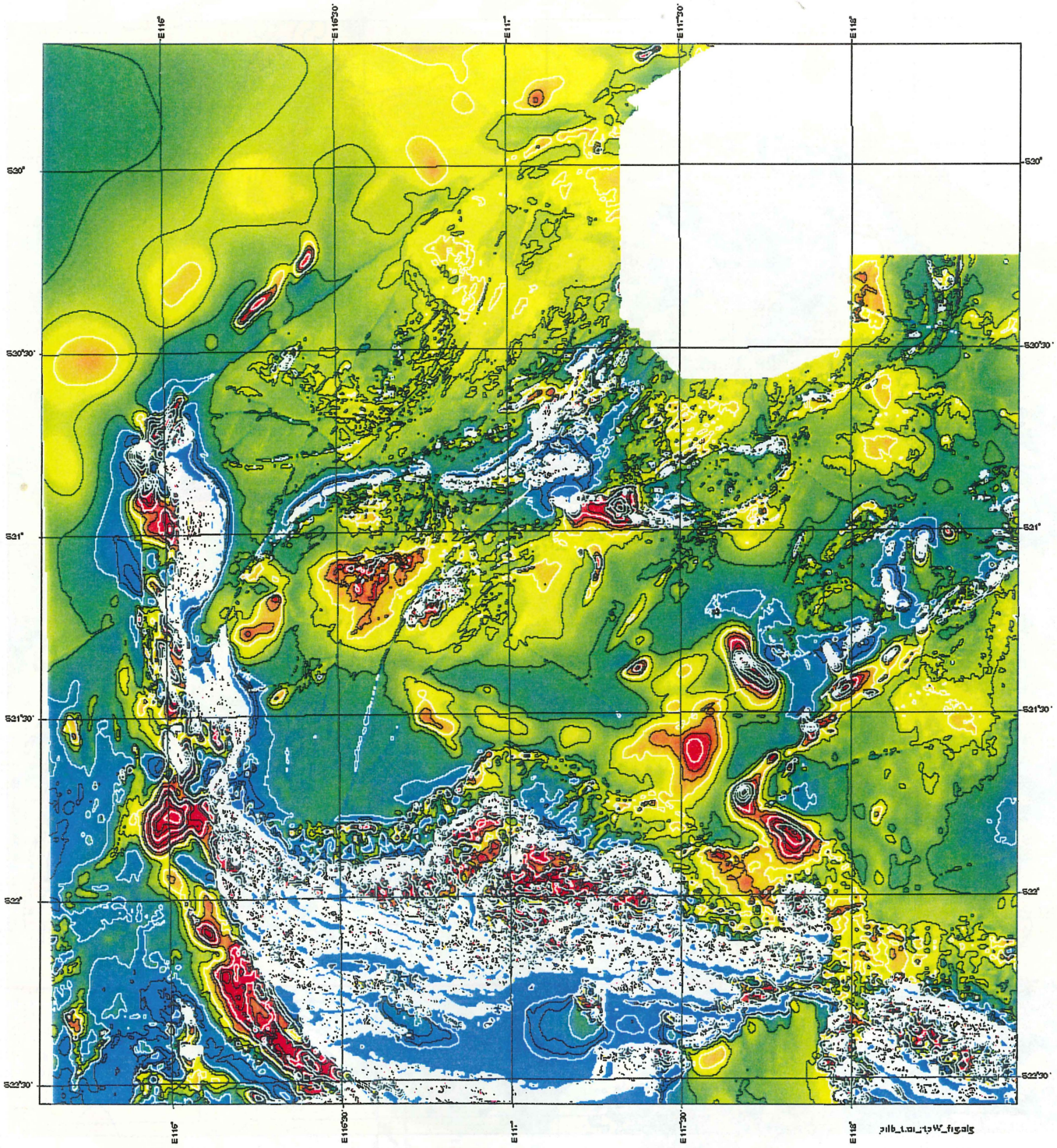

Figure 26. Total magnetic intensity reduced-to-the-pole for the western part of the Pilbara Craton. Blue is low and red is high. Contour interval is 200 nT for black lines, and 600 nT for red lines. In general the anomalies shown by a mass of white contours are caused by outcropping bodies, and the longer wavelength anomalies (red areas) are due to bodies not outcropping.

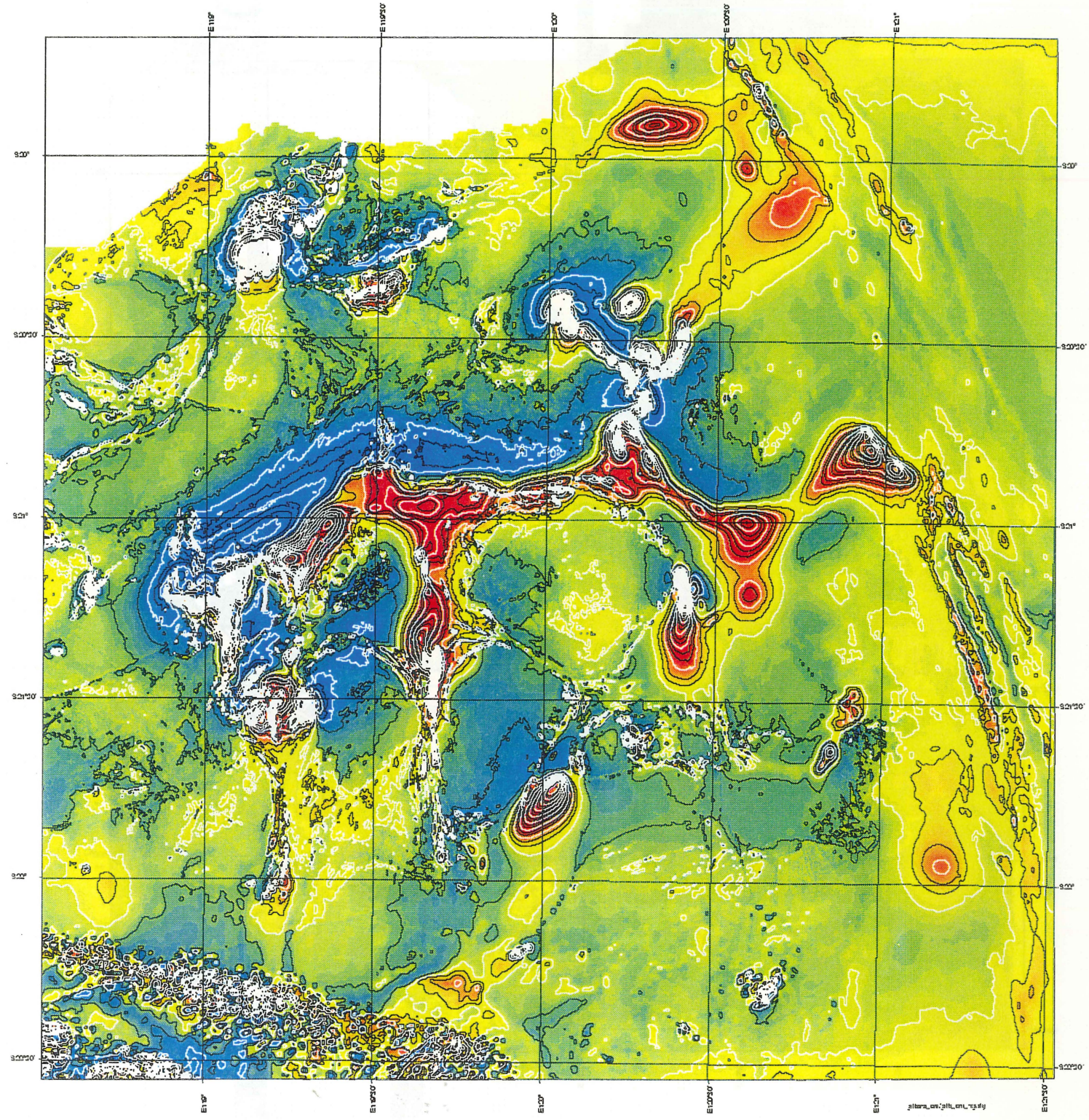

Figure 27. Total magnetic intensity reduced-to-the-pole for the eastern part of the Pilbara Craton. Blue is low and red is high. Contour interval is 200 nT for black lines, and 600 nT for red lines. In general the anomalies shown by a mass of white contours are caused by outcropping bodies, and the longer wavelength anomalies (red areas) are due to bodies not outcropping.

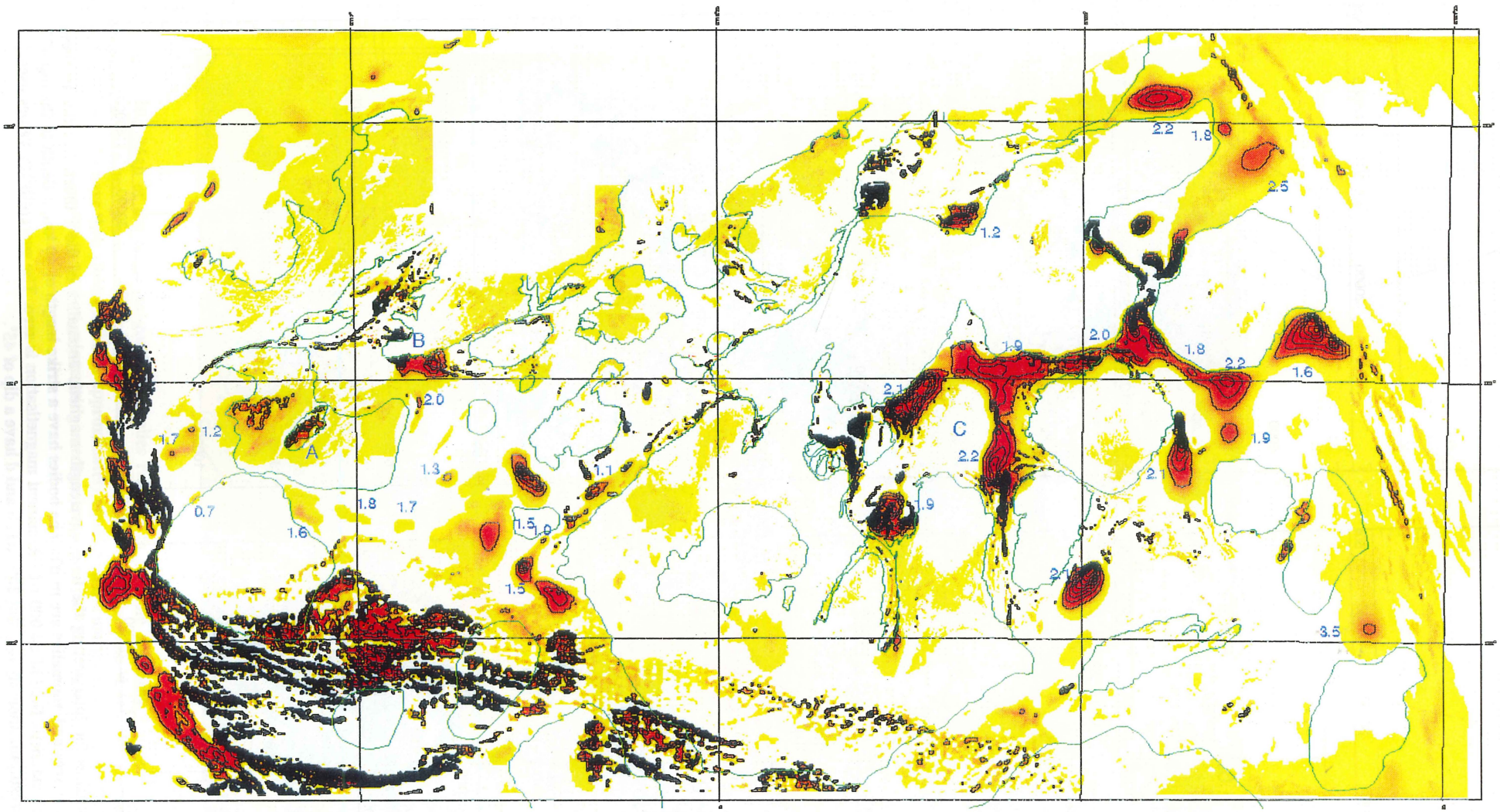

Figure 28. Interpretation of long-wavelength magnetic anomalies. Positive magnetic anomalies are shown by green to red colours and black contours with a 600 nT contour interval starting at 600 nT. The green line is the outcrop and subcrop of the granite/greenstone boundary. The numbers give the interpreted depth to the top of the long-wavelength magnetic anomalies in kilometres. The large mafic/ultramafic intrusions of Munni-Munni and Andover Intrusions are at A, B. North Pole Dome is at C. The grid shows the 1:250 000 Sheet areas. Note the greater amplitude, continuity and extent of the long wavelength magnetic anomalies in the central east Pilbara compared with the two mafic/ultramafic intrusions, and the anomalies due to the Hamersley Basin.

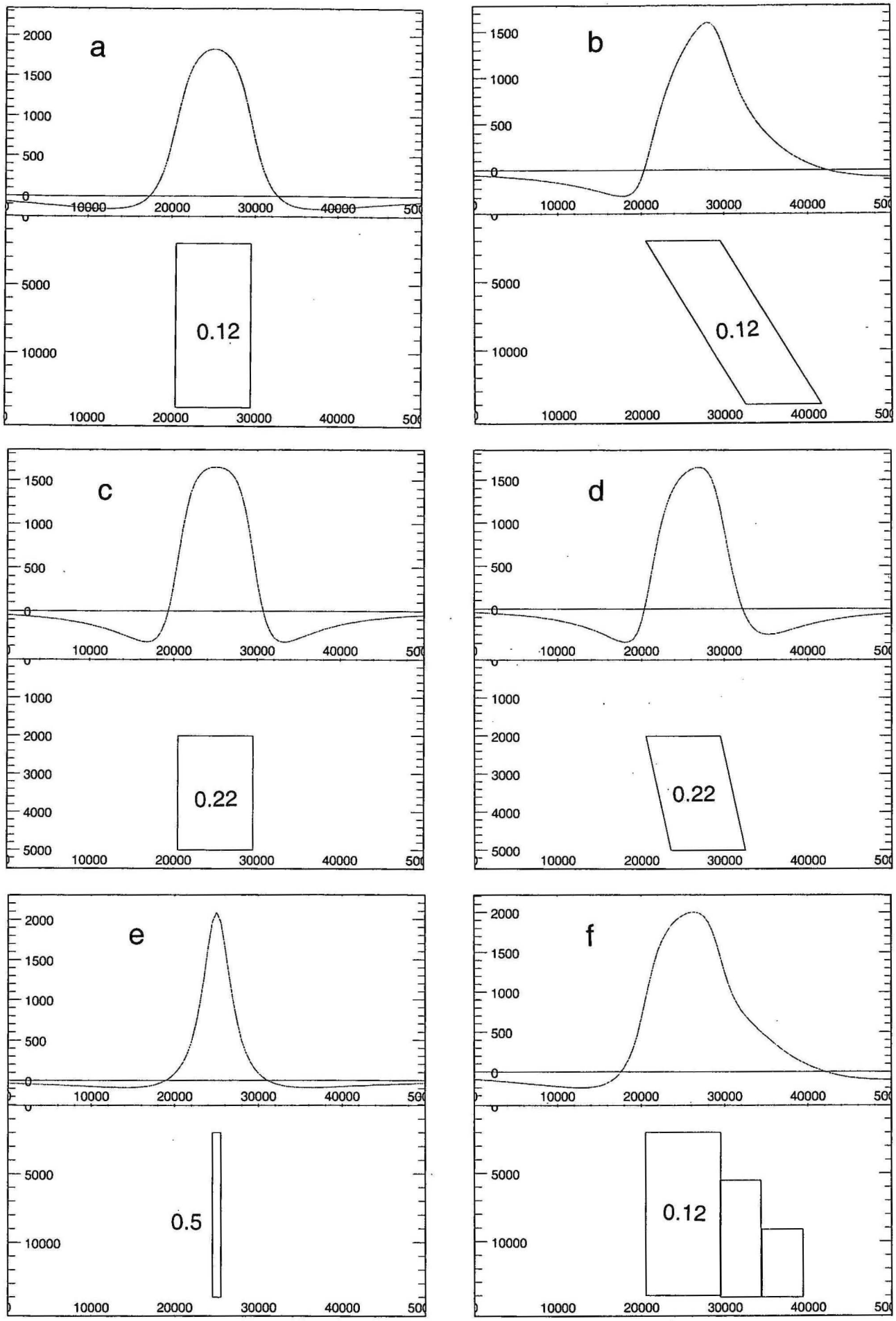

Figure 29. Model anomalies for interpreting the long-wavelength magnetic anomalies of the Pilbara Craton. In these figures distances are in metres and anomalies are in nT. The bodies have a strike length of 40 km, a depth to the top of 2 km, and are in a vertical magnetic field of 54 000 nT. Remanent magnetisation is zero. The susceptibility values used (SI units) are such that the resultant anomaly is about 2000 nT. b and d have a dip of 45°.

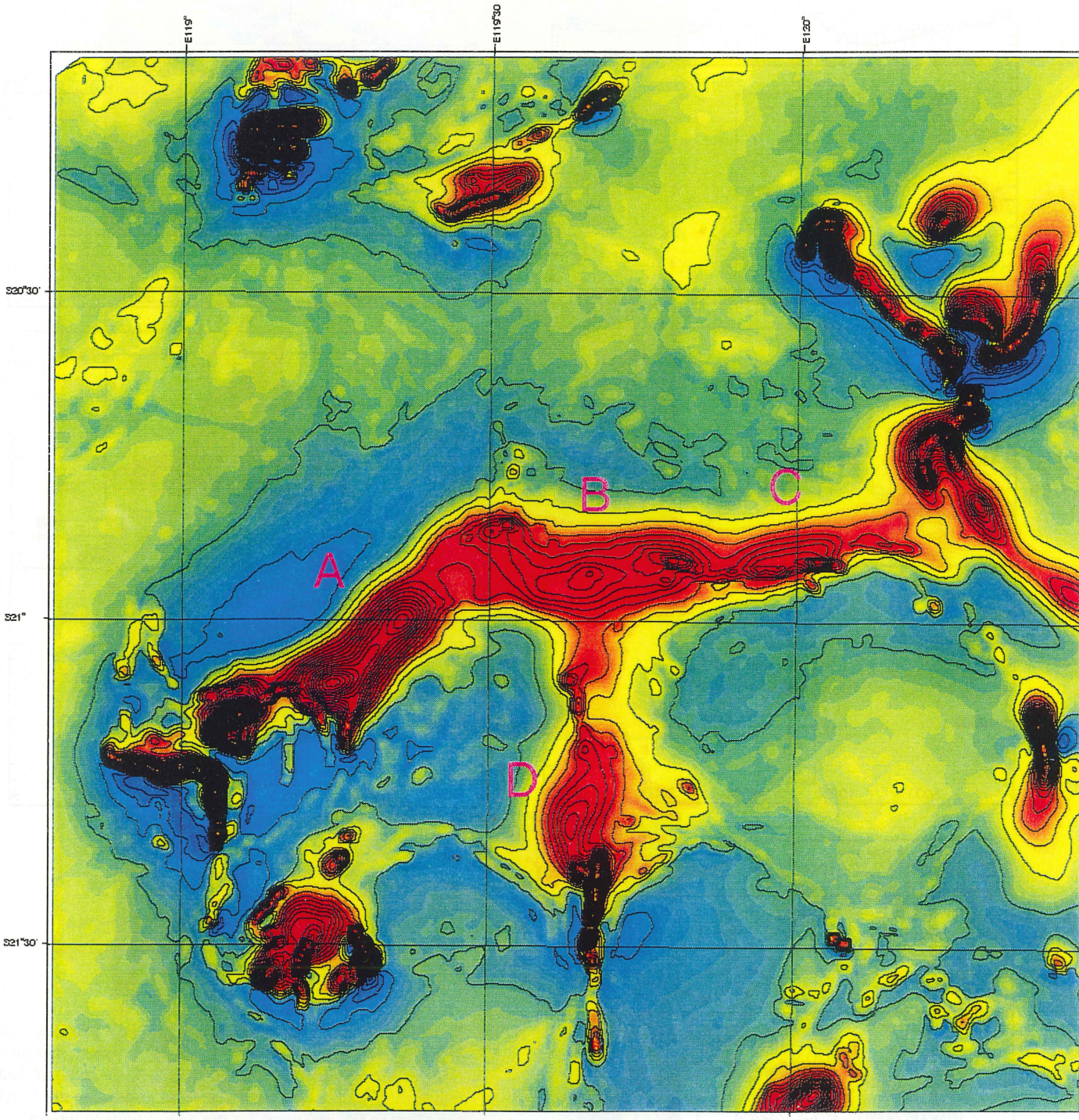

Figure 30. Map of the larger magnetic anomalies reduced to the pole assuming a magnetic inclination of -80°. The anomalies have been smoothed by using an average of width 2 km. The map shows that for this inclination the larger anomalies (A-D) have their flank gradients approximately equal, and the marginal lows approximately equal, so they have an anomaly shape similar to vertical prisms with a vertical magnetisation (Fig. 29a).

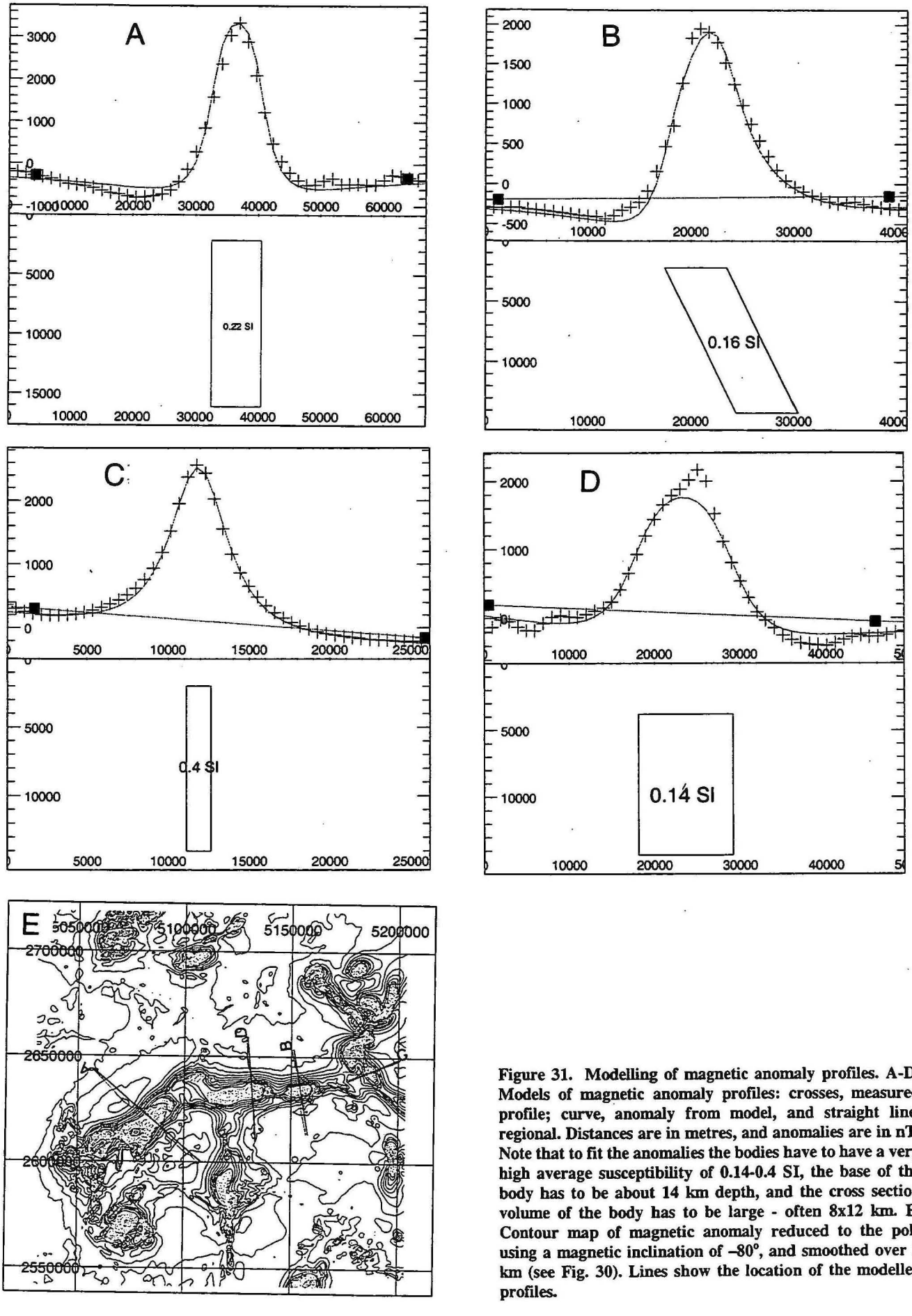

Figure 31. Modelling of magnetic anomaly profiles. A-D. Models of magnetic anomaly profiles: crosses, measured profile; curve, anomaly from model, and straight line, regional. Distances are in metres, and anomalies are in nT. Note that to fit the anomalies the bodies have to have a very high average susceptibility of 0.14-0.4 SI, the base of the body has to be about 14 km depth, and the cross section volume of the body has to be large - often 8x12 km. E. Contour map of magnetic anomaly reduced to the pole using a magnetic inclination of –80°, and smoothed over 2 km (see Fig. 30). Lines show the location of the modelled profiles.

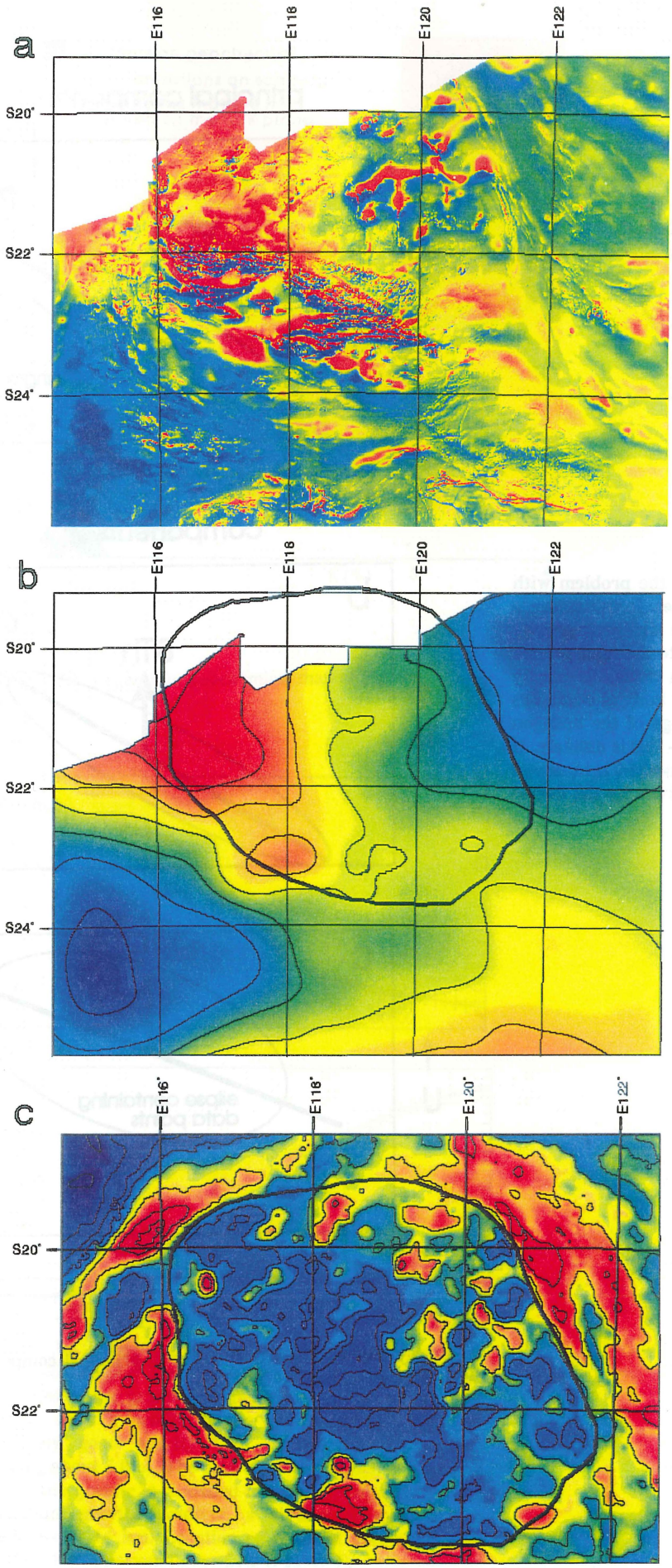

Figure 32. Regional magnetic and gravity anomalies over the Pilbara Craton. (a) Total magnetic intensity anomalies. (b) Total magnetic intensity anomalies upward continued to 50 km, contour interval is 100 nT. (c) Free air gravity anomalies with contour interval 200 $\mu m.s^{-2}$. The dark black line in b and c shows the extent of the Pilbara Craton in the middle crust from gravity anomalies.

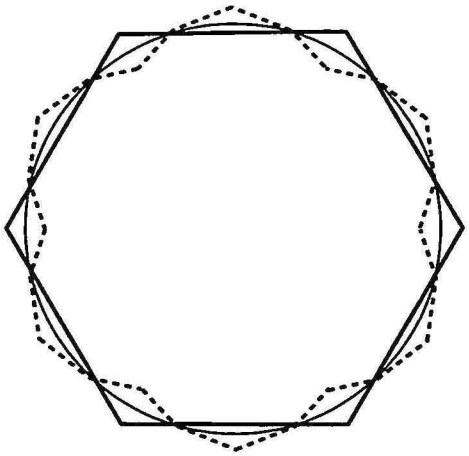

Figure 33. Synthetic example to show the problem with detailed modelling of gravity over granites. In this example the granite outcrop is a hexagon, and the maximum gravity gradient of the observed anomalies due to the total granite mass is smoother, and has the form of a circle. To exactly model the observed anomaly, the granite body at depth has to have a shape that is the mirror image of the hexagon across the line of the circle (dotted line) - this is unlikely. If the maximum gravity gradient is a smoothed measure of the shape at depth, then the estimate given by the dotted line is incorrect.

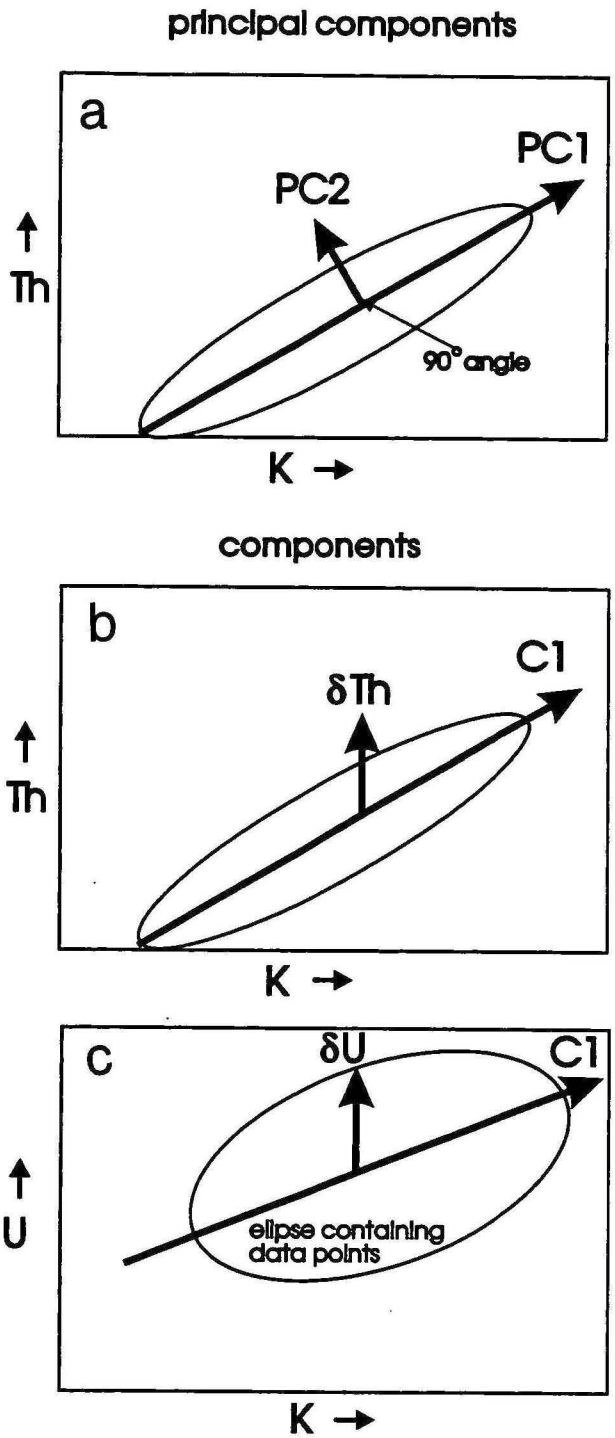

Figure 34. Coordinate systems: a, principal components; b, c, components.

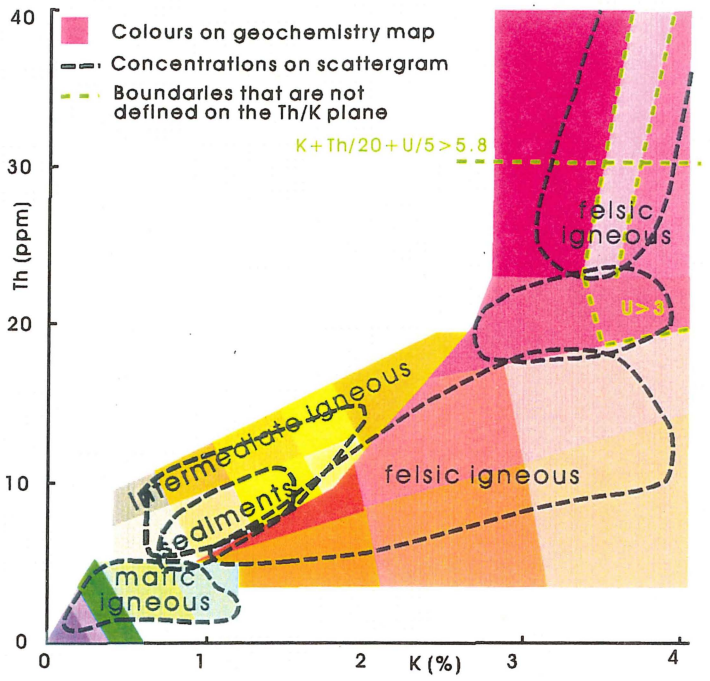

Figure 35. Legend for geochemical map of Fig. 9g.

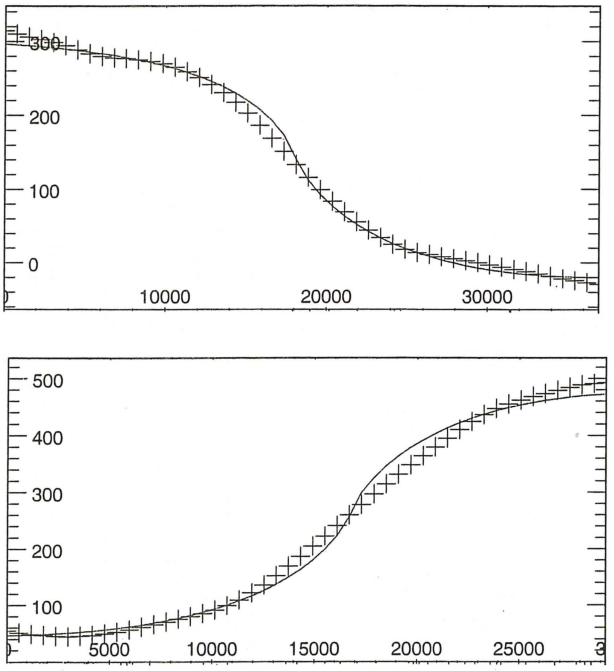

Figure 36. Modelling of the gravity anomaly between granitoid complex and greenstone belt to show that the thickness of the granitoid complexes is about 14 km. The crosses show a profile of the gravity grid in areas of relatively good gravity field control (gravity station spacing about 5 km). The lines show the modelled anomaly, where the granite is modelled to have a plan shape of the maximum gravity gradient, a vertical margin, and a thickness of 14 km. Location of gradient are: top figure 17.1°E 21.4°S, bottom figure 21.9°S 119.7°E.